Transport and Spectral Properties of Electrons on Curved Three-Dimensional Topological Insulators

Submitted by:
Ioachim Dusa
University of Regensburg
Department of Theoretical Physics

Submission Date:
July 2, 2024

First Reviewer:
Prof. Dr. Klaus Richter

Second Reviewer:
Prof. Dr. Ferdinand Evers

Desired Academic Degree:
Master of Science

Abstract

Over the last two decades, topological insulators have attracted considerable interest due to their unique ability to robustly conduct charge carriers at their surfaces, while remaining insulating inside. To date, the mechanism by which these surface states arise has been well understood, giving us considerable insight into the massless Dirac particle nature of these states. However, previous studies have focused only on trivial geometries of topological insulators, such as flat slabs or thin films, with no intrinsic or extrinsic curvature. Moreover, experimental progress shows the possibility of growing topological insulating crystalline structures with various complex geometries.

Therefore, to fill the theoretical gap and to motivate new experiments, we generalize the description of topological insulators to general curved spaces, and consider the Dirac Hamiltonian on several prominent curved surfaces, such as the cone and the pseudosphere, subjected to a coaxial magnetic field.

In the first part of the thesis, we calculate the bound states on these surfaces and find that the energies decompose into two branches, one which is curvature independent and always scales with $\propto B^{\frac{1}{2}}$, and one which is curvature dependent, giving us, for example, in the case of the pseudosphere, a peculiar scaling of $\propto B^{\frac{1}{4}}$. Notably, we find a further surface whose curvature dependent part of the spectrum has bound state energies that are independent of the magnetic field.

In the second part of the thesis, we perform quantum magnetotransport simulations on the pseudosphere, including a longitudinal conductance and a 4-terminal quantum Hall simulation. For the longitudinal simulation, we reveal the mechanism by which electrons propagate along curved topological insulator surfaces, consisting of resonant tunneling through non-degenerate energy levels that have a non-zero overlap due to disorder effects in the materials, such as impurities. For the quantum Hall transport simulation, we reveal the mechanism by which the edge states give rise to quantum Hall plateaus in a 4 terminal measurement on curved surfaces.

Contents

List of Figures

1 Introduction

In 1980, Klaus von Klitzing made the seminal discovery of the Quantum Hall Effect (QHE) [1], where the transverse Hall resistance R_{Hall} exhibits steps that take on quantized values

$$R_{\text{Hall}} = \frac{h}{e^2 \nu}\,, \tag{1.1}$$

with some natural number ν. Over the more than four decades since this discovery, it has played a major role in inspiring and motivating new areas of research in condensed matter physics [2–4], one of which is *topological condensed matter physics*. This research area explores how the principles of topology, a branch of mathematics, can be applied to understand various phenomena in condensed matter systems.

For physicists, *topology* is the discipline that studies the properties of objects that remain unchanged under continuous transformations, such as stretching or bending, while gluing or tearing is forbidden. These properties are known as *topological invariants*. In condensed matter physics, we are particularly interested in these invariants when discussing the band structure. One such invariant is the Chern number $\mathcal{C}$ [5], which is closely related to the well-known Berry curvature [6]. The Chern number can be thought of as the total flux of the Berry curvature through the entire Brillouin zone. As a topological invariant, the Chern number is quantized $\mathcal{C} \in \mathbb{Z}$ and provides a straightforward way to classify specific topological properties of a system's band structure by just one number - a number that remains constant even if the system is deformed to a certain extent. This is where the QHE comes into play, which has been shown to be closely related to the Chern number [7]

$$R_{\text{Hall}} = \frac{h}{e^2 \mathcal{C}}\,, \tag{1.2}$$

revealing its intimate relationship to topology, which explains the striking universality and stability of the plateaus.

Since then, numerous materials have been discovered to possess diverse topological properties [8–10], i.e., materials that allow us to link physical phenomena to some topological invariant. This research project deals with probably the most prominent type of materials: *topological insulators* (TIs), which can be two-dimensional (2DTIs) or three-dimensional (3DTIs)[1]. TIs are materials that are insulating in the bulk but conduct electricity at their surfaces or edges. The most studied examples include HgTe, Bi_2Te_3, and Bi_2Se_3. For these and many other materials, this behavior has been demonstrated theoretically and experimentally [11]. While this is the most defining property of TIs, they often exhibit other equally interesting properties such as time-reversal symmetry (TRS) or surface states with spin-momentum

[1] In this work, we will focus on 3DTIs.

locking, as measured in Bi_2Se_3 [12]. These materials are not only interesting from an academic perspective but also from an applications point of view, since the electronic properties of TIs are very stable against small perturbations such as structural imperfections, minor chemical impurities, or deformations. This makes TIs attractive for new types of electronic devices. As in the QHE, the stability and universality of these properties suggest that TIs can be classified by the topology of their band structure and therefore by some topological invariant[1].

Although the topological nature of TIs has been well studied to this day, a large part of the research has focused on trivial real-space geometries of TIs, such as flat slabs or other flat geometries, without any intrinsic or extrinsic curvature.

Only in recent experiments have geometries with non-zero curvature been explored. These advances demonstrate the feasibility of designing TI nanowires with spatially varying cross-sections [13]. Furthermore, even in experiments intended for flat geometries, non-zero curvature is sometimes inevitable [14]. This makes TIs, which host Dirac-type boundary states, a perfect platform for experimentally exploring quantum mechanics, including quantum Hall physics, in curved spaces.

This work addresses this aspect by theoretically investigating the effects of real-space curvature on the physics of 3DTIs. Although topological arguments are central to explaining the Dirac-type boundary states of flat TIs, they become secondary when generalizing TIs from flat to curved spaces, as this procedure is more geometrical in nature. To highlight this contrast, we will present both, geometrical and topological aspects of TIs.

Altogether, this work aims to pave the way for experimentalists to explore quantum mechanics in new geometries, potentially uncovering new properties that could be exploited for quantum computing, spintronics, and other significant research areas.

In Chapter 2, we provide a brief overview of the quantum spin Hall effect in graphene. This example serves as a pedagogical illustration of the emergence of edge states in 2DTIs, which relies on the mechanism of band inversion due to spin-orbit coupling. This same mechanism gives rise to surface states in 3DTIs in a similar, yet more intricate, fashion. While we will not delve into this depth here, the discussion will provide a sufficient foundation for understanding the emergence of Dirac-type surface states in flat 3DTIs.

In Chapter 3, we examine the mathematical formulation of the Dirac equation in curved spaces, which will then be used to generalize flat 3DTIs to curved 3DTIs.

In Chapter 4, we introduce the discretization scheme imposed on the Dirac system to enable numerical calculation of physical quantities.

In Chapter 5, we solve the Dirac equation on curved surfaces for various types

[1]In fact, as we will soon discuss in Chapter 2, TIs are classified by the so-called $\mathbb{Z}_2$ invariant, which is different from the Chern number $\mathcal{C}$.

of surfaces of revolution subjected to a coaxial magnetic field. We find that energies decompose into two branches: one which is curvature dependent and one that always scales with $\propto B^{\frac{1}{2}}$. For example, on the pseudosphere, the curvature dependent part scales with $\propto B^{\frac{1}{4}}$, and we identify a surface where this part is independent of the magnetic field. Additionally, we propose a conjecture predicting the magnetic field dependence on any surface of revolution, supported by numerical calculations.

In Chapter 6, we perform quantum magnetotransport simulations on a surface of constant negative curvature, including a longitudinal conductance simulation and a 4-terminal quantum Hall simulation. For the longitudinal conductance simulations, we find that the electron travels along a surface of revolution by resonant tunneling through non-degenerate energy levels. In the 4-terminal quantum Hall simulations, we compute the transversal resistance, which exhibits perfect quantum Hall plateaus explained by the emergence of edge sates at the borders of the surface.

2 Emergence of boundary states in TIs

In this chapter we give a detailed outline of the underlying mechanisms of TIs, consisting mainly of topology and spin-orbit coupling (SOC). The arguments and concepts in this chapter are taken from [15]. While the following discussion introduces the defining properties of TIs, such as Dirac boundary states, through the simpler case of 2DTIs, the same underlying mechanisms also give rise to surface states in 3DTIs in a similar but more complex manner. Consequently, this chapter serves as a pedagogical motivation, using the 2D example to illustrate that the surfaces of 3DTIs can be modeled as massless Dirac systems in a similar way.

To understand the defining properties of TIs using the 2D case, we first need to properly introduce the already mentioned Chern number and consequently also the Berry curvature. Essentially, the Berry curvature stems from the general gauge freedom of Bloch states $|\psi(\mathbf{k})\rangle$ in solid state physics

$$|\psi(\mathbf{k})\rangle \to \exp(i\varphi(\mathbf{k}))|\psi(\mathbf{k})\rangle\,, \tag{2.1}$$

which strongly resembles an electromagnetic gauge transformation. Therefore, one tries to define a vector potential $\mathbf{A}$ which satisfies

$$\mathbf{A} \to \mathbf{A} + \nabla_{\mathbf{k}}\varphi(\mathbf{k}) \tag{2.2}$$

and thus leads to the canonical definition

$$\mathbf{A} = -i\langle\psi(\mathbf{k})|\nabla_{\mathbf{k}}\psi(\mathbf{k})\rangle\,. \tag{2.3}$$

From this, the famous Berry phase can be defined as

$$\gamma_C = \oint_\Gamma \mathbf{A}\mathrm{d}\mathbf{k}\,, \tag{2.4}$$

where Γ is a closed loop. Therefore, the Berry phase describes geometric properties of the band structure associated with the path. If we desire some quantity that encodes properties of the whole band structure at once, we arrive at the definition of the Chern number

$$\mathcal{C} = \frac{1}{2\pi}\int_{T^2} \mathbf{F}\mathrm{d}^2\mathbf{k}\,, \tag{2.5}$$

where T^2 is the first Brillouin zone and finally

$$\mathbf{F}(\mathbf{k}) = \nabla_{\mathbf{k}} \times \mathbf{A} \tag{2.6}$$

is the Berry curvature, which is analogous to the magnetic field in electromagnetism. Just as a magnetic field in real space can cause a charged particle to perform

cyclotron orbits, the Berry curvature can affect the "motion" of wave packets in momentum space. And just as the magnetic flux through a real space surface tells us how much magnetic field passes through that surface, the Chern number $\mathcal{C}$ tells us how much Berry curvature passes through the whole momentum space.

We can now discuss the emergence of conducting edge states in 2DTIs due to the intrinsic property of SOC, starting with the Haldane model. In 1988, F.D.M. Haldane presented a simple model [16] which exhibited a quantized Hall conductance arising purely from the band topology of the system, without the need for an external magnetic field. This was a groundbreaking discovery as it showed that materials in general can exhibit properties such as insulating bulk and conducting edge states due to intrinsic properties rather than external influences. This model therefore laid the foundation for understanding TIs. Although the Haldane model does not consider spin, we will use it as a foundation and extend it to include spin, allowing us to account for SOC.

Haldane considered a honeycomb lattice, the structure of graphene, which consists of two interpenetrating triangular lattices. This provided a simple but effective two-dimensional platform for exploring topological properties. For graphene, the low-energy excitation around the Dirac points $\mathbf{K}$ and $\mathbf{K}'$ can be described by a Dirac-like Hamiltonian[1]

$$H_0 = \hbar v_F \left[\hat{k}_x \tau_z \sigma_x + \hat{k}_y \sigma_y \right], \tag{2.7}$$

which has a linear dispersion relation $E(\mathbf{k}) = \hbar v_F |\mathbf{k}|$. $\tau_z = \pm 1$ includes the valley degree of freedom. Haldane's idea was to start from an already gapped system by considering an extra term that violates $\mathcal{P}$-symmetry[2]

$$\Delta H_{\mathcal{P}} \equiv m_{\mathcal{P}} \sigma_z \,. \tag{2.8}$$

He then tried to break the TRS, as in the quantum Hall effect, to get conducting edge channels and thus quantum Hall plateaus. Only this time, he wanted to break it by an intrinsic quantity rather than by an external magnetic field. He did this by introducing a magnetic field that is zero on average, but has all the spatial symmetries of the honeycomb lattice, and contains a sign whether the electron is jumping to the right or to the left. In the continuum representation, this extra symmetry-breaking term reads

$$\Delta H_{\mathcal{T}} = m_{\mathcal{T}} \sigma_z \tau_z \,. \tag{2.9}$$

To understand why the Haldane model

$$H_{\mathrm{H}} = H_0 + \Delta H_{\mathcal{T}} + \Delta H_{\mathcal{P}} \tag{2.10}$$

[1] In the course of the thesis we drop the hat on any Hamiltonian $\hat{H}$.

[2] In the case of graphene, this parity violation occurs, for example, when two atoms in a unit cell do not have the same mass.

will now exhibit quantum Hall plateaus and therefore edge states, we need to make some topological arguments by again consulting the relationship between the Chern number and the quantum Hall conductance in equation eq. (1.2) and by using a theorem derived by Berry in [6]. It gives a statement for a Hamiltonian of the form

$$H(\mathbf{k}) = \mathbf{d}(\mathbf{k}) \cdot \vec{\sigma}\,, \tag{2.11}$$

which possesses the eigenvalues $\pm|\mathbf{d}(\mathbf{k})| \neq 0$, and we define

$$\mathbf{e_d}(\mathbf{k}) \equiv \frac{\mathbf{d}(\mathbf{k})}{|\mathbf{d}(\mathbf{k})|} \in S^2\,, \tag{2.12}$$

with S^2 being the unit sphere. The theorem says that the integral over the Berry curvature of the system $H(\mathbf{k})$ is given by

$$\int_{T^2} \mathbf{F}\mathrm{d}^2\mathbf{k} = \frac{1}{2}\{\text{solid angle swept by } \mathbf{e_d}(\mathbf{k}) \text{ for } \mathbf{k} \in T\}\,. \tag{2.13}$$

Applying this theorem to the definition of the Chern number and its relation to the conductance, we obtain for the Hall conductance

$$\sigma_{xy} = \frac{e^2}{h}\frac{1}{4\pi}\{\text{solid angle swept by } \mathbf{e_d}(\mathbf{k}) \text{ for } \mathbf{k} \in T\}\,. \tag{2.14}$$

One can see that

$$m_{\mathcal{P}} > m_{\mathcal{T}} \implies \sigma_{xy} = 0\,, \tag{2.15}$$

since in this case for both $\mathbf{K}$ and $\mathbf{K}'$ only one of the poles of the sphere S^2 is visited by $\mathbf{e_d}(\mathbf{k})$, since for both Dirac points we have $d_z > 0$, which gives us a solid angle of 0 and therefore the claim from above. On the other side

$$m_{\mathcal{P}} < m_{\mathcal{T}} \implies \sigma_{xy} = \frac{e^2}{h}\,, \tag{2.16}$$

since $\mathrm{sgn}(d_z) = \pm 1$ has different signs at $\mathbf{K}$ and $\mathbf{K}'$ such that $\mathbf{e_d}(\mathbf{k})$ goes to the north and south pole of the sphere S^2 and wraps around it once completely. With this finite conductance, we expect accompanying edge channels - just as in the regular QHE. The easiest way to understand the emergence of edge states is to consider an interface between two systems with different topologies, a Haldane model with quantum Hall conductance and an insulating one without quantum Hall conductance (which can later be set to be the vacuum). Suppose we are at the valley $\tau = -1$, so the correction in the Haldane model is

$$\Delta H = \Delta H_{\mathcal{P}} + \Delta H_{\mathcal{T}} = (m_{\mathcal{P}} - m_{\mathcal{T}})\sigma_z \equiv m'\sigma_z\,. \tag{2.17}$$

As introduced earlier, the distinction between the topologies is given by $m' > 0$

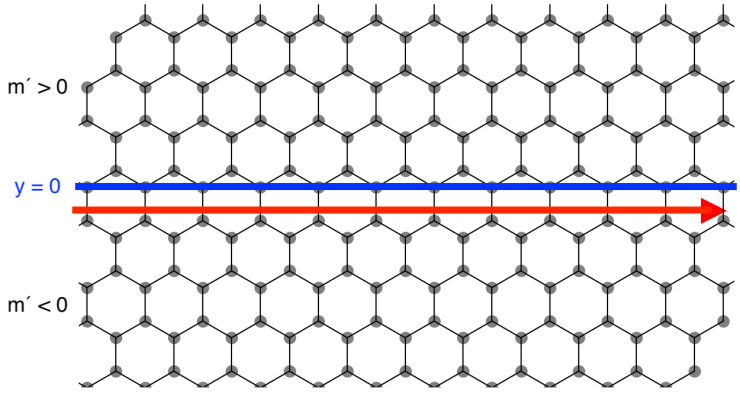

Figure 2.1: Interface between graphene lattices with different topological phases

Interface at $y = 0$ (blue line) between two graphene honeycomb lattices described by the Haldane model eq. (2.10) with different topological phases m'. Due to the topological phase change, we obtain edge states (red line) located around the boundary $y = 0$. The appearance of edge states does not require an external magnetic field.

for the trivial case and $m' < 0$ for the quantum Hall case. We therefore introduce a system that is translation invariant along the x axis, while along the y axis the topology changes from quantum Hall to trivial, with the interface at $y = 0$, as shown in Figure 2.1. We thus define a mass $m'(y)$ which depends on the coordinate y and has the properties $m'(y > 0) > 0$ and $m'(y < 0) < 0$. To solve this problem, one makes the Ansatz

$$\psi_{k_x;n}(x, y) = \exp(ik_x x)\psi_n(y)\,. \tag{2.18}$$

To understand the emergence of edge states, one focuses on the lowest band, i.e., $n = 0$. The solution to this problem was treated long ago in the Jackiw-Rebbi model [17], which states that in a 1D system with a boundary where the mass changes sign, there is a zero energy solution which reads

$$\psi_{n=0}(y) = \exp\left\{ -\int_0^y \frac{m'(y')}{v_F} dy' \right\} |x\pm\rangle\,, \tag{2.19}$$

where $|x\pm\rangle$ are the eigenstates of σ_x corresponding to the eigenvalues ± 1. The choice between $|x+\rangle$ and $|x-\rangle$ depends on whether the mass $m'(y)$ changes from $+$ to $-$ or vice versa. For us, this means that since there is a zero energy solution in the y direction $\psi_{n=0}(y)$, the lowest energy of the Ansatz is

$$H_{\mathrm{H}}\psi_{k_x;n=0}(x, y) = \epsilon_{n=0}(k_x)\psi_{k_x;n=0}(x, y)\,, \tag{2.20}$$

with

$$\epsilon_{n=0}(k_x) = \hbar v_F k_x \,. \tag{2.21}$$

As can be seen in Figure 2.2, this single band describing edge states connects the

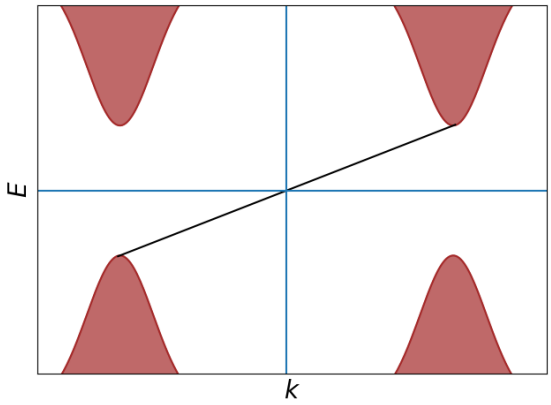

Figure 2.2: Gap inversion induced by TRS breaking

The colored regions show the bulk conductance and valence bands, which form continuum states in the model shown in Figure 2.1. An edge state connects the valence band at **K** to the conductance band at **K′** with a positive group velocity.

valence and conductance bands between the points **K** and **K′**. To connect the other two bulk bands we need another interface at some $y < 0$, describing a system going from topologically trivial to quantum hall. Therefore the mass $m'(y)$ changes now the other way round, giving us the same spectrum as before only with an additional minus

$$\epsilon_{n=0}(k_x) = -\hbar v_F k_x, \,. \tag{2.22}$$

As one can see, we are approaching the description of TIs, materials that close the conductance gap by edge/surface states. It may seem strange that we have taken into account the violation of TRS when it was stated at the beginning that TIs are materials known to preserve this precise symmetry. One way to consider this and correctly describe TIs is to include the spin degree of freedom of the electrons and thus arrive at the quantum spin Hall effect (QSHE) and hence the Kane and Mele model. This freedom allows us to incorporate a mass term ΔH_{SO} instead of eq. (2.9), which arises from SOC and thus leaves TRS untouched. In the continuum model this term reads

$$\Delta H_{\mathrm{SO}} = m_{\mathrm{SO}} \sigma_z \tau_z s_z \,, \tag{2.23}$$

where $s_z = \pm 1$ represents the spin. This gives us the definition of the new mass term $m' \equiv m_{\mathcal{P}} - \tau s_z m_{\mathrm{SO}}$. Since introducing spin into the Hamiltonian basically

gives us two copies of the Haldane model from before, we can immediately state this system at hand will have gapless edge states! Moreover, taking into account the spin, the lowest energy states from eq. (2.18) now includes the spin part and reads

$$\psi_{k_x;n=0}(x,y) \otimes \chi \,, \tag{2.24}$$

where χ is the spin wave function representing spin-up $\uparrow$ or spin-down $\downarrow$ with eigenvalues ± 1. By looking at the new definition of m', one realizes that the mass change $m'(y)$ is opposite for spin-down compared to spin-up. Therefore for spin-up we get

$$\epsilon_{n=0;\uparrow}(k_x) = \hbar v_F k_x \tag{2.25}$$

and for spin-down

$$\epsilon_{n=0;\downarrow}(k_x) = -\hbar v_F k_x \,. \tag{2.26}$$

This leads to the property of spin-momentum locking that we talked about earlier which is encompassed by the fact that the up and down spin propagate in opposite directions, greatly improving the stability of these states as back-scattering from non-magnetic impurities is now forbidden.

It is worth remembering that TIs are materials whose electronic properties appear to be very robust to impurities and other defects and deformations. However, there are a large number of materials with strong SOC that are trivial insulators and lack these robust electronic properties. How do these materials differ from TIs? As mentioned earlier, their distinct robustness suggests a deeper, topological reason. We ask which topological property of the band structure indicates whether a physical system with TRS is trivial or a topological insulator. The answer to this question leads to the so-called $\mathbb{Z}_2$ invariant. In order to understand this special class of materials, one needs to understand the implications of TRS on the band structure, which is given by Kramer's theorem. It states that all eigenstates of a Hamiltonian H with TRS are at least twofold degenerate. This has major implications for the band structure of a system. Let us look at a generic band structure of the 1D edge states of a 2D time-reversal insulator, see Figure 2.3. We see that since the points $k_x = 0$ and $k_x = \pi/a$ are the same[1] after a time reversal transformation $\mathcal{T}$, Kramers' theorem requires that the energy at these points is twofold degenerate, while for all other points this of course need not be the case. In fact, because of SOC, their degeneracy is split. Consequently, a band structure can have the states at the points $k_x = 0$ and $k_x = \pi/a$ connected in pairs, as in plot a), or not in pairs, as in plot b). As a result, one could eliminate the edge states in plot a) by pushing them out of the gap giving us a trivial insulator. While in plot b) one cannot eliminate the states because by pushing them, say, up in the energy, there would have to be states added from below to ensure that the Fermi energy always cuts an

[1] since $k_x = \pm\pi/a$ describe the same point in the Brillouin zone.

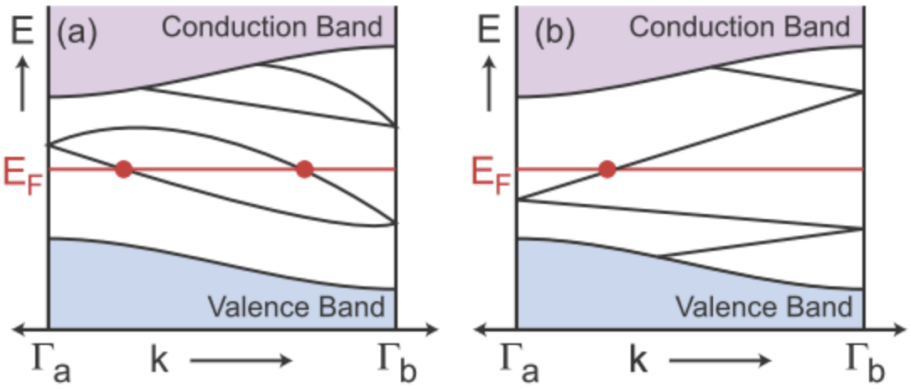

Figure 2.3: Trivial vs. Topological Insulator

The figure is taken from [15]. It shows two types of dispersion relations between two Krammers degenerate points of a material satisfying TRS (e.g., $\Gamma_a = 0$ and $\Gamma_b = \pi/a$ in a 2D rectangular Brillouin zone). For a given Fermi energy, an odd number of crossings results in topological protection of the edge states.

uneven number of states, resulting in a TI. These are the only two cases that can occur in the band structure, and so we can characterize time-reversal insulators by determining whether we have the case shown in plot a) trivial insulator or plot b) topological insulator. This can be defined mathematically rigorously [18], giving us the $\mathbb{Z}_2$-invariant ν, which can take the values $\nu = 1$ (topological insulator) or $\nu = 0$ (trivial insulator).

At this point, one might rightly point out that graphene has a very weak SOC, which is why it does not play a significant role in most physical cases. Given that the previous derivations have considered SOC in graphene, one might wonder about the purpose of this analysis. However, in various gapped TI materials with strong SOC, a SOC-induced band inversion occurs [19] in the same way as described in the graphene example above.

Therefore, the Kane and Mele model serves as a simplified yet powerful framework for understanding the general mechanism of SOC-induced band inversion in 2DTIs - a mechanism consisting of edge states described by the massless Dirac Hamiltonian

$$H = \hbar v_F \hat{k}_x \sigma_x \,. \tag{2.27}$$

Having derived the defining properties of 2DTIs and demonstrated the presence of gapless edge states, one can extend this analysis by considering the Fu-Kane-Mele model [20], which generalizes the QSHE to three dimensions. Consequently, in the three dimensional case, we obtain conducting surface states instead of edge states.

This extension arises from similar considerations regarding topology and SOC, but with more subtle differences regarding the $\mathbb{Z}_2$-invariant. While 2DTIs are described by a single invariant, 3DTIs are characterized by four invariants: ν_0, ν_1, ν_2, ν_3. In the special case $\nu_0 = 1$ for so-called "strong" 3DTIs, which we assume in this work, the surface states are robust and, in the same way as in the 2DTI case, they are described by the massless Dirac Hamiltonian, only this time in two dimensions

$$H = \hbar v_F \left[\hat{k}_x \sigma_x + \hat{k}_y \sigma_y \right]. \tag{2.28}$$

3 Curved 3DTI

In this chapter we outline how to extend the massless Dirac Hamiltonian eq. (2.28) to curved spaces.

So far we have considered the case of 3DTIs with a flat surface, i.e. particles moving on insulator surfaces with no intrinsic curvature. Since we are interested in studying the transport and spectral properties of electrons on *curved* topological insulators, we will first give a mathematical description of spin-$\frac{1}{2}$ particles on such curved TIs. We thus want to allow the particles to move on curved surfaces with some non-trivial spatial curvature (such as cones, spheres, etc.) while keeping time flat. To do this, we need to find a Dirac Hamiltonian like eq. (2.28), but generalised to curved 2D surfaces. The starting point of our analysis is the massless Dirac equation in $(2+1)$-dimensional flat spacetime dimensions

$$i\gamma^\mu \partial_\mu \Psi = 0\,, \tag{3.1}$$

from which the Dirac Hamiltonian eq. (2.28) is derived. Here we use Einstein's summation convention, where $\mu = 0$ is the time direction, while $\mu = 1, 2$ is the space direction. The matrices γ^μ are two-dimensional matrices satisfying the Dirac algebra

$$\{\gamma^\mu, \gamma^\nu\} = 2\delta_{\mu\nu}\,, \tag{3.2}$$

where $\delta_{\mu\nu}$ is the Kronecker delta and $\{\cdot,\cdot\}$ is the anti-commutator. Throughout the thesis we will use the matrices as follows

$$\gamma_0 = -i\sigma_z\,, \gamma_1 = \sigma_y\,, \gamma_2 = \sigma_x\,. \tag{3.3}$$

In the flat case the underlying space-time metric reads

$$\eta_{\mu\nu} = \mathrm{diag}(-1, 1, 1)\,. \tag{3.4}$$

Now, when passing to curved surfaces, two things will happen. First, the flat metric will transform into some non-trivial and generally space-dependent metric $\eta_{\mu\nu} \to g_{\mu\nu}(x_\sigma)$. Second, the trivial derivative $\partial_\mu \to D_\mu$ will transform into a covariant derivative to provide a way to differentiate spinors in a manner that respects the geometry of the space. The covariant Dirac equation then becomes

$$i\gamma^a e_a^\mu D_\mu \Psi = 0\,. \tag{3.5}$$

The covariant Dirac equation eq. (3.5) and the covariant derivative D_μ are explained and rigorously derived in [21]. The local coordinate representation of D_μ reads

$$D_\nu = \partial_\nu + \frac{1}{8}\hat{\omega}_{\mu\sigma\nu}[\gamma^\mu, \gamma^\sigma]\,, \tag{3.6}$$

where $[\cdot,\cdot]$ describes the commutator and $\hat{\omega}_{\mu\sigma\nu}$ the spin-connection term

$$\hat{\omega}_{\nu}^{\mu\sigma} = e_{\rho}^{\mu}\Gamma_{\alpha\nu}^{\rho}e^{\alpha\sigma} + e_{\rho}^{\mu}\partial_{\nu}e^{\rho\sigma}\,, \tag{3.7}$$

where $\Gamma_{\alpha\nu}^{\rho}$ are the Christoffel symbols and $e^{\lambda\sigma}$ the vielbein field, defined through $g_{\mu\nu} = e_{\mu}^{a}e_{\nu}^{b}\eta_{ab}$.

While these relations are general for any kind of curved surface, we want to focus our investigations on a special class of curved surfaces, namely surfaces of revolution, which promise a drastic simplification of the underlying calculations. A surface of revolution can be parametrized by the arc length and azimuthal angle (s,φ), which gives us the parametrization $\mathbf{\Sigma}$

$$\begin{aligned} \mathbf{\Sigma} &: (s_0, s_1) \times (0, 2\pi] \to \mathbb{R}^3 \\ \mathbf{\Sigma} &: (s,\varphi) \to \begin{pmatrix} r(s)\cos(\varphi) \\ r(s)\sin(\varphi) \\ z(s) \end{pmatrix}\,, \end{aligned} \tag{3.8}$$

where $r(s)$ is the arc length dependent radius of revolution. We can have bounded and as well unbounded radii, i.e.

$$r_{\min} \leq r(s) \leq r_{\max}\,, \tag{3.9}$$

with $r_{\min} \in \mathbb{R}_0^+$ and $r_{\max} \in \mathbb{R}^+ \cup \{+\infty\}$. To simplify future considerations we also assume the function

$$r : [s_0, s_1] \mapsto [r_{\min}, r_{\max}] \tag{3.10}$$

to be bijective[1] and consequently monotonous. An example of such a surface is shown in Figure 5.6. With this constrains and the parametrization eq. (3.8) in mind, we further simplify the notation and denote the coordinate indices by the coordinate that they describe $\mu = (0,1,2) \equiv (t,s,\varphi)$. The last important element in our mathematical setup is the relation between the $z(s)$ coordinate and the radius $r(s)$, which reads as follows

$$\left(\frac{\mathrm{d}z}{\mathrm{d}s}\right)^2 + \left(\frac{\mathrm{d}r}{\mathrm{d}s}\right)^2 = 1 \tag{3.11}$$

and is derived in Appendix A. This relation allows us to translate a given radial profile $r(s)$ into its real space $z(s)$ coordinate and vice versa. In addition, it imposes the constraints

$$z'(s)^2 \leq 1 \text{ and } r'(s)^2 \leq 1 \tag{3.12}$$

[1]We therefore exclude the case of constant radius $r_{\min} = r_{\max}$, since such surfaces have already been extensively studied in [23]. Furthermore, in the case of a bijective radius function $r(s)$, one could also parametrize the surfaces by the radius and azimuthal angle (r,φ). For this different parametrization, a derivation of the Dirac Hamiltonian was performed in [22].

on any surface of revolution. Using these ingredients in some lengthy calculations in Appendix A we arrive at the space-time metric

$$g_{\mu\nu} = \mathrm{diag}(-v_F^2, r(s)^2, 1) \tag{3.13}$$

and the only non-zero spin-connection term, which reads

$$\hat{\omega}_{\varphi}^{\varphi s} = \frac{\mathrm{d}r}{\mathrm{d}s} = -\hat{\omega}_{\varphi}^{s\varphi}\,. \tag{3.14}$$

Thus, the covariant derivative becomes

$$\begin{aligned} D_t &= \partial_t \\ D_\varphi &= \partial_\varphi + \frac{i}{2}\hat{\omega}_{\varphi}^{\varphi s}\sigma_z \\ D_s &= \partial_s\,. \end{aligned} \tag{3.15}$$

Since we will later be interested in the formation of Landau levels and magneto-transport simulations, we now want to introduce a magnetic field into the system. At this point, one could rightly point out that introducing a magnetic field would destroy the TRS of the material, which is the very reason for the topological protection of the surface states. However, as long as the violation of this symmetry is not too severe, in some cases the surface states survive and are still protected. For example, in [24] it is has been shown that mercury telluride quantum wells in a magnetic field retain their topological insulating properties even under the application of a strong magnetic field. In addition, it should be noted that although we will consider magnetic fields, for simplicity we will not consider Zeeman terms. To introduce the homogeneous B-field into our system, we use cylindrical coordinates along the axis of revolution, in our case the z-axis

$$\mathbf{B} = B\mathbf{e}_z\,, \tag{3.16}$$

giving us the vector potential

$$\mathbf{A} = A_\varphi \mathbf{e}_\varphi = \frac{Br(s)}{2}\mathbf{e}_\varphi\,, \tag{3.17}$$

where $\nabla \times \mathbf{A} = \mathbf{B}$ is obtained by expressing ∇ in cylinder coordinates. To introduce the effect of the vector potential, we need to use minimal coupling. This involves adding the vector potential to the associated momentum operator, which in our case reads

$$\hat{p}_\varphi = \hbar\hat{k}_\varphi = -i\hbar e_\varphi^\varphi \partial_\varphi = -i\hbar\frac{\partial_\varphi}{r(s)} \tag{3.18}$$

and hence

$$-i\hbar\frac{\partial_\varphi}{r(s)} = \hat{p}_\varphi \to \hat{p}_\varphi + eA_\varphi = -i\hbar\frac{\partial_\varphi}{r(s)} + eA_\varphi\,, \tag{3.19}$$

where $e > 0$. This transformation boils down to

$$\partial_\varphi \to \partial_\varphi + i\frac{e}{\hbar}r(s)A_\varphi\,. \tag{3.20}$$

We therefore arrive at the final form of the derivatives

$$\begin{aligned} D_t &= \partial_t \\ D_\varphi &= \partial_\varphi + \frac{i}{2}\hat{\omega}_\varphi^{\varphi s}\sigma_z + i\frac{e}{\hbar}r(s)A_\varphi \\ D_s &= \partial_s\,. \end{aligned} \tag{3.21}$$

Having this, using the covariant Dirac equation eq. (3.5) and assuming stationary states

$$\Psi(t,s,\varphi) = \psi(s,\varphi)e^{i\epsilon t/\hbar} \tag{3.22}$$

we arrive (see Appendix C for detailed calculations) at the Dirac Hamiltonian H on general surfaces of revolution under a coaxial magnetic field, where we recall that we **dropped the hat** for convenience

$$H\psi(s,\varphi) = \epsilon\psi(s,\varphi) \tag{3.23}$$

$$H = \hbar v_F\left[i\sigma_y\frac{1}{r(s)}\left(\partial_\varphi + i\frac{e}{\hbar}r(s)A_\varphi\right) - i\sigma_x\left(\partial_s + \frac{r'(s)}{r(s)}\frac{1}{2}\right)\right]. \tag{3.24}$$

To make the equations easier to handle, we want to get rid of the spin-connection term $r'(s)/2r(s)$. This is done by introducing the transformed Hamiltonian[1]

$$\tilde{H} = \sqrt{r(s)}H\frac{1}{\sqrt{r(s)}} = \hbar v_F\left[i\sigma_y\frac{1}{r(s)}\left(\partial_\varphi + i\frac{e}{\hbar}r(s)A_\varphi\right) - i\sigma_x\partial_s\right]. \tag{3.25}$$

Since dealing with dimensionless variables is simpler, we set the length scale of the system to be a and factor it out of eq. (3.25) to obtain

$$\tilde{H} = \frac{\hbar v_F}{a}\left[i\sigma_y\frac{1}{\bar{r}(s)}\left(\partial_\varphi + i\frac{a^2eB}{2\hbar}\bar{r}^2(s)\right) - i\sigma_x\partial_{\bar{s}}\right], \tag{3.26}$$

where we generally denote rescaled variables as in the following examples

$$\bar{r} = \frac{r}{a} \quad \bar{r}_{\min} = \frac{r_{\min}}{a} \quad \bar{s} = \frac{s}{a}\,, \tag{3.27}$$

[1]The Hamiltonian H from eq. (3.24) and the rescaling trick in eq. (3.25) were presented in [23], but without the detailed derivations.

and so on. A typical length scale in nanowires is around $a \sim 50\text{nm}$. Geometrically, $1/a^2$ describes the characteristic scale of the system's curvature[1]. From now on, we will only deal with $\tilde{H}$ to examine its single particle spectrum. Whenever we find a solution of

$$\tilde{H}\tilde{\psi}(s,\varphi) = \epsilon\tilde{\psi}(s,\varphi) \tag{3.28}$$

we can translate it to a solution of

$$H\psi(s,\varphi) = \epsilon\psi(s,\varphi) \;\text{ with }\; \psi(s,\varphi) = \frac{1}{\sqrt{r(s)}}\tilde{\psi}(s,\varphi)\,. \tag{3.29}$$

Consequently, the transformation eq. (3.25) leaves the spectrum unchanged, making $\tilde{H}$ optimal to study the single particle spectrum of H. Since we are only dealing with $\tilde{H}$, from now on we will also **drop the tilde**, so that whenever we write H and $\psi(s,\varphi)$ we mean $\tilde{H}$ and $\tilde{\psi}(s,\varphi)$. Moreover, we **drop the bar** from the rescaled variables, so that whenever we write r, s and r_{min} we mean $\bar{r}$, $\bar{s}$ and $\bar{r}_{\text{min}}$ and so on. Furthermore, we express the energies ϵ in terms of the natural energy scale

$$\mathcal{E} = \frac{\hbar v_F}{a}\,, \tag{3.30}$$

which is given as a prefactor in eq. (3.26). Therefore, it can be omitted in the Hamiltonian. Altogether, the overall rescaled Hamiltonian eq. (3.26), which we will deal with throughout the thesis, reads

$$H = \left[i\sigma_y \frac{1}{r(s)}\left(\partial_\varphi + i\frac{\Phi}{\Phi_0}r^2(s)\right) - i\sigma_x\partial_s\right], \tag{3.31}$$

where we introduced the flux $\Phi = \pi a^2 B$ and flux quanta $\Phi_0 = h/e$. Since we are dealing with surfaces of revolution, we can take advantage of this symmetry and build a sensible Ansatz for the eq. (3.31). There we need to take into account the nature of the spin-$\frac{1}{2}$ particle, which flips its spin after a full 360° rotation and thus acquires a quantum mechanical phase factor when it orbits the surface of revolution once. This effect is implemented as an anti-periodic boundary condition (BC) in the angular part $\psi(s,\varphi+2\pi) = -\psi(s,\varphi)$, leading to the Ansatz

$$\psi(s,\varphi) = e^{i(m+1/2)\varphi}\psi(s) \;\text{ with }\; m \in \mathbb{Z} \tag{3.32}$$

and the notation

$$\psi(s) = \begin{pmatrix}\psi_\uparrow(s)\\ \psi_\downarrow(s)\end{pmatrix}\,. \tag{3.33}$$

[1] In our considerations, this refers to the Gaussian curvature, which will be introduced in Chapter 5.1.

With this, eq. (3.28) becomes

$$\begin{aligned} \boldsymbol{L}\psi(s) &= \epsilon\psi(s) \\ \boldsymbol{L} &\equiv \begin{pmatrix} 0 & \hat{L}^{+} \\ \hat{L}^{-} & 0 \end{pmatrix} , \end{aligned} \tag{3.34}$$

where we introduced the differential operator

$$\hat{L}^{\pm} = i(-\partial_s \pm V(s)) \,, \tag{3.35}$$

containing the effective mass potential

$$V(s) = \frac{\alpha_m}{r(s)} + \beta r(s) \,. \tag{3.36}$$

For convenience, we use the notation

$$\alpha_m \equiv m + \frac{1}{2} \text{ and } \beta \equiv \frac{\Phi}{\Phi_0} \,, \tag{3.37}$$

which we will refer to as the angular momentum quantum number and magnetic flux for simplicity and use throughout the whole thesis. We emphasize the supersymmetric structure of the differential equation eq. (3.34), see for example in [25].

4 Numerical Methodologies

Among other things we are interested in computing the bound state solutions of eq. (3.34). Since analytical solutions are not always accessible, we have to resort to numerical approaches. Nevertheless, even when analytical expressions of the solutions exist, it is useful to check their correctness and validity by comparing them with numerical calculations. Therefore, in this chapter, we will introduce the standard methodology in the numerical study of Dirac particles.

First, we aim to discretize the space to facilitate the use of linear algebra methods. This discretization scheme is also essential for the quantum transport simulations discussed in Chapter 6. Second, we address a common numerical problem associated with Dirac-like equations: Fermion doubling, and how to circumvent it. We also explore the boundary conditions for Dirac particles. Unlike Schrödinger particles, Dirac particles cannot have a vanishing wave function on both sides of a domain, necessitating alternative physical boundary conditions.

4.1 Tight-Binding Calculations

To treat the problem numerically and compute for example bound states, we consider the differential equation eq. (3.34) on the grid, i.e. we discretize the parameter space into L points along the arc length coordinate s, namely

$$\begin{aligned} s &\in (s_0, s_1) \\ \rightarrow s_i &\in \{s_0, s_1 + \Delta s, s_0 + 2\Delta s, \ldots, s_1\}\,, \end{aligned} \tag{4.1}$$

where we denote the lattice spacing by

$$\Delta s = \frac{s_1 - s_0}{L}\,. \tag{4.2}$$

By this, and by using finite symmetric difference[1] the derivative contained in eq. (3.34) becomes

$$\partial_s \psi(s_i) \rightarrow \frac{\psi_{i+1} - \psi_{i-1}}{2\Delta s}\,, \tag{4.3}$$

where $\psi_i = \psi(s_i)$. With this, we are ready to write down the discretized version of eq. (3.34)

$$\frac{-i\sigma_x}{2\Delta s}(\psi_{i+1} - \psi_{i-1}) - \sigma_y V_i \psi_i = \epsilon \psi_i\ , \tag{4.4}$$

[1] Forward or backward difference would not be adequate, since they do not preserve the hermicity of H.

again using the notation $V(s_i) = V_i$. Eq. (4.4) can be rewritten in matrix form

$$\begin{pmatrix} d_1 & t_s & 0 & \cdots & 0 \\ t_s^* & d_2 & t_s & \ddots & \vdots \\ 0 & t_s^* & d_3 & \ddots & 0 \\ \vdots & \ddots & \ddots & \ddots & t_s \\ 0 & \cdots & 0 & t_s^* & d_L \end{pmatrix} \begin{pmatrix} \psi_1 \\ \psi_2 \\ \vdots \\ \vdots \\ \psi_{L-1} \\ \psi_L \end{pmatrix} = \epsilon \begin{pmatrix} \psi_1 \\ \psi_2 \\ \vdots \\ \vdots \\ \psi_{L-1} \\ \psi_L \end{pmatrix}, \tag{4.5}$$

where

$$t_s = \frac{-i\sigma_x}{2\Delta s} \text{ and } d_i = -\sigma_y V_i \,. \tag{4.6}$$

Eq. (4.5) is now simply an eigenvalue problem, and we can solve for the energies and wave function using any standard eigenvalue solver routine, such as *scipy.sparse.linalg*. Note that in this form the matrix equation imposes inherently hard-wall boundary conditions[1] on ψ. At this point we also note that the numerical lattice reassembles the structure of a tight binding model on an atomic lattice. Therefore, for simplicity, we adopt the notation from tight binding models

$$\boldsymbol{L} = \sum_i t_s |i\rangle\langle i+1| + \frac{d_i}{2}|i\rangle\langle i| + \text{h.c.}\,. \tag{4.7}$$

The term $t_s|i\rangle\langle i+1|$ represents the hopping between sites i and $i+1$ with hopping amplitude t_s, while $d_i/2|i\rangle\langle i|$ acts as an effective on-site mass term. It is only the similar mathematical structure that motivates this notation, not any physical similarity. And the reason why this mathematical structure is of interest to us is that it remains easy to handle even when we introduce more than one degree of freedom, whereas the matrix notation in eq. (4.5) becomes unwieldy to handle.

If we want to have both degrees of freedom and intend to discretize the original Hamiltonian eq. (3.31) by additionally discretizing the angular coordinate φ into W points, we get the following tight-binding model by the same procedure as above

$$H = \sum_{ij} t_s |i,j\rangle\langle i+1,j| + t_\varphi(s_i)|i,j\rangle\langle i,j+1| + \text{h.c.}\,, \tag{4.8}$$

with

$$t_\varphi(s_i) = i\sigma_y \frac{1}{2r(s_i)\Delta\varphi} \quad \text{and} \quad \Delta\varphi = \frac{2\pi}{W}\,. \tag{4.9}$$

[1]This is due to the fact that the matrix is truncated at some point, leaving us, for example in the first row with only one forward hopping term t_s while the backward hopping was assumed to be zero.

Note that in this discretization scheme[1] we have not included the magnetic field, as in tight-binding models it should not be included as an on-site potential, but rather in the hopping amplitudes, which leads us to the Peierl's phase.

Peierl's phase To correctly implement magnetic fields in tight-binding models, the hopping terms in eq. (4.9), must be modified by the accumulated phase factor

$$t_{ij} \to t_{ij} \exp\left(\frac{ie}{\hbar}\int_{\mathbf{r}_i}^{\mathbf{r}_j} \mathbf{A}\cdot d\mathbf{l}\right) . \tag{4.10}$$

This is called the Peierl's phase and is discussed in [26]. Since in our case our vector potential has the form

$$\mathbf{A} = A_\varphi \mathbf{e}_\varphi \,, \tag{4.11}$$

we obtain the modification

$$t_\varphi(s_i) \to t_\varphi(s_i)\ \exp\left(i\beta r(s_i)^2 \frac{2\pi}{W}\right) . \tag{4.12}$$

Another important detail not to be overlooked is that, as mentioned before, due to the spin-$\frac{1}{2}$ nature we need to impose anti-periodic boundary conditions on $\psi(s,\varphi)$ in the φ-direction. In the tight-binding scheme this is done by simply adding a minus to the hoppings

$$|i,1\rangle\langle i,W| \to -|i,1\rangle\langle i,W| \,. \tag{4.13}$$

Overall, we will use this discretized version of the Hamiltonian eq. (4.8) including Peierl's phase and anti-periodic BC at a later point in Chapter 6. Until then, we will only deal with the reduced problem eq. (4.7), diagonalizing it whenever necessary.

4.2 Fermion Doubling

As already mentioned, before finding its place in low-energy condensed matter physics, the Dirac equation was first introduced in the context of high-energy physics. Thus, not only its strengths were transferred to condensed matter physics, but also its limitations. One of these is its behavior under discretization of the lattice. When discretizing a lattice describing Dirac-Fermions, one additionally obtains spurious, non-physical, solutions, which alter any physical observable, such as energy. This is best illustrated by choosing the simplest system in which spurious

[1] In eq. (4.7) we included the magnetic field as an on-site potential because we did not discretize the coordinate in which the magnetic field was included by minimal coupling, i.e. the φ direction. This is no longer the case here, since we discretize φ.

solutions occur, namely in eq. (4.4), and as a proof of concept we chose $V(s) = 0$. We therefore have for the continuum Hamiltonian

$$H = \sigma_x \hat{k}_s \,, \tag{4.14}$$

while for its discretized version we obtain

$$\epsilon\psi_j = H\psi_j = \frac{-i\sigma_x}{2\Delta s}(\psi_{j+1} - \psi_{j-1}) \,. \tag{4.15}$$

By making the plain wave Ansatz

$$\psi_j \propto e^{ik_s j\Delta}\chi \,, \tag{4.16}$$

with the spin wave function χ, we get for the tight-binding eigenvalue

$$\epsilon_{\mathrm{TB}}(k_s) = \pm\frac{1}{\Delta s}|\sin(k_s\Delta s)| \,. \tag{4.17}$$

For small k_s, this is clearly consistent with the actual continuum Dirac spectrum

$$\epsilon_{\mathrm{cont}}(k_s) = \pm|k_s| \,, \tag{4.18}$$

while for bigger k_s the spectra differ significantly. This has the consequence that

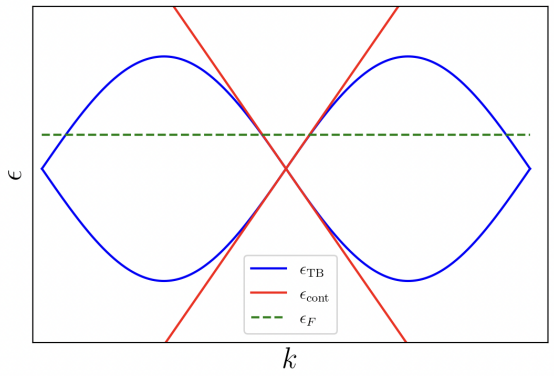

Figure 4.1: Fermion doubling in Dirac systems

The plot shows the energy of the continuous 1D Dirac model eq. (4.14) compared to that obtained by the tight-binding formulation eq. (4.15). For a given Fermi energy ϵ_F, the tight-binding model yields additional spurious solutions, leading to incorrect physical quantities in simulations.

for a given Fermi energy ϵ_F we get two times more modes than in the continuum case (see Figure 4.1), which leads to incorrect physical results. Therefore, there is

a great need for a method to avoid this numerical problem. One way to solve this problem is to introduce a small quadratic correction to the Dirac Hamiltonian

$$H = \sigma_x \hat{k}_s + \zeta \hat{k}_s^2 \sigma_z \,. \tag{4.19}$$

This term, called Wilson's mass term, is introduced in [27] and its consideration is a standard procedure in high-energy physics. To see its effect on the spectrum, we again discretize the Hamiltonian by finite symmetric difference and calculate its spectrum using the same plain wave Ansatz eq. (4.16), which yields

$$\epsilon_{\mathrm{TB}}^{\zeta} = \pm\sqrt{\frac{1}{\Delta s^2}\sin(k_s \Delta s)^2 + \zeta^2 \frac{4}{\Delta s^2}[1-\cos(k_s \Delta s)]^2} \,. \tag{4.20}$$

As can be seen in Figure 4.2, adding this term opens a gap $\delta = 4\zeta\ /\Delta s^2$, which

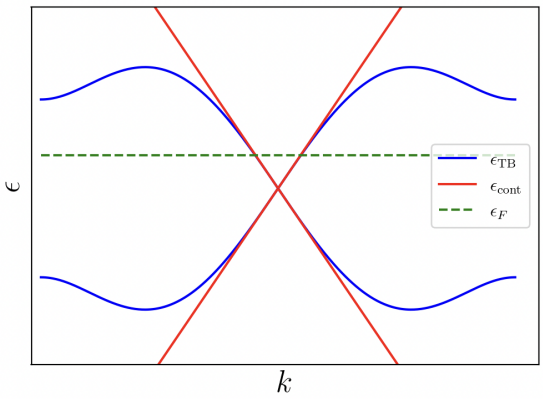

Figure 4.2: Effect of Wilson's mass term in Dirac systems

The introduction of Wilson's term eq. (4.19) removes the spurious solutions from Figure 4.1. The gap opened amounts to $\delta = 4\zeta\ /\Delta s^2$.

solves our initial problem. Now at some low Fermi energy ϵ_F we see that by adding Wilson's term we no longer cut off four energy points but only two, which is physically correct. The whole discussion still holds even in the case of a non-zero potential $V(s)$, since it does not contain any momentum dependence k_s and thus the spurious solutions are not affected by it. Therefore, we will tacitly make use of Wilson's term in our numerical computations, unless otherwise stated.

4.2.1 Boundary Conditions

We now address another subtle implementation problem regarding the BC in Dirac systems, a problem which turns out to be solved whenever the Fermion doubling problem is solved. Dirac systems, which are by nature coupled differential equations

of first order, have the disadvantage that one cannot impose more than one Dirichlet boundary condition on the wave function ψ from eq. (3.34). This means that we cannot require a vanishing $\psi = 0$ at two borders simultaneously [28], as one would be familiar with in the case of a Schrödinger particle in a 1-dimensional box. However, this issue is crucial in our systems, since we have systems which are cut at two sides (see Figure 6.2). One way to tackle this problem is by demanding a weaker boundary condition at the borders, namely vanishing current density $j = 0$. In [29] it is shown that for our Dirac equation eq. (4.14) from before, an easy way to demand the current density to vanish at the two borders $s^- \equiv s_0$ and $s^+ \equiv s_1$ is via the condition

$$\big[i\sigma_x \pm \sigma_y\big]\psi(s^\pm) = 0 \implies j(s^\pm) = 0\,. \tag{4.21}$$

While mathematically this can be demanded without concerns, numerically it poses a problem. The discretized Hamiltonian eq. (4.4) was solved by translating it to a matrix equation and then diagonalizing it numerically. However, translating a continuum eigenvalue equation to a discretized matrix version allows only a few types of boundary conditions[1] under which a current preserving BC does not fall. Fortunately in the same paper [29] the authors manage to figure out that demanding current preserving BC eq. (4.21) at low energies in the Dirac Hamiltonian eq. (4.14) is equivalent to demanding hard-wall BC from a slightly changed Hamiltonian. In other words the following two systems are equivalent

$$H_1 = \sigma_x \hat{k}_s \quad \text{with} \quad \big[i\sigma_x \pm \sigma_y\big]\psi(s^\pm) = 0 \tag{4.22}$$

$$H_2 = \sigma_x \hat{k}_s + m\hat{k}_s^2\sigma_z \quad \text{with} \quad \psi(s^\pm) = 0\,, \tag{4.23}$$

for some mass term m. Surprisingly, this is Wilson's mass term discussed in the previous section. This is ideal, since we intended either way to implement this term, to solve the Fermion doubling problem, remember? The additional nice effect is that now by this term we also ensure that the boundary conditions imposed by the numerical scheme work fine with the model.

To summarize, at low energies including Wilson's term in our computation gets rid of Fermion doubling and ensures that the inherent hard-wall BC of the numerical algorithm implements the mathematically correct current vanishing condition $j = 0$ - all simultaneously!

[1] In our case hard-wall, other possible BC are periodic or anti-periodic.

5 Bound States Analysis

In this chapter, we will analyze the bound states on various surfaces of revolution characterized by different Gaussian curvatures K. This investigation aims to enhance our understanding of the effects of curvature on confined Dirac Fermions. Specifically, we will examine three distinct cases of Gaussian curvature:

$$K = 0,\ K = -1 \text{ and } K = 2 - 2r^2\,. \tag{5.1}$$

Notably, the zeroth energy level can be solved for any surface of revolution, irrespective of the surface's specifics or its curvature. This universal solvability stems from the super symmetric structure of the governing equations, as shown in eq. (3.34).

In addition, this chapter introduces the concept of a reciprocal surface - a surface which is related to an initial surface by a particular transformation. Using this relationship, we can determine the spectra and wave functions of this reciprocal surface based on the solutions of the original surface, allowing us to calculate solutions once and use them to describe a second system without additional computation.

5.1 Solutions for Different Gaussian Curvatures K

First we present a brief reminder of the Gaussian curvature K and how it is calculated on surfaces of revolution. A more detailed description can be found in [30]. Afterwards, we will look at the zeroth energy level on general surfaces of revolution and ask the question, whether it exists and, if so, how it can be computed. We therefore derive an existence condition for these states and extend it to a existence condition for excited states. We also clarify the procedure of explicit calculation of excited states.

In general, the Gaussian curvature on arbitrary two-dimensional surfaces describes how much the surface bends by measuring the product of the principal curvatures at a given point. Mathematically, it is defined as

$$K = \frac{\det(\mathrm{II})}{\det(\mathrm{I})}\,, \tag{5.2}$$

where I and II are the first and second fundamental form, respectively, see Appendix B for their local coordinate representation. And in our case of surfaces of revolution eq. (3.8), after some calculations steps (see again Appendix B) the Gaussian curvature of surfaces of revolution yields

$$K = \frac{-r''(s)}{r(s)}\,. \tag{5.3}$$

Note that K is expressed in terms of $1/a^2$ since all variables, including the radius $r(s)$ and its derivatives, are rescaled as shown in eq. (3.27).

Let us first investigate the structure of the analytical solution of the zeroth level for any Gaussian curvature, and hence, for any bijective radial profile $r(s)$. Afterwards, we establish the existence condition for zero-energy states. The differential equation for the zeroth level arises from eq. (3.34) and reads

$$\begin{pmatrix} 0 & \hat{L}^+ \\ \hat{L}^- & 0 \end{pmatrix} \begin{pmatrix} \psi_\uparrow(s) \\ \psi_\downarrow(s) \end{pmatrix} = 0\,. \tag{5.4}$$

If we denote the up and down components of the ground state in this chapter as

$$\psi^-(s) \equiv \psi_\downarrow(s) \tag{5.5}$$
$$\psi^+(s) \equiv \psi_\uparrow(s)\,, \tag{5.6}$$

we then have the equation

$$i(-\partial_s \pm V(s))\psi^\mp(s) = 0\,. \tag{5.7}$$

With this, the zero-energy solution of each components is either trivial $\psi^\pm(s) = 0$ or it reads

$$\psi^\pm(s) = \mathcal{N}_0 \exp\left\{ \mp \int_{s_{\text{ref}}}^{s} V(s')ds' \right\}, \tag{5.8}$$

where s_{ref} is some constant between $s_0 < s_{\text{ref}} < s_1$ which is irrelevant since the antiderivative of $V(s)$ evaluated at s_{ref} goes into the normalization constant $\mathcal{N}_0$ of the ground state spinor. As already mentioned, this problem was addressed in [25] from the point of view of supersymmetric quantum mechanics. As one can easily check, neither ψ^+ nor ψ^- is bounded in eq. (5.8) if

$$\lim_{s\to s_0} V(s) = \lim_{s\to s_1} V(s) = \pm\infty\,. \tag{5.9}$$

On the other hand, if

$$\lim_{s\to s_0} V(s) = \pm\infty \tag{5.10}$$
$$\lim_{s\to s_1} V(s) = \mp\infty\,, \tag{5.11}$$

then $\psi^\mp$ is bounded, while the other component $\psi^\pm$ is not, hence we choose it to be trivial $\psi^\pm = 0$. In other words, if the zero energy state exists, it is spin polarized.

Moving on, we now need to examine under what necessary condition our potential

$$V(s) = \frac{\alpha_m}{r(s)} + \beta r(s)$$

satisfies eq. (5.10). For $V(s)$ to have a divergence of different signs at both ends, s_0 and s_1, implies the existence of an odd number of zero crossings s_* located between the two ends

$$s_0 < s_* < s_1 \,. \tag{5.12}$$

These zero crossings are found by

$$V(s_*) \stackrel{!}{=} 0 \,, \tag{5.13}$$

which can be easily solved to obtain

$$-\frac{\alpha_m}{\beta} = r^2(s_*) \,, \tag{5.14}$$

which, if it has a solution, it is unique due to the bijectivity of $r(s)$ required in eq. (3.10). Since s_* describes the localization of the unique zero crossing, it is at the same time also the minimum of $|V(s)|$ and hence the position around which the zero state is located. Therefore, the value of the zero crossing s_* must be not only between both ends, but also far away from them, i.e.

$$s_0 \ll s_* \ll s_1 \tag{5.15}$$

to ensure the confinement of the state on the surface and, consequently, the divergence of $V(s)$, which is given if the state does not "feel" the borders. From this inequality we can again, due to the bijectivity of $r(s)$, transform this condition into the radius space and obtain the necessary condition for the zero state to exist

$$r_{\min}^2 \ll -\frac{\alpha_m}{\beta} \ll r_{\max}^2 \,, \tag{5.16}$$

which directly implies

$$\operatorname{sgn}(\alpha_m) \neq \operatorname{sgn}(B) \,. \tag{5.17}$$

The quantitative meaning of "far away from the borders" described above depends on how confined or localized the state is, i.e., how steep the potential wedge $|V(s)|$ is around s_*. This property is directly influenced by the values of α_m and β, but also by the radial profile $r(s)$, and therefore has to be checked separately for each particular case.

If we now want to play the same game and derive a general existence condition for excited states, we can apply the same rationale. For excited states where $\operatorname{sgn}(B) \neq \operatorname{sgn}(\alpha_m)$, we get exactly the same condition as in eq. (5.16). For the case where the potential does not have a zero crossing, i.e. $\operatorname{sgn}(B) = \operatorname{sgn}(\alpha_m)$, we obtain the minimum of $|V(s)|$ by calculating

$$\partial_s V(s_*) \stackrel{!}{=} 0 \,, \tag{5.18}$$

which gives us the condition

$$r_{\min}^2 \ll \frac{\alpha_m}{\beta} \ll r_{\max}^2 \,. \tag{5.19}$$

So, altogether, for all excited states, the condition

$$r_{\min}^2 \ll \left| \frac{\alpha_m}{\beta} \right| \ll r_{\max}^2 \tag{5.20}$$

must hold.

Since we now also know when excited states $\epsilon \neq 0$ occur, we shall present the procedure by which we intend to solve for their explicit analytical form. To do this, we need to simplify the analysis of eq. (3.34) further, since coupled differential equations are unpleasant to deal with. This is done by decoupling the equations, which results in

$$\hat{L}^- \hat{L}^+ \psi_\downarrow(s) = \epsilon^2 \psi_\downarrow \tag{5.21}$$

and for the other component

$$\hat{L}^+ \hat{L}^- \psi_\uparrow(s) = \epsilon^2 \psi_\uparrow \,. \tag{5.22}$$

The calculated spectrum is identical for both equations due to the super-symmetric structure of the underlying equation (see [25]). For instance, if we write out the differential equation eq. (5.21) of the down component, we obtain

$$\left[-\partial_s^2 + \frac{\partial V}{\partial s}(s) + V(s)^2 \right] \psi_\downarrow(s) = \epsilon^2 \psi_\downarrow(s) \,. \tag{5.23}$$

And whenever we find a solution for the down-component, the up-component is easily calculated by

$$\psi_\uparrow(s) = \frac{\hat{L}^+ \psi_\downarrow(s)}{\epsilon} \,. \tag{5.24}$$

If we want to start from the up component, the only difference is that in eq. (5.23) we have a minus in front of the potential derivative.

5.1.1 Cone $K = 0$

We shall start by giving explicit bound state solution for the simplest surface of revolution - surfaces with vanishing Gaussian curvature $K = 0$. By eq. (5.3) we conclude

$$r''(s) = 0 \to r(s) = C_1 s + C_2 \tag{5.25}$$

and from the equation eq. (3.11) we find

$$z(s) = s\sqrt{1 - C_1^2} + C_3 \,. \tag{5.26}$$

For simplicity, we set $z(0) = 0$ and $r(0) = 0$, therefore $C_2 = C_3 = 0$. Moreover, the variable C_1 is linked to the opening angel θ, which can be seen in Figure 5.1. The relation is calculated by

$$\sin(\theta/2) = \frac{r(s)}{s} = C_1 \,. \tag{5.27}$$

With this, we have

$$r(s) = s \sin(\theta/2) \,, \tag{5.28}$$

where $\theta \in (0, \pi]$. For the arc length we choose

$$s_0 = \frac{r_{\min}}{\sin(\theta/2)} \text{ and } s_1 = \frac{r_{\max}}{\sin(\theta/2)} \tag{5.29}$$

for some non-zero minimal and maximal radius $r_{\min} > 0$ and $r_{\max} > 0$.

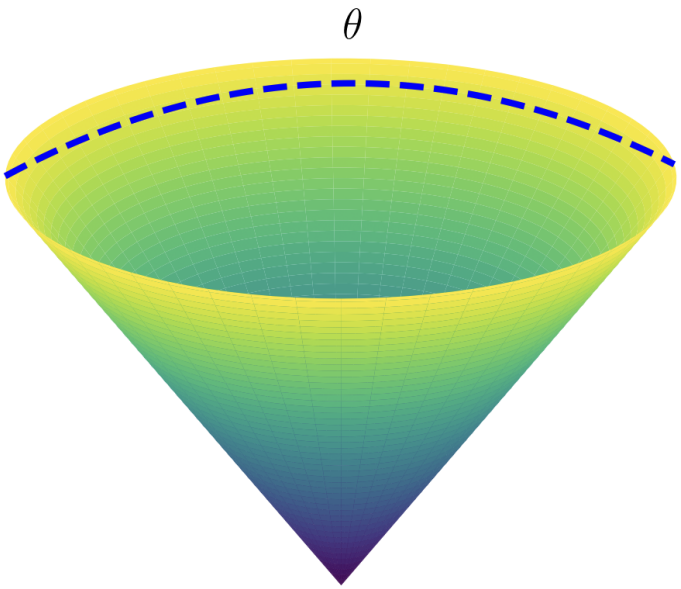

Figure 5.1: Sketch of a cone, eq. (5.26), with opening angle θ

Moving on, we explicitly calculate the wave function of the ground state. To do so, we explicitly specify the potential eq. (3.36) by rewriting it as

$$V(s) = \frac{\alpha_m^\theta}{s} + \beta_\theta s \,, \tag{5.30}$$

where we defined the quantities in the same manner as at the beginning (eq. (3.37))

$$\beta_\theta = \sin(\theta/2)\beta \quad \text{and} \quad \alpha_m^\theta = \frac{\alpha_m}{\sin(\theta/2)} \,. \tag{5.31}$$

This definition will be useful, since these variables will show up as exponents. As mentioned above, the ground state only exists if the magnetic field B and the angular number α_m have different signs. And from eq. (5.8) we get the ground state in the case $B > 0$ and $\alpha_m < 0$

$$\psi_0(s) = \mathcal{N}_0\, p_0(s) \begin{pmatrix} 1 \\ 0 \end{pmatrix} , \tag{5.32}$$

with

$$p_0(s) = s^{|\alpha_m^\theta|} \exp\Big\{ -|\beta_\theta| s^2/2 \Big\} , \tag{5.33}$$

while in the other case $B < 0$ and $\alpha_m > 0$ we obtain

$$\psi_0(s) = \mathcal{N}_0\, p_0(s) \begin{pmatrix} 0 \\ 1 \end{pmatrix} . \tag{5.34}$$

In addition, the existence condition from eq. (5.16) must be fulfilled for the state to be confined to the surface. In this context it reads

$$s_0^2 \ll \left| \frac{\alpha_m^\theta}{\beta_\theta} \right| \ll s_1^2 , \tag{5.35}$$

where, by taking the absolute values around it, it also includes the condition for the excited states eq. (5.20). The ground state, with the above analytical form and also computed numerically, is depicted in Figure 5.2, where we see a perfect match. Now that we know the expression for the ground state, we can proceed to analyze the excited states. Let us now go ahead and solve for the explicit form of the excited states. Using the explicit radial profile eq. (5.28), we are ready to write down the differential equation eq. (5.23), where we order the terms by powers in s, namely

$$\left(-\partial_s^2 + A_1 - \epsilon^2 + \frac{A_2}{s^2} + A_3 s^2 \right) \psi_\downarrow(s) = 0 , \tag{5.36}$$

where we have the factors

$$A_1 = \beta_\theta + 2\beta_\theta \alpha_m^\theta \tag{5.37}$$

$$A_2 = \alpha_m^\theta (\alpha_m^\theta - 1) \tag{5.38}$$

$$A_3 = \beta_\theta^2 . \tag{5.39}$$

The exact calculation of the constant factors A_1, A_2 and A_3 can be found in Appendix D. The most important properties to keep in mind are $A_3 > 0$ and $A_2 > -1/4$. It turns out that a further practical Ansatz leads us to an analytical solution

$$\psi_\downarrow(s) = \frac{\mathcal{N}}{\sqrt{s}} p\Big(|\beta_\theta| s^2 \Big) , \tag{5.40}$$

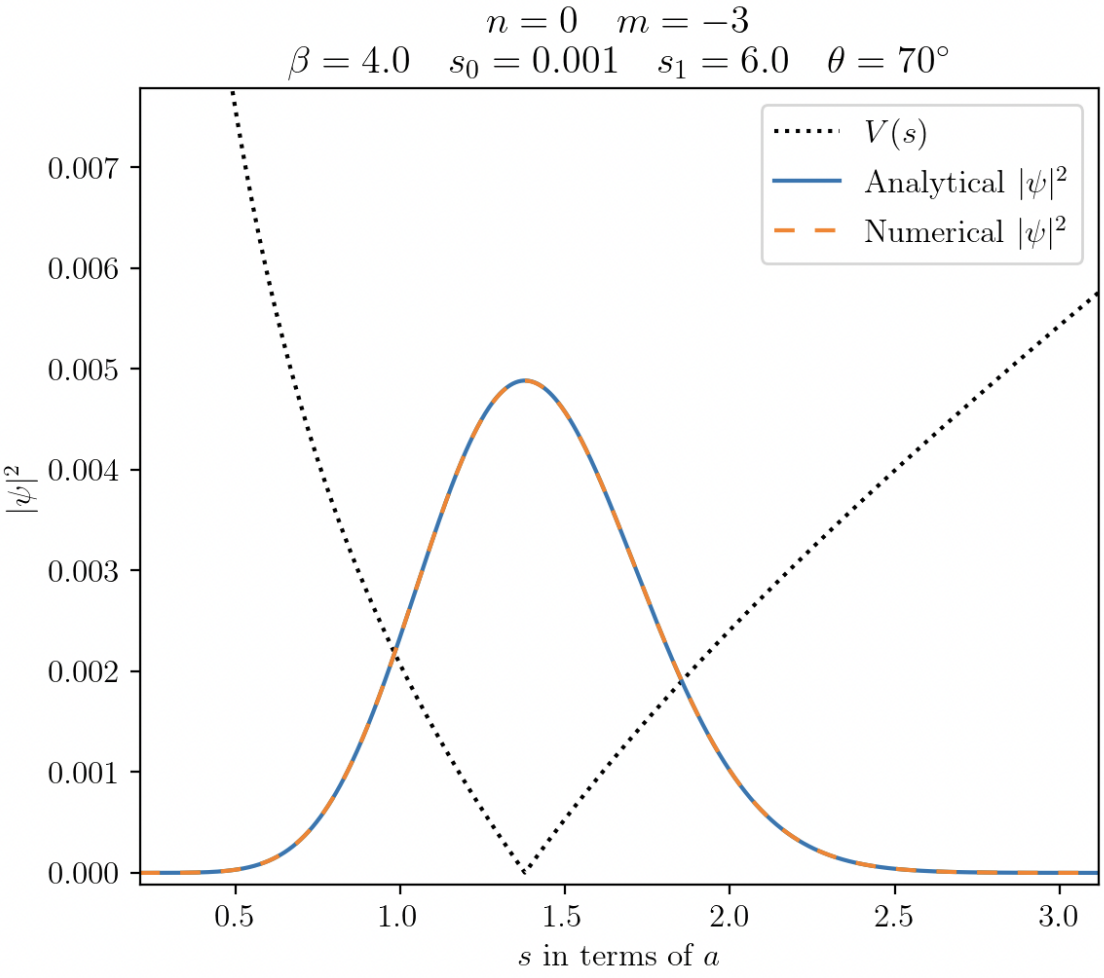

Figure 5.2: Ground state, eq. (5.32), on the cone

The dotted line represents the effective mass potential $|V(s)|$. For the numerics we used $L = 1200$ lattice points in the arc length direction.

with some new function $p(z)$ and normalization constant $\mathcal{N}$. After some calculation steps in Appendix D, we arrive at the two linear independent solutions, which turn out to be the Whittaker functions

$$p\Big(|\beta_\theta|s^2\Big) = M_{\kappa,\mu}\Big(|\beta_\theta|s^2\Big) \quad \text{and} \quad W_{\kappa,\mu}\Big(|\beta_\theta|s^2\Big)\,, \tag{5.41}$$

with

$$\begin{aligned} \kappa &= \frac{-A_1+\epsilon^2}{4A_3} \\ \mu &= \frac{1}{2}\sqrt{A_2+1/4} = \frac{1}{2}|\alpha_m^\theta - 1/2| > 0\,. \end{aligned} \tag{5.42}$$

These Whittaker functions can be further expressed in terms of Kummer's confluent hyper-geometric functions $M(a,b,z)$ and $U(a,b,z)$, with the variables $a,b,z \in \mathbb{R}$, by the formula

$$M_{\kappa;\mu}(z) = \exp(-z/2)\, z^{\mu+\frac{1}{2}} M\left(\mu-\kappa+\tfrac{1}{2}, 1+2\mu, z\right) \tag{5.43}$$

$$W_{\kappa;\mu}(z) = \exp(-z/2)\, z^{\mu+\frac{1}{2}} U\left(\mu-\kappa+\tfrac{1}{2}, 1+2\mu, z\right)\,. \tag{5.44}$$

Since we want the solutions to be bound states, we demand

$$\begin{aligned} \lim_{s\to 0}\psi_\downarrow(s) &\to 0 \\ \lim_{s\to\infty}\psi_\downarrow(s) &\to 0\,. \end{aligned} \tag{5.45}$$

At this point the observant reader may object that at the beginning we specified the arc length to range from some finite non zero $s_0 > 0$ to $s_1 < \infty$. And with that we cannot serve any of the limites form above. The solution to this problem is given by the same argument from the section before (see Chapter 5.1). While strictly mathematically the concerns are true, as long as the potential minimum s_* is far away from the borders of the surface s_0 and s_1, the particle is localized enough and therefore it does not know anything about the borders, and we are allowed to demand both limites.

It turns out that the first limit in eq. (5.45) is fulfilled by default. This is because we have $\mu > 0$ and by that we have no poles at $s = 0$ in the term $z^{\mu+1/2}$ in eq. (5.43) and since by definition $M(a,b,0) = 1$ we automatically have

$$\psi_\downarrow(0) = M_{\kappa;\mu}(0) = 0\,. \tag{5.46}$$

Therefore, the only relevant case we have to worry about is $s \to \infty$. Here the only way to achieve a vanishing solution at infinity is by requiring the Kummer's functions $M(a,b,z)$ and $U(a,b,z)$ to decay into a polynomial, which is the case if

the first argument is a non-positive number $-n$ where $n \in \mathbb{N}$, which in our case amounts to

$$\mu - \kappa + 1/2 \stackrel{!}{=} -n\,. \tag{5.47}$$

In this case, they reduce to the generalized Laguerre polynomials and become linearly dependent

$$U(-n, 1+2\mu, z) \propto M(-n, 1+2\mu, z) \propto L_n^{2\mu}(z)\,. \tag{5.48}$$

By rearranging eq. (5.47), we arrive at the spectrum ϵ_n and notice that it splits into two categories, namely, for $\mathrm{sgn}(B) \neq \mathrm{sgn}(\alpha_m)$ we obtain

$$\epsilon_n = \pm\sqrt{4|\beta_\theta|n} \underset{B\to\infty}{\propto} B^{\frac{1}{2}}\,, \tag{5.49}$$

while for $\mathrm{sgn}(B) = \mathrm{sgn}(\alpha_m)$ we have

$$\epsilon_{nm} = \pm\sqrt{4|\beta_\theta|\Big(\frac{1}{2} + n + |\alpha_m^\theta|\Big)} \underset{B\to\infty}{\propto} B^{\frac{1}{2}}\,. \tag{5.50}$$

In both cases, we get a square root dependence of the energies on the magnetic field B for big fields $B \to \infty$. These energies are depicted in their analytical form and also numerically in Figure 5.3 for some fixed β and a range of α_m. We obtain a perfect match. To see the asymptotic behavior of the energies $\epsilon_{nm}(B)$ better, we pick a certain angular quantum number m and calculate the energy numerically on the truncated surface as well as analytically for a few values of n for varying magnetic flux β in some allowed range. This plot can be seen in Figure 5.4. We see a perfect agreement for high fluxes. At low magnetic fluxes β, the numerical solutions deviate significantly from the analytical calculations. In this regime, we have a weak particle confinement and hence the electron feels the boundaries of the truncated surface, which was used in the numerical calculations. Therefore, at low β the observed numerical solutions describe edge states.

As we can see in the analytical expression eq. (5.50), the conical geometry with $\theta < \pi$ leads to the breaking of the m-degeneracy of the standard Dirac-Landau levels from eq. (5.49). To the best of our knowledge, these novel energy levels for massless Dirac electrons on the cone have not been calculated before. A similar problem, yet only for Schrödinger electrons, has been addressed in [31], where a degeneracy breaking can also be observed.

Let us now take care of the wave functions and deliver the explicit form of the spinor $\psi(s)$. Before starting, a short remark is necessary. We have already seen that the energies fall into two branches, namely for same and opposite sign of α_m and B, and thus the absolute sign was not of importance, only the relative one. However, this is no longer the case for the wave functions. We have already seen in the

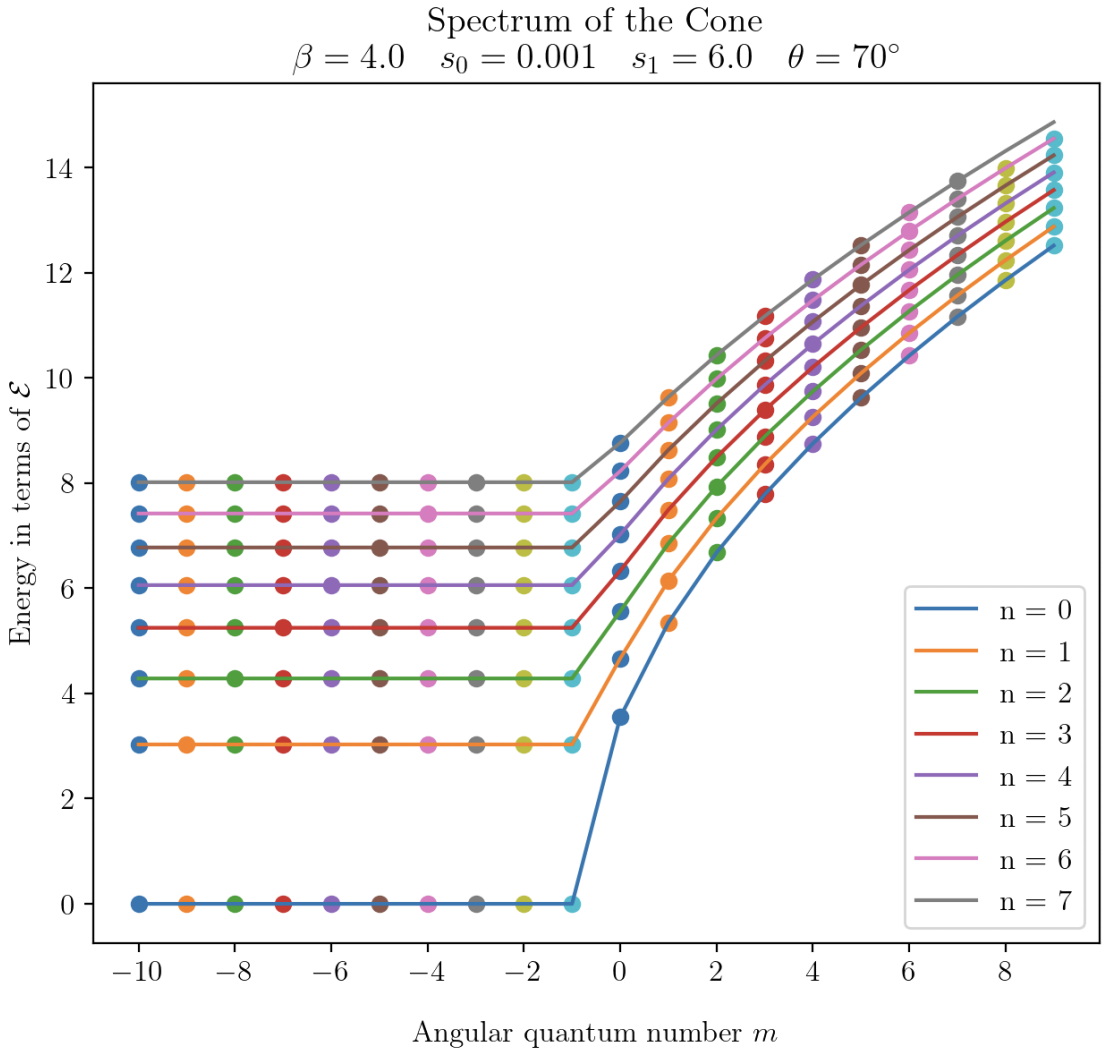

Figure 5.3: Spectrum of the cone

The continuous lines depict the analytical solutions eq. (5.49) and eq. (5.50) while the dots represent the numerical results. For the numerics we used $L = 1200$ lattice points in the arc length direction.

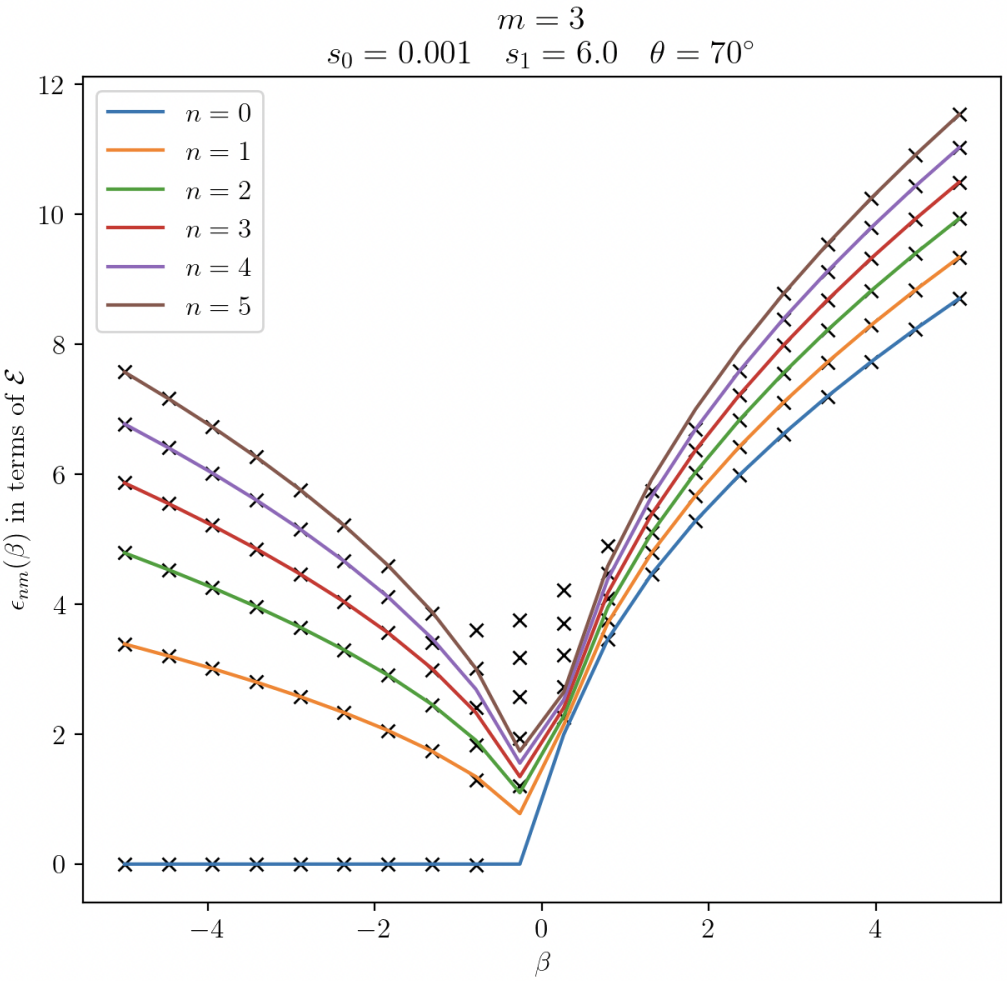

Figure 5.4: Flux dependence of the energy of the cone

The continuous lines depict the analytical solutions eq. (5.49) and eq. (5.50) while the crosses represent the numerical results. For the numerics we used $L = 1200$ lattice points in the arc length direction.

calculation of the zero energy levels (eq. (5.34), eq. (5.32)) that the absolute sign of B and α_m influences the form of the ground state wave function. The same behavior is to be expected in the calculation of the excited states. Therefore, we expect slightly different solutions for different absolute signs of B and α_m. Fortunately, we do not need to calculate all four cases, as we can make use of time reversal transformations $\mathcal{T}$ to translate solutions from B and α_m to $-B$ and α_{-m}, since time reversal transformations flip the sign of magnetic fields and angular momentum, and thus also the sign of the angular momentum quantum number. Therefore, we compute the wave functions only for two cases, namely for $B < 0$ and $\alpha_m > 0$ and for the case $B > 0$ and $\alpha_m > 0$ and then apply each time the time reversal operator, i.e.

$$\mathcal{T} = i\sigma_y \mathcal{K} \tag{5.51}$$

on the spinor $\psi(s)$ to obtain the other two cases. Here we denote the complex conjugate operator by $\mathcal{K}$. Let us start with $B < 0$ and $\alpha_m > 0$, then with all the information from above, eq. (5.40) becomes

$$\psi_\downarrow(s) = \mathcal{N} p_0(s) L_n^{|\alpha_m^\theta|-1/2}(|\beta_\theta| s^2)\,, \tag{5.52}$$

having the function $p_0(s)$ from eq. (5.33) contained in the ground state. Moving on, for the other component we obtain

$$\psi_\uparrow(s) = \frac{i(-\partial_s + V(s))}{\epsilon_n} \psi_\downarrow(s)\,, \tag{5.53}$$

which gives us the total spinor

$$\psi(s) = \mathcal{N} p_0(s) \begin{pmatrix} \frac{2i|\beta_\theta|}{|\epsilon_n|} s L_{n-1}^{|\alpha_m^\theta|+1/2}(|\beta_\theta| s^2) \\ L_n^{|\alpha_m^\theta|-1/2}(|\beta_\theta| s^2)\,. \end{pmatrix} \tag{5.54}$$

We observe that the up component has one polynomial order less than the down component, which is consistent with the structure of the ground state eq. (5.34). The interested reader may refer to Appendix D for the detailed calculations. The other case $B > 0$ and $\alpha_m > 0$ gives us a total spinor

$$\psi(s) = \mathcal{N} p_0(s) \begin{pmatrix} \frac{2i|\beta_\theta|}{|\epsilon_{nm}|} s L_n^{|\alpha_m^\theta|+1/2}(|\beta_\theta| s^2) \\ L_n^{|\alpha_m^\theta|-1/2}(|\beta_\theta| s^2) \end{pmatrix}\,, \tag{5.55}$$

where this time we obtain an order higher in the up component. The effect of $\mathcal{T}$ to get the other two cases, preserves the overall shape of the states only that the up component is swapped with the down component. The detailed calculation can also be found in Appendix D. In Figure 5.5, for a truncated cone at a given flux value

of β and α_m, the wave functions for the same and different sign cases from above are computed numerically and compared with the analytical expressions, yielding a perfect match. We note that in the case of the same sign, the number of nodes of the up and down components is the same, while in the case of different signs, it differs by one.

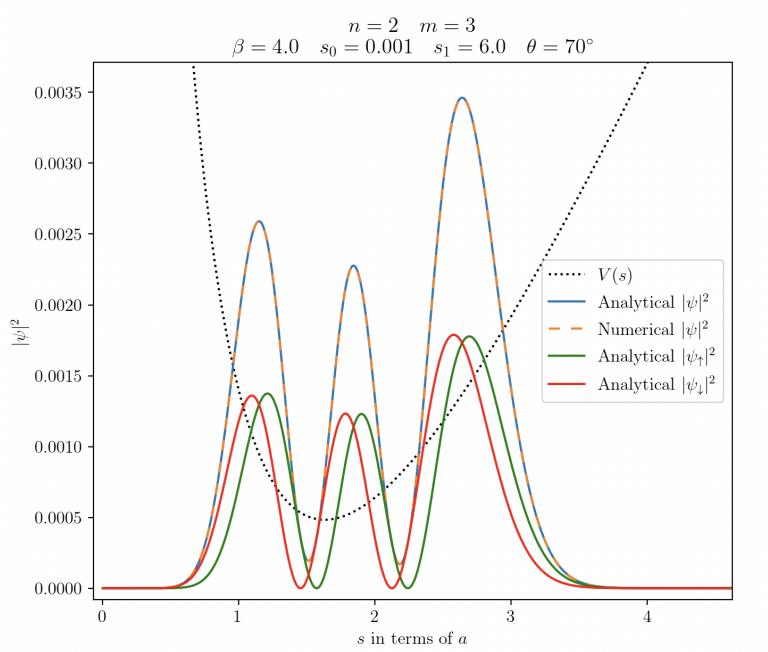

(a) $\mathrm{sgn}(B) = \mathrm{sgn}(\alpha_m)$

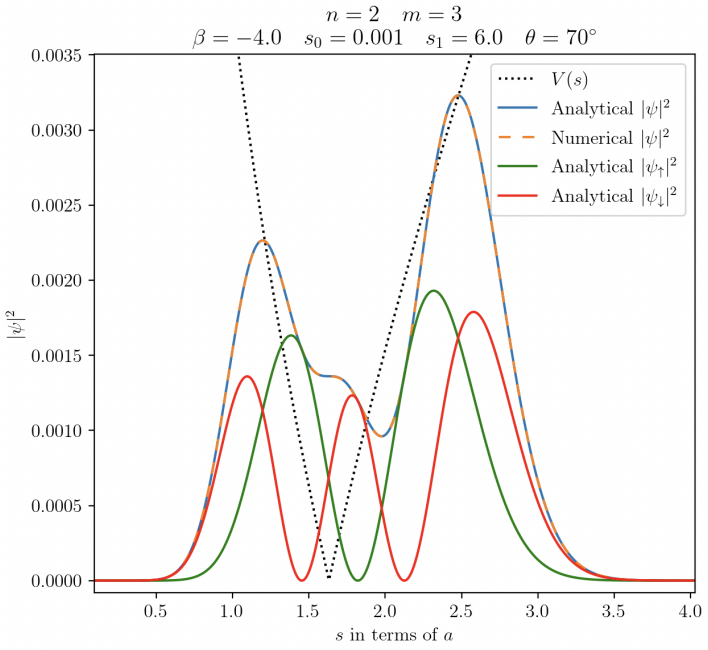

(b) $\mathrm{sgn}(B) \neq \mathrm{sgn}(\alpha_m)$

Figure 5.5: Excited states on the cone, eq. (5.54) and eq. (5.55)

Excited states on the cone with different sign configurations of B and α_m. The dotted line represents the effective mass potential $|V(s)|$. For the numerics, we used $L = 1200$ lattice points in arc length direction.

5.1.2 Pseudosphere $K = -1$

Let us now move on to a more interesting example of a curved surface, one with constant negative curvature $K = -1$. For this purpose, we simply solve the differential equation eq. (5.3), one linearly independent solution of which is

$$r(s) = \exp(-s)\,. \tag{5.56}$$

Since the arc length can be chosen as $s_0 \geq 0$ and $s_1 \leq \infty$, we notice that for the maximal and minimal radius we have

$$0 \leq r_{\min} < r < r_{\max} \leq 1\,. \tag{5.57}$$

This surface is known as the pseudosphere and can be viewed in Figure 5.6 for

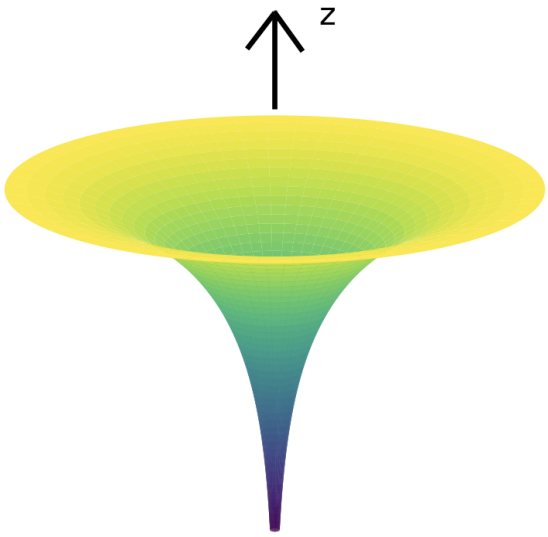

Figure 5.6: Sketch of a pseudosphere, eq. (5.58)

which we again used eq. (3.11) to calculate the r dependent z-coordinate, namely

$$z(r) = \int_r^1 \sqrt{\frac{1}{R^2} - 1}\,\mathrm{d}R\,. \tag{5.58}$$

As before, we first determine the wave function of the ground state. In the case of $B > 0$ and $\alpha_m < 0$, we obtain

$$\psi_0(s) = \mathcal{N}_0 p_0(s) \begin{pmatrix} 0 \\ 1 \end{pmatrix}\,, \tag{5.59}$$

with

$$p_0(s) = \exp\left\{ -\frac{|\alpha_m|}{r(s)} - |\beta| r(s) \right\}. \tag{5.60}$$

For the other case of $B < 0$ and $\alpha_m > 0$, we obtain

$$\psi_0(s) = \mathcal{N}_0 p_0(s) \begin{pmatrix} 1 \\ 0 \end{pmatrix}. \tag{5.61}$$

Note again the necessary condition eq. (5.20) such that the state is localized within the pseudosphere. We now turn our attention to the excited states. It turns out that if we change the variables from the arc length s to the radius r, we get the derivative

$$\partial_s = -r\partial_r \,, \tag{5.62}$$

which turns out to be the right coordinate for this problem to solve the eigenvalue problem, transforming eq. (5.22) to

$$\left[-r^2\partial_r^2 - r\partial_r - r\frac{\partial V}{\partial r}(r) + V(r)^2 \right] \psi_\downarrow(r) = \epsilon^2 \psi_\downarrow(r) \,. \tag{5.63}$$

To solve the case of the excited states, we get the inspiration from Chapter 5.1.1, where we see that the structure of the excited states eq. (5.54) and eq. (5.55) contains the functions of the ground states eq. (5.34) and eq. (5.32), which motivates the Ansatz

$$\psi_\downarrow(r) = p_0(r) H(r) \,. \tag{5.64}$$

This Ansatz leads us to the following differential equation

$$r^2 \frac{\mathrm{d}^2 H}{\mathrm{d}r^2}(r) + f(r) \frac{\mathrm{d}H}{\mathrm{d}r}(r) + q(r) H(r) = 0 \,, \tag{5.65}$$

with

$$f(r) = r + 2|\alpha_m| - 2|\beta| r^2 \tag{5.66}$$

$$q(r) = r(\beta - |\beta|) - r^{-1}(\alpha_m + |\alpha_m|) + \epsilon^2 - 2\beta\alpha_m - 2|\beta\alpha_m| \,. \tag{5.67}$$

For simplicity, we set $\alpha_m < 0$ to remove the r^{-1} factor in order to obtain Heun's double confluent equation. To find out the spectrum we use asymptotic methods presented in [32], for which we have to bring the equation into its canonical form used in the paper. For this purpose, we use the transformation

$$r \to 2|\beta| r \,, \tag{5.68}$$

which gives us the transformed functions

$$f(r) \to f(r) = r + 4|\alpha_m \beta| - r^2 \tag{5.69}$$

$$q(r) \to q(r) = \frac{r}{2}(\mathrm{sgn}(\beta) - 1) + \epsilon^2 - 2\Phi\alpha_m - 2|\beta\alpha_m| \tag{5.70}$$

$$q(r) \to q(r) = -r\Theta(-\beta) + \epsilon^2 - 4\beta\alpha_m\Theta(\beta\alpha_m)\,, \tag{5.71}$$

where $\Theta(x)$ is the Heavy-side function. This gives us the spectrum

$$\epsilon_{nm} = \tag{5.72}$$
$$\pm\sqrt{\sqrt{4|\alpha_m\beta|}(2n + \Theta(-\beta)) + \frac{1}{2}n(n + \Theta(-\beta)) - 1 - \Theta(-\beta) + 4\beta\alpha_m\Theta(\beta\alpha_m)}\,.$$

Thus, in the case of same sign $\mathrm{sgn}(\alpha_m) = \mathrm{sgn}(B)$ we obtain the energies and their asymptotic dependence on the magnetic field

$$\epsilon_{nm} = \tag{5.73}$$
$$\pm\sqrt{\sqrt{4|\alpha_m\beta|}(2n+1) + \frac{1}{2}n(n+1) - 2 + 4\beta\alpha_m} \underset{B\to\infty}{\propto} B^{\frac{1}{2}}\,,$$

while surprisingly in the other case of different sign $\mathrm{sgn}(\alpha_m) \neq \mathrm{sgn}(B)$ we have

$$\epsilon_{nm} = \pm\sqrt{\sqrt{4|\alpha_m\beta|}2n + \frac{1}{2}n^2 - 1} \underset{B\to\infty}{\propto} B^{\frac{1}{4}}\,. \tag{5.74}$$

This unique scaling of the magnetic field was first discovered by Maximilian Fürst. Subsequently, I extended the energy formula to encompass both scenarios. These findings, being novel and unexpected, have been published in the joint publication [22]. The analytical computation of the wave functions is rather tedious, the algorithm for this is also described in [32], and since the analytic formula does not give us much more insight, we only focus on the numerical solutions of the wave function on the truncated pseudosphere, which is shown in Figure 5.9 for a high flux β and some permitted α_m. The associated effective mass potentials $|V(s)|$ are also shown. Here we see, as in the previous section, that in the case of same sign the number of nodes of the up and down component are the same, while in the case of different sign they differ by one. In Figure 5.8 we also plot the numerical solutions of the bound state wave functions and energies for the same β and a wide range of permitted α_m on the truncated pseudosphere and compare them with the analytics. Again, we see a perfect match. To see the asymptotic behavior of the energies better, we pick a specific angular quantum number m and calculate the energy for a few values of n by varying the magnetic flux β in some allowed range both numerically on the truncated surface and analytically. This plot can be seen

in Figure 5.7. As in the previous section, we see a perfect match for high magnetic fluxes, while for small fluxes we obtain edge states.

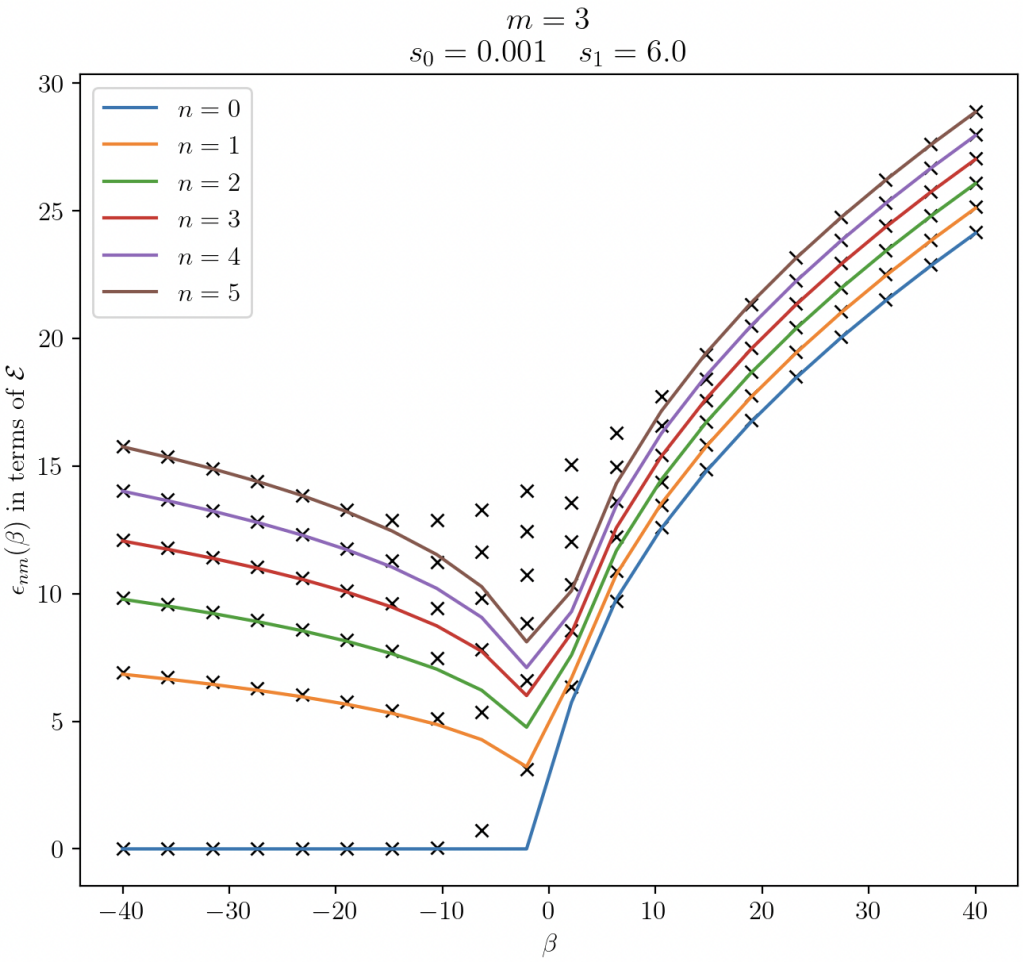

Figure 5.7: Flux dependence of the energy of the pseudosphere

The continuous lines depict the analytical solutions eq. (5.73) and eq. (5.74) while the crosses represent the numerical results. For the numerics we used $L = 1200$ lattice points in arc length direction.

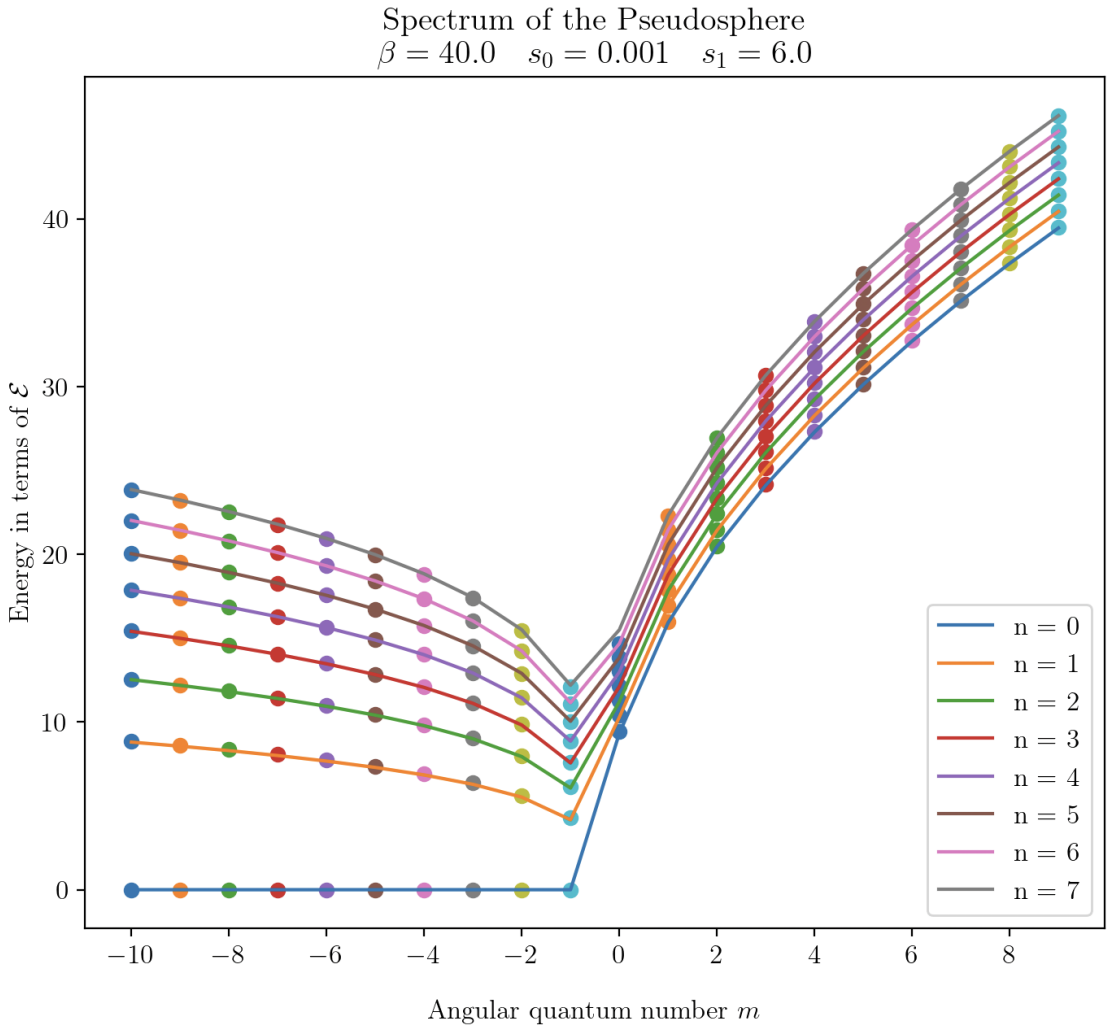

Figure 5.8: Spectrum of the pseudosphere

The continuous lines depict the analytical solutions eq. (5.73) and eq. (5.74) while the dots represent the numerical results. For the numerics we used $L = 1200$ lattice points in arc length direction.

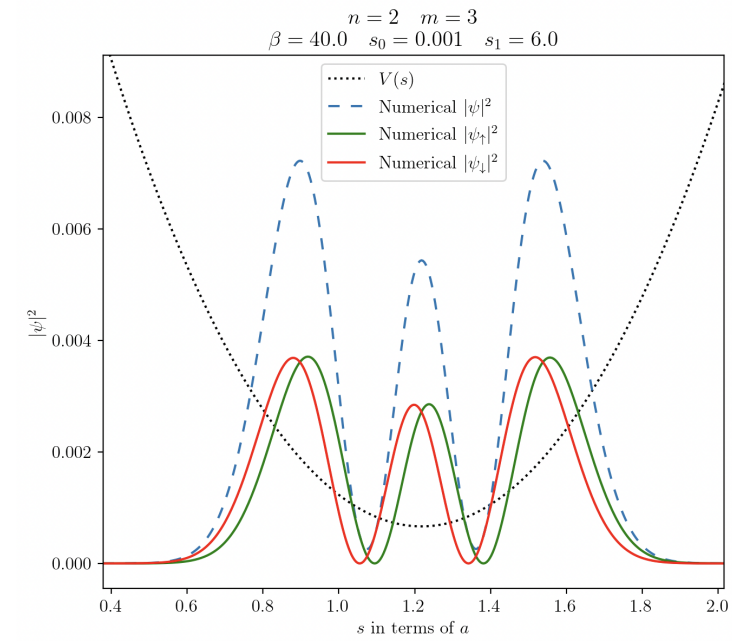

(a) $\mathrm{sgn}(B) = \mathrm{sgn}(\alpha_m)$

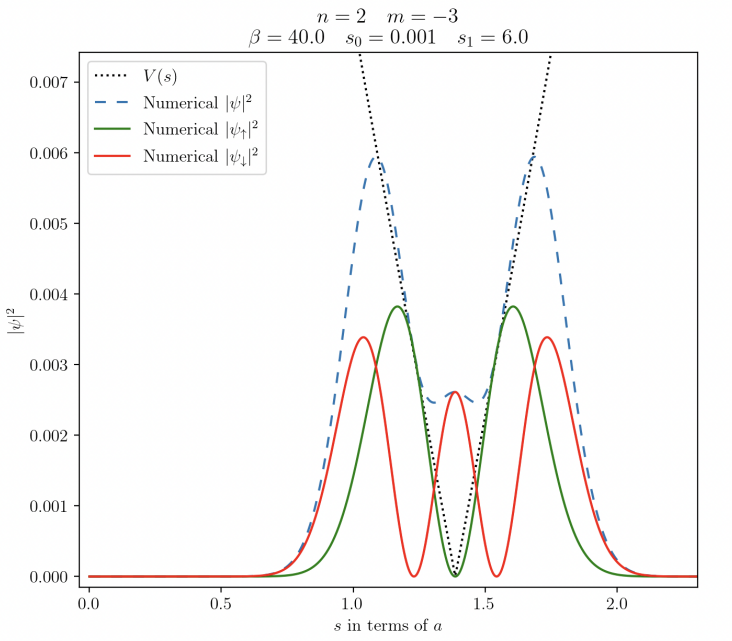

(b) $\mathrm{sgn}(B) \neq \mathrm{sgn}(\alpha_m)$

Figure 5.9: Excited states on the pseudosphere

Excited states on the pseudosphere with different sign configurations of B and α_m. The dotted line represents the effective mass potential $|V(s)|$. For the numerics, we used $L = 1200$ lattice points in arc length direction.

5.1.3 Hyperbolic Surface $K = 2 - 2r^2$

Now we come to another surface which turns out to be analytically solvable and complements the other two cases, since we are now dealing with a surface with positive Gaussian curvature $K > 0$. As it will become clear in a second, we have chosen the Gaussian curvature

$$K = 2 - 2r^2 \text{ with } 0 \leq r_{\min} < r < r_{\max} \leq 1\,, \tag{5.75}$$

which can be checked via eq. (5.3) to have the following radial profile

$$r(s) = \tanh(s)\,, \tag{5.76}$$

where the arc lengths can be chosen as $s_0 \geq 0$ and $s_1 \leq \infty$. Furthermore, we have the derivative

$$r' = 1 - r^2\,, \tag{5.77}$$

which we can use in combination with eq. (3.11) to obtain the r dependent z-coordinate

$$z(r) = \int_0^r \sqrt{\frac{1}{(1-R^2)^2} - 1}\,\mathrm{d}R\,. \tag{5.78}$$

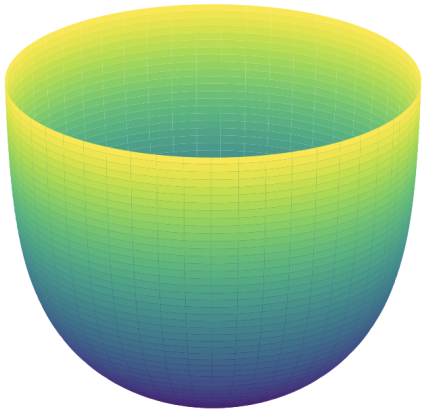

Figure 5.10: Sketch of the hyperbolic surface, eq. (5.78)

This surface can be seen in Figure 5.10. We call it from now on *hyperbolic surface*. We again start working in radius coordinates and specify the ground state for $\alpha_m > 0$ and $B < 0$, which yields

$$\psi_0(r) = \mathcal{N}_0 p_0(r) \begin{pmatrix} 0 \\ 1 \end{pmatrix}\,, \tag{5.79}$$

and for $\alpha_m < 0$ and $B > 0$ subsequently

$$\psi_0(r) = \mathcal{N}_0 p_0(r) \begin{pmatrix} 1 \\ 0 \end{pmatrix} , \tag{5.80}$$

with

$$p_0(r) = \cosh(s)^{-|\beta|+|\alpha_m|} \tanh(s)^{|\alpha_m|} = \left[1 - r^2\right]^{\frac{|\beta|-|\alpha_m|}{2}} r^{|\alpha_m|} . \tag{5.81}$$

By using the condition eq. (5.20), we have for $s_1 \gg 1$ ($r_{\max} \to 1$) the following rule

$$|\beta| - |\alpha_m| \gg 0 . \tag{5.82}$$

As in the section before, we first specify the equation that follows from eq. (5.23) when switching to radius coordinates

$$\left[-(1-r^2)^2 \partial_r^2 + 2r(1-r^2)\partial_r + (1-r^2)\frac{\partial V}{\partial r}(r) + V(r)^2 \right] \psi_\downarrow(r) = \epsilon^2 \psi_\downarrow(r) . \tag{5.83}$$

To make the analysis somehow easier, we set from the beginning $\alpha_m > 0$ and leave the freedom of sign in the flux β. Surprisingly, we no longer have the luck anymore to use the same trick as in the previous chapters. After some extensive trial and error, we find the right Ansatz to solve eq. (5.23), namely

$$\psi_\downarrow(r) = \rho_\epsilon(r) F(r) \tag{5.84}$$

$$\rho_\epsilon(r) = r^{\alpha_m}(1-r^2)^{k_\epsilon} \tag{5.85}$$

with

$$k_\epsilon = \frac{\sqrt{\left[\beta + \alpha_m\right]^2 - \epsilon^2}}{2} , \tag{5.86}$$

where we see that $\rho_\epsilon(r)$ is simply a generalization of $p_0(r)$, since in the case of $\mathrm{sgn}(B) \neq \mathrm{sgn}(\alpha_m)$ we have

$$\rho_0(r) = p_0(r) . \tag{5.87}$$

With this, we move on and insert $\rho_\epsilon(r)$ in eq. (5.83). After some lengthy but trivial calculation steps, we obtain the differential equation

$$(1-r^2)\frac{\mathrm{d}^2 F}{\mathrm{d}r^2}(r) + f(r)\frac{\mathrm{d}F}{\mathrm{d}r}(r) + qF(r) = 0 , \tag{5.88}$$

with

$$f(r) = \frac{2\alpha_m - r^2(4k_\epsilon + 2\alpha_m + 2)}{r} \tag{5.89}$$

$$q = -4\left[\alpha_m + \frac{1}{2}\right] k_\epsilon - 2\alpha_m^2 - (2\beta+1)\alpha_m + \epsilon^2 - \beta . \tag{5.90}$$

This differential equation already reassembles the hyper geometric differential equation

$$z(1-z)\frac{\mathrm{d}^2y}{\mathrm{d}z^2}(z) + [c-(a+b+1)z]\frac{\mathrm{d}y}{\mathrm{d}z}(z) - aby(z) = 0\,, \tag{5.91}$$

where its solution is the hyper geometric function $y(z) = {}_2F_1(a,b,c,z)$. Now, if we introduce the variable to be

$$z = r^2\,, \tag{5.92}$$

we obtain the equation

$$(1-r^2)\frac{\mathrm{d}^2y}{\mathrm{d}r^2}(r) + \left(\frac{2c-1-(2a+2b+1)r^2}{r}\right)\frac{\mathrm{d}y}{\mathrm{d}r}(r) - 4aby(r) = 0\,. \tag{5.93}$$

All that remains is to solve the equation

$$2a+2b+1 = 4k_\epsilon + 2\alpha_m + 2 \tag{5.94}$$

$$4ab = -q\,, \tag{5.95}$$

which links the variables of our differential equation to those of the hyper geometric equation and yields

$$a = \frac{2k_\epsilon + \alpha_m + 1/2 + |\beta - 1/2|}{2} \tag{5.96}$$

$$b = \frac{2k_\epsilon + \alpha_m + 1/2 - |\beta - 1/2|}{2} \tag{5.97}$$

$$c = \alpha_m + \frac{1}{2}\,. \tag{5.98}$$

Note the peculiarity in the absolute value $|\beta - 1/2|$, where it seems quite unnatural that the parameters change their values at a turning point $\beta = 1/2$ and not at zero. This is explained by the condition eq. (5.82), since $|\beta| > |\alpha_m| > 1/2$, therefore the constants will change their behavior at the magnetic flux $|\beta| > 1/2$. With this information, we finally can specify the desired solution $F(r)$ of eq. (5.88), which reads

$$F(r) = {}_2F_1(a,b,c,r^2)\,. \tag{5.99}$$

In order to have bound states we recall that one of the variables a or b have to be non-positive integers. Since we chose $\alpha_m > 0$, only b can become negative and hence

$$b \stackrel{!}{=} -n\,. \tag{5.100}$$

Therefore, we get in the case of $B > 0$ (hence in the case of same sign) the following energies

$$\epsilon_{nm} = \pm\sqrt{4\left[|\beta| - n - \frac{1}{2}\right]\left[n + |\alpha_m| + \frac{1}{2}\right]} \underset{B\to\infty}{\propto} B^{\frac{1}{2}}\,, \tag{5.101}$$

while in the case of $B < 0$ (hence in the case of different sign) we have

$$\epsilon_{nm} = \pm\sqrt{4n\left[|\beta| - |\alpha_m| - n\right]} \underset{B\to\infty}{\propto} B^{\frac{1}{2}} \,. \tag{5.102}$$

We introduced the absolute value of α_m although we started with positive $\alpha_m > 0$. By this, the formula is also applicable for the case $\alpha_m < 0$. One must shortly note that besides the condition eq. (5.82) the B-field must be large enough for the energies ϵ_{nm} to remain real.

Besides the interesting spectrum, we obtain an unconventional Ansatz function compared to those used in the previous chapters. It thus expands our repertoire of possible Ansatz functions in curved Dirac systems. We also learn that the energies scale in both cases with the square root of the B-field, just as in the case of the cone. The energies are plotted in Figure 5.11 for a specific high flux value β, both analytically and numerically on the truncated surface for various allowed quantum numbers α_m. We see a perfect agreement.

Let us now turn again our attention to the wave function. Summing up, we obtain for the down component in the case of $\alpha_m > 0$ and arbitrary B-field

$$\psi_\downarrow(r) \propto \rho_\epsilon(r) P_n^{m;2k_\epsilon}(1 - 2r^2) \,, \tag{5.103}$$

where we have used the relation between Jacobi-polynomials $P_n^{\kappa;\mu}(x)$ and the hypergeometric function ${}_2F_1(a, b, c, x)$, namely

$$P_n^{\kappa;\mu}(x) \propto {}_2F_1\left(n + \kappa + \mu + 1, -n; \kappa + 1; \frac{1-x}{2}\right) \,. \tag{5.104}$$

Due to the quantization of the energy, we obtain the relation

$$2k_\epsilon = -2n - m - 1 + |\beta - \frac{1}{2}| \,. \tag{5.105}$$

We omit the computation of the other component, since it can be done analytically by using various identities regarding the Jacobi-polynomials in the same manner as in the derivation of the states on the cone in eq. (5.54). It is left as an exercise for the reader. In Figure 5.12 the wave function is computed numerically on the truncated surface for the same flux β as used for the energies and for some permitted α_m. The associated effective mass potential $|V(s)|$ is also shown. Again, we see that in the case of same sign of B and α_m we get the same number of nodes in the up and down spin, while in the other case they differ by one. As before, we choose a certain angular quantum number m and calculate the energy for some values of n and vary the magnetic flux β in some allowed range numerically on the truncated surface as well as analytically. This plot can be seen in Figure 5.13.

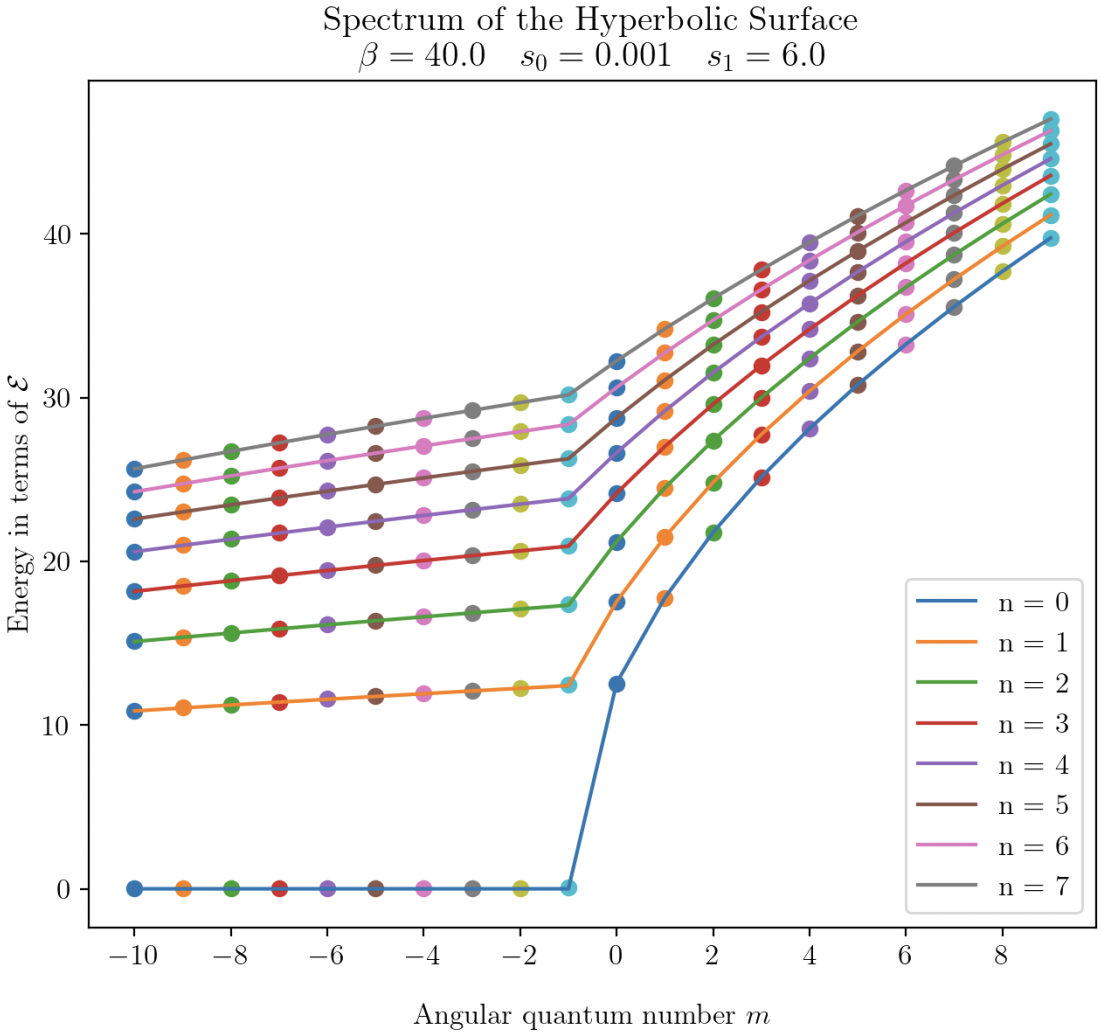

Figure 5.11: Spectrum of the hyperbolic surface

The continuous lines depict the analytical solutions eq. (5.101) and eq. (5.102) while the dots represent the numerical results. For the numerics we used $L = 1200$ lattice points in arc length direction.

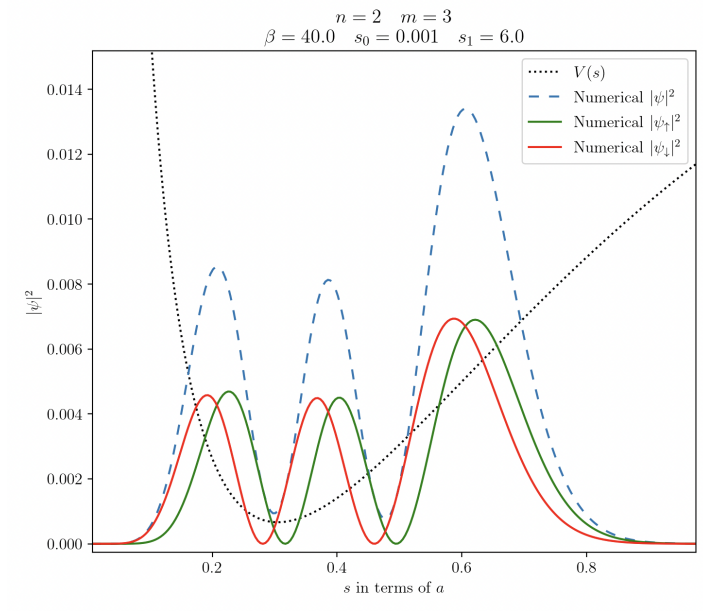

(a) $\mathrm{sgn}(B) = \mathrm{sgn}(\alpha_m)$

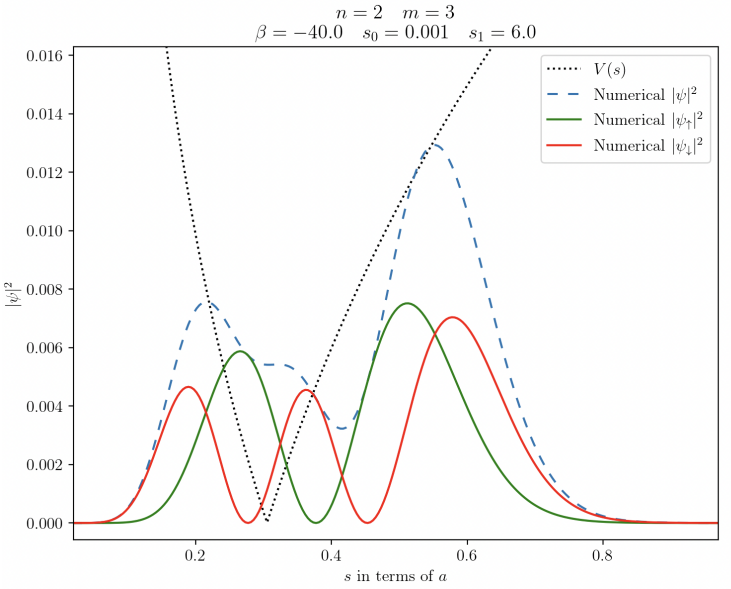

(b) $\mathrm{sgn}(B) \neq \mathrm{sgn}(\alpha_m)$

Figure 5.12: Excited states on the hyperbolic surface

Excited states on the hyperbolic surface with different sign configurations of B and α_m. The dotted line represents the effective mass potential $|V(s)|$. For the numerics, we used $L = 1200$ lattice points in arc length direction.

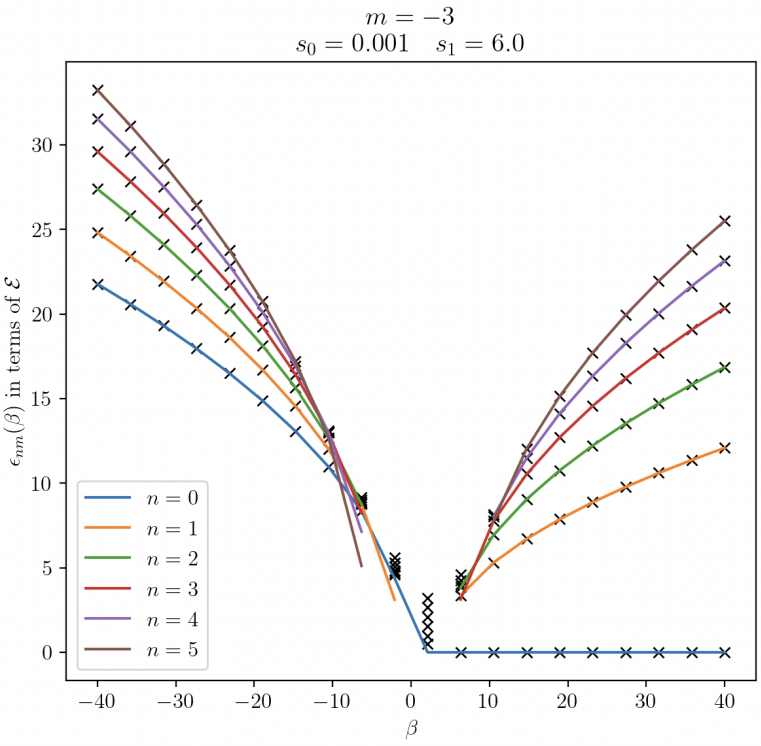

Figure 5.13: Flux dependence of the energy of the hyperbolic surface

The continuous lines depict the analytical solutions eq. (5.101) and eq. (5.102) while the crosses represent the numerical results. For the numerics we used $L = 1200$ lattice points in arc length direction.

5.2 Reciprocal Surfaces

So far, we have discussed and solved three distinct Gaussian curvature cases, whose specific geometries and magnetic field dependence where basically encoded in the effective mass potential $V(s)$ from eq. (3.36). We now want to move away from specific calculations and focus more on symmetry arguments to give us more insight into the energetic structure of general surfaces of revolution and their connection to each other. One specific link is established by the general structure of the potential $V(s)$, which is invariant under the change of the radius to the reciprocal radius, i.e.

$$r(s) \to \frac{1}{r(s)} \,. \tag{5.106}$$

By this, the underlying structure of the differential equation eq. (3.34) will also be invariant under this transformation[1]. Therefore, our aim now is to link solutions of a surface described by the radial profile $r(s)$, with the corresponding potential

$$V_r(s) = \frac{\alpha_m}{r(s)} + \beta r(s) \tag{5.107}$$

to solutions of a surface described by the reciprocal radius profile $1/r(s)$, with the corresponding potential

$$V_{\frac{1}{r}}(s) = \alpha_m r(s) + \frac{\beta}{r(s)} \tag{5.108}$$

and vice versa. From now, on we will call a surface described by the reciprocal radius $1/r$ simply *reciprocal surface*. An schematic representation of a surface and its corresponding reciprocal surface is showed in Figure 5.14. As a side note, for

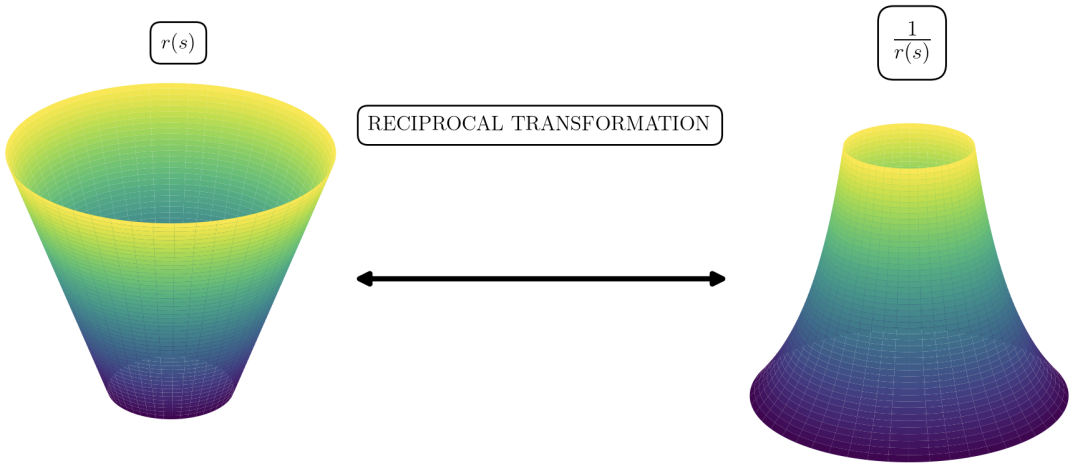

Figure 5.14: Sketch of a surface and its corresponding reciprocal surface

the boundary radii of the reciprocal surface we have

$$\left[\frac{1}{r}\right]_{\min} = \frac{1}{r_{\max}} \text{ and } \left[\frac{1}{r}\right]_{\max} = \frac{1}{r_{\min}}, \tag{5.109}$$

[1]It is to be noted that in general, the Schrödinger equation on a surface of revolution does not have this symmetry, i.e. when changing from the radius to the reciprocal radius the structure of the equation fundamentally changes. This can be simply seen by computing the Laplacian $\Delta = \frac{1}{\sqrt{\det g}} \frac{\partial}{\partial x^i} \left(\sqrt{\det g} g^{ij} \frac{\partial}{\partial x^j} \right)$ on a curved surface and by performing the transformation from radius to its reciprocal radius $r \to \frac{1}{r}$.

which plays a role in the bound state condition eq. (5.20). Moving on, let us suppose that we have a solution of the Hamiltonian eq. (3.31) for some quantum number m and dimensionless magnetic flux β for the surface r, where we denote the total wave function and energy by

$$\psi_r^{\alpha_m;\beta}(s,\varphi) = e^{i\alpha_m\varphi}\psi_r^{\alpha_m;\beta}(s) \text{ and } \epsilon_r(\alpha_m,\beta)\,. \tag{5.110}$$

Correspondingly, for the reciprocal surface $1/r$ we have

$$\psi_{\frac{1}{r}}^{\alpha_m;\beta}(s,\varphi) = e^{i\alpha_m\varphi}\psi_{\frac{1}{r}}^{\alpha_m;\beta}(s) \text{ and } \epsilon_{\frac{1}{r}}(\alpha_m,\beta)\,. \tag{5.111}$$

In both cases we mean by $\psi_r(s)$ or $\psi_{\frac{1}{r}}(s)$ the arc length wave function resulting from the separation Ansatz eq. (3.32). By looking at the potentials V_r and $V_{\frac{1}{r}}$ from above, which arise in the differential equation eq. (3.34) for $\psi(s)$, we realize that the arc length wave functions are related by

$$\psi_{\frac{1}{r}}^{\alpha_m;\beta}(s) = \psi_r^{\beta;\alpha_m}(s) \tag{5.112}$$

and therefore, one can relate the energies of both systems by

$$\epsilon_r(\alpha_m,\beta) = \epsilon_{\frac{1}{r}}(\beta,\alpha_m)\,. \tag{5.113}$$

After relating arc length wave functions and energies, as a next step we want to relate the entire wave functions $\psi(s,\varphi)$ of both systems by making use of the identity regarding the arc length wave functions eq. (5.112). By using this identity, we are now able to relate the electron densities of both systems by

$$|\psi_r^{\alpha_m;\beta}(s,\varphi)|^2 = |\psi_{\frac{1}{r}}^{\beta;\alpha_m}(s,\varphi)|^2 \text{ with } \beta \in \mathbb{Z} + \frac{1}{2}\,, \tag{5.114}$$

where we have to demand β to be half-integer due to the anti periodic boundary condition in the angular part of eq. (5.111) and the interchange of β and α_m used in the context of eq. (5.112). Hence, β plays the role of the angular momentum quantum number in the reciprocal system.

In summary, we conclude that we can always relate the energies of a $r(s)$ surface to its reciprocal surface $1/r(s)$ for arbitrary parameters β and α_m by eq. (5.113) as well as their arc length wave functions by eq. (5.112), while the full electron density $|\psi|^2$ of a reciprocal surface can only be constructed from the original surface in the case of half-integer flux β, as shown in eq. (5.114).

Before we can move on and look at specific examples of the duality described above, there is need for one more remark. This remark stems from the fact that we tacitly assumed that for any give surface $r(s)$ the reciprocal surface $1/r(s)$ exists in real space. This is not the case in general, which is manly due to the constrain

from eq. (3.12). Therefore, whenever we have a surface described by $r(s)$, we can find a reciprocal surface of revolution $1/r(s)$ whenever the surface radius satisfies the inequality

$$\left[\frac{r'(s)}{r^2(s)}\right]^2 \leq 1\,. \tag{5.115}$$

5.2.1 $K = 0$

Again, we shall start the investigation with the most simple and, at the same time, most interesting reciprocal surface, the reciprocal surface of the zero curvature case. We recall from Chapter 5.1.1 the formula for the radius of the case of zero curvature, and thus obtain for its reciprocal surface radius

$$r(s) = \frac{1}{s\sin(\theta/2)} \tag{5.116}$$

and therefore, due to the condition eq. (5.115), we can find a reciprocal surface only for

$$s \geq \frac{1}{\sqrt{\sin(\theta/2)}} \equiv s_0 \quad \text{and} \quad s_1 \leq \infty\,. \tag{5.117}$$

Consequently, for the minimal and maximal radii we calculate

$$0 \leq r_{\min} \leq r \leq r_{\max} = \frac{1}{\sqrt{\sin(\theta/2)}}\,. \tag{5.118}$$

We now specify the formula for the $z(r)$ coordinate of the reciprocal surface by again using eq. (3.11), which yields

$$z(r) = \int_r^{1/\sqrt{\sin(\theta/2)}} \sqrt{\frac{1}{R^4\sin^2(\theta/2)} - 1}\,\mathrm{d}R\,. \tag{5.119}$$

With this formula, we plot the radial function $z(r)$ of the reciprocal surface of the cone in Figure 5.15.

Let us now proceed as in the previous section and derive the arc length wave function and energy in terms of solutions of the $K = 0$ surface. Taking now into consideration eq. (5.112), we obtain for the total wave function of the reciprocal surface

$$\psi(s,\varphi) = e^{i\alpha_m\varphi}\psi^{\beta;\alpha_m}(s)\,, \tag{5.120}$$

where $\psi^{\beta;\alpha_m}(s)$ is the function from eq. (5.54) or eq. (5.55) in which β and α_m are swapped[1]. For the energies we obtain due to the formula eq. (5.113) and the already

[1]One shall not swap β_θ and α_m^θ inside eq. (5.54) and eq. (5.55), but rather β and α_m, which are to be found inside β_θ and α_m^θ.

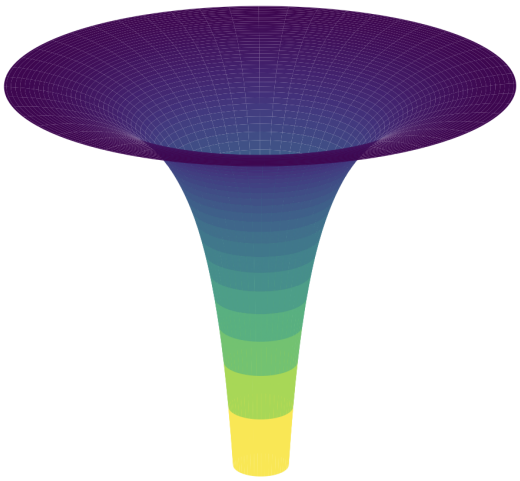

Figure 5.15: Sketch of the reciprocal cone, eq. (5.116)

calculated energies on the cone eq. (5.49) and eq. (5.50) the following two cases. For $\mathrm{sgn}(B) \neq \mathrm{sgn}(\alpha_m)$ the energies read

$$\epsilon_n = \pm\sqrt{4|\alpha_m \sin(\theta/2)|n} \propto B^0 = \text{const}\,, \tag{5.121}$$

while for $\mathrm{sgn}(B) = \mathrm{sgn}(\alpha_m)$ we get

$$\epsilon_{nm} = \pm\sqrt{4|\alpha_m \sin(\theta/2)|\left(\frac{1}{2} + n + \left|\frac{\beta}{\sin(\theta/2)}\right|\right)} \underset{B\to\infty}{\propto} B^{\frac{1}{2}}\,, \tag{5.122}$$

where we notice that one branch of the **energies** is **magnetic field independent**, which is something remarkable and to the best of our knowledge novel. We calculate the energies analytically and numerically on the truncated surface for some flux β and some permitted α_m and present them in Figure 5.17. Here we see a perfect agreement for $|m| > 1$, while in this plot, as expected by eq. (5.20), for the low m, the particle feels the low boundary $r_{\min}$ of the truncated surface, and hence the deviation between numerics and analytics emerges. The wave functions can be seen in Figure 5.16 for the same parameters as in the energy computation, calculated analytically by eq. (5.120) and numerically on the truncated surface. We see a perfect fit. The associated potentials $V(s)$ are also to be seen. As before, we pick a specific angular quantum number m and calculate the energy for a few values of n, and vary the magnetic flux β in some allowed range numerically on the truncated surface as well as analytically. This plot can be seen in Figure 5.18.

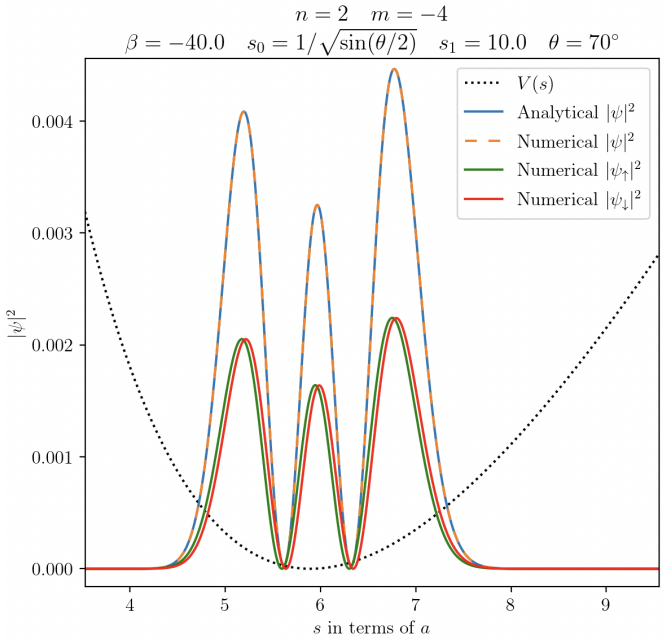

(a) $\mathrm{sgn}(B) = \mathrm{sgn}(\alpha_m)$

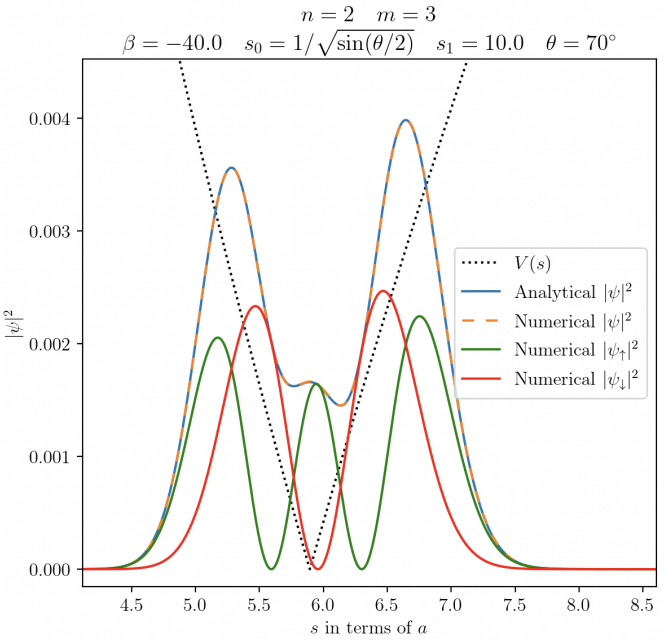

(b) $\mathrm{sgn}(B) \neq \mathrm{sgn}(\alpha_m)$

Figure 5.16: Excited states on the reciprocal cone surface

Excited states on the reciprocal cone surface with different sign configurations of B and α_m. The analytical expression is taken from eq. (5.120). The dotted black line represents the effective mass potential $|V(s)|$. For the numerics, we used $L = 1200$ lattice points in arc length direction.

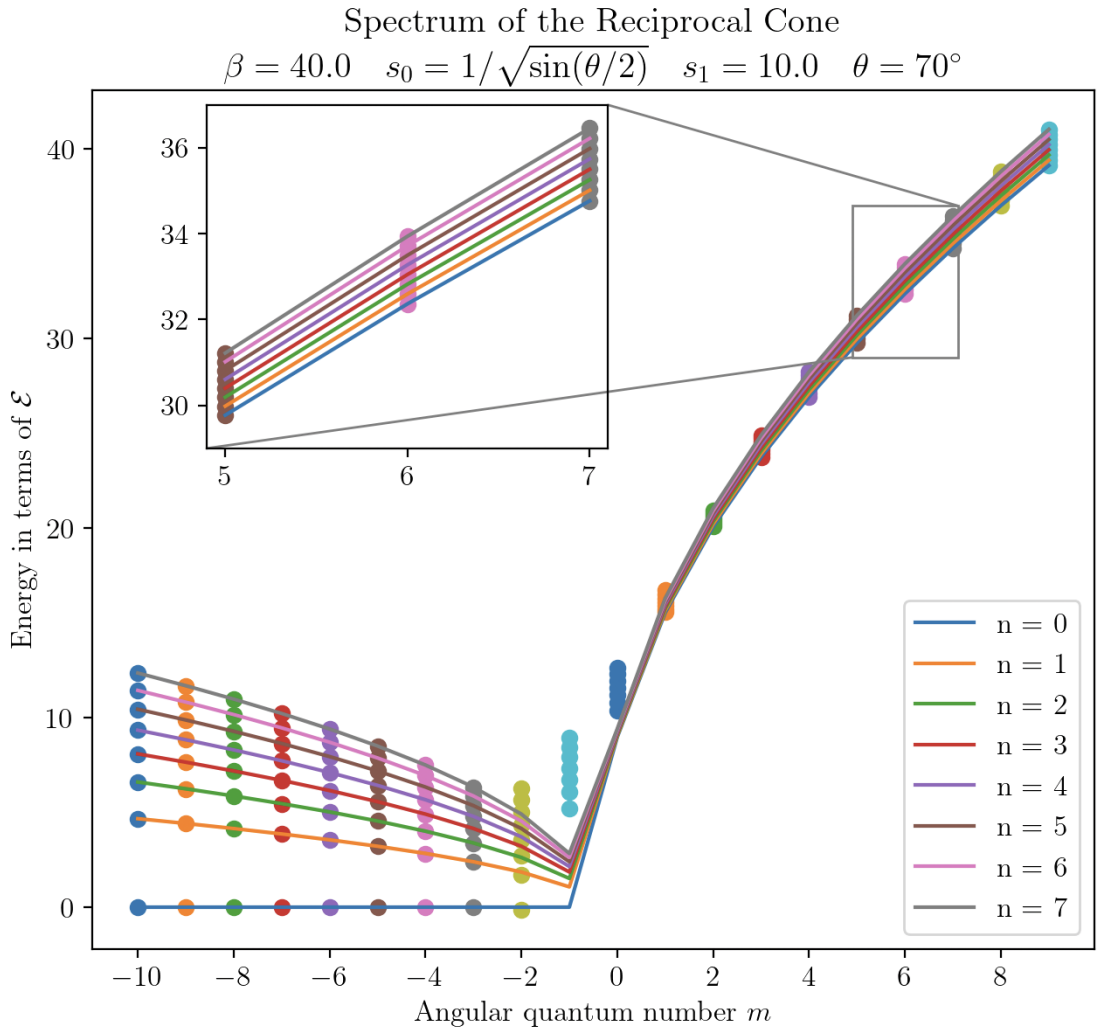

Figure 5.17: Spectrum of the reciprocal cone

The continuous lines depict the analytical solutions eq. (5.121) and eq. (5.122) while the dots represent the numerical results. For the numerics we used $L = 1200$ lattice points in arc length direction.

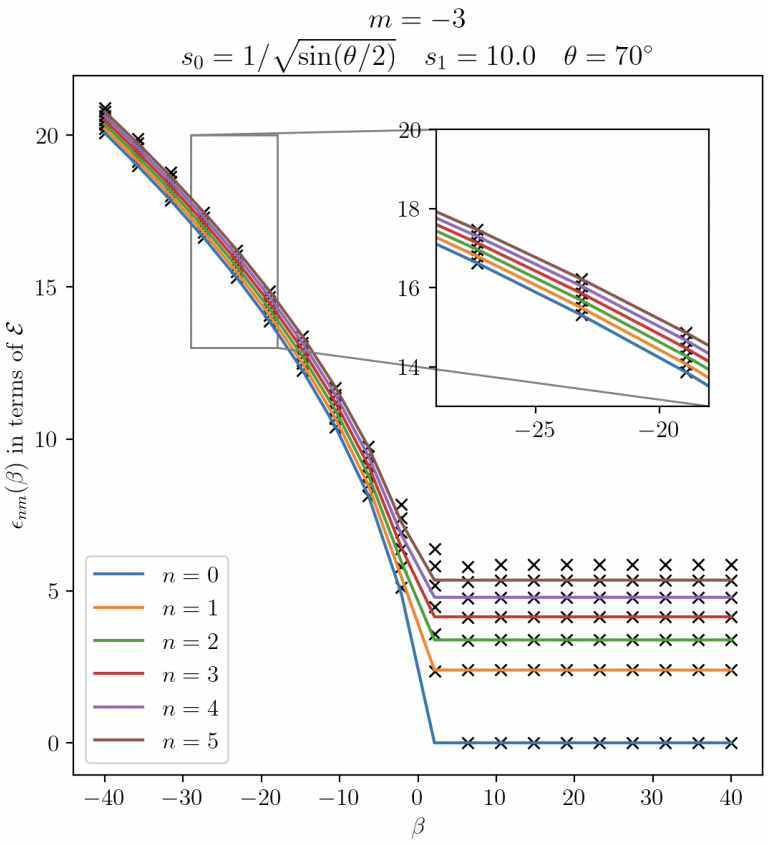

Figure 5.18: Flux dependence of the energy of the reciprocal cone

The continuous lines depict the analytical solutions eq. (5.121) and eq. (5.122) while the dots represent the numerical results. For the numerics we used $L = 1200$ lattice points in arc length direction.

5.2.2 $K = 2 - 2r^2$

We now move on and perform the same analysis as above in a concise manner, since the calculation steps are the same. Here the reciprocal radius reads

$$r(s) = \frac{1}{\tanh(s)}\,. \tag{5.123}$$

Due to condition eq. (5.115), we arrive at the constrain

$$s \geq \operatorname{arctanh}\left(\frac{1}{\sqrt{2}}\right) \equiv s_0\,, \tag{5.124}$$

while the other end can be chosen to be $s_1 \leq \infty$. Consequently, we obtain the boundary radii

$$1 = r_{\min} < r < r_{\max} = \sqrt{2}\,. \tag{5.125}$$

We now use again eq. (3.11) and arrive at the z-coordinate function

$$z(r) = \int_r^{\sqrt{2}} \sqrt{\frac{1}{(1-R^2)^2} - 1}\,\mathrm{d}R\,, \tag{5.126}$$

which gives us the surface in Figure 5.19.

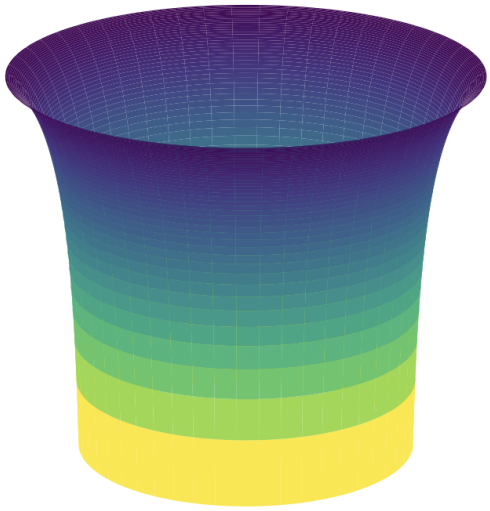

Figure 5.19: Sketch of the reciprocal hyperbolic surface, eq. (5.126)

Since the calculation of the wave function is straight forward, as in the section before, by using eq. (5.112) and the findings form Chapter 5.1.3, we only specify the energies by again just swapping α_m and β inside the energies in Chapter 5.1.3, yielding in the case of same sign $\mathrm{sgn}(B) = \mathrm{sgn}(\alpha_m)$

$$\epsilon_{nm} = \pm\sqrt{4\left[|\alpha_m| - n - \frac{1}{2}\right]\left[n + |\beta| + \frac{1}{2}\right]} \underset{B\to\infty}{\propto} B^{\frac{1}{2}}\,, \tag{5.127}$$

while in the case of different sign $\mathrm{sgn}(B) \neq \mathrm{sgn}(\alpha_m)$ we obtain

$$\epsilon_{nm} = \pm\sqrt{4n\left[|\alpha_m| - |\beta| - n\right]} \underset{B\to\infty}{\propto} B^{\frac{1}{2}}\,. \tag{5.128}$$

These energies are compute analytically and numerically and can be viewed in Figure 5.20. Again, for the angular quantum numbers m yielding confined states,

see eq. (5.20), we see a perfect matching. As before, we pick a specific angular quantum number m and calculate the energy for a few values of n, and vary the magnetic flux β in some allowed range numerically on the truncated surface as well as analytically. This plot can be seen in Figure 5.22. As in previous cases, for high magnetic fluxes β, we see a good agreement, while for low fluxes we obtain edge states and thus a discrepancy between numerics and analytics. For the wave functions, we see the same node structure as in the previous cases, see Figure 5.21.

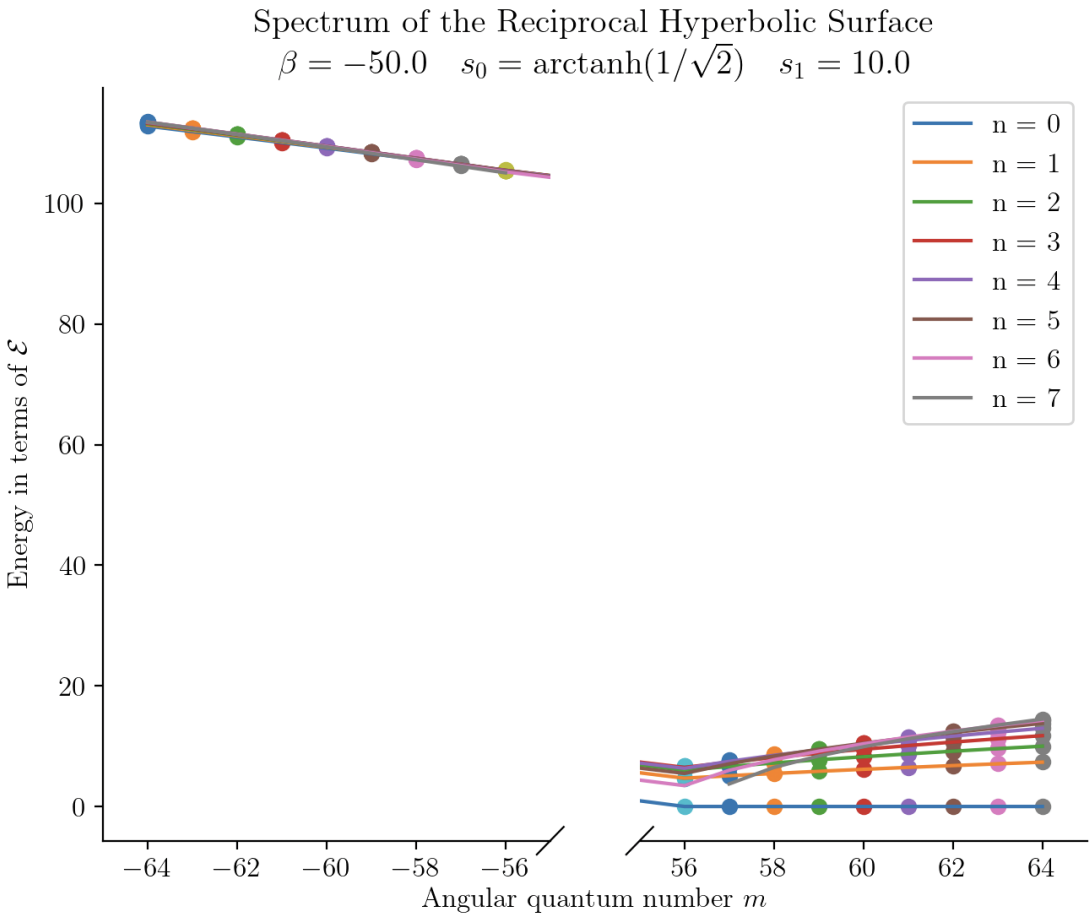

Figure 5.20: Spectrum of the reciprocal hyperbolic surface

The continuous lines depict the analytical solutions eq. (5.127) and eq. (5.128) while the dots represent the numerical results. For the numerics we used $L = 1200$ lattice points in arc length direction.

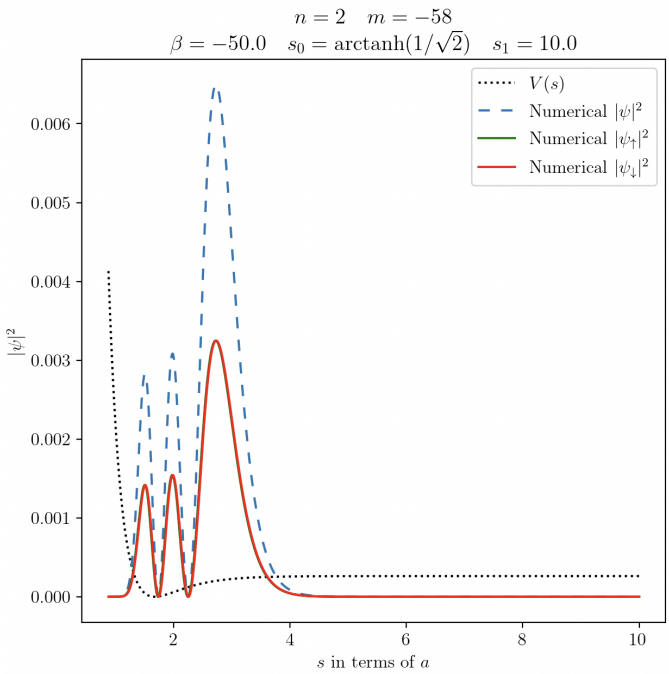

(a) $\operatorname{sgn}(B) = \operatorname{sgn}(\alpha_m)$

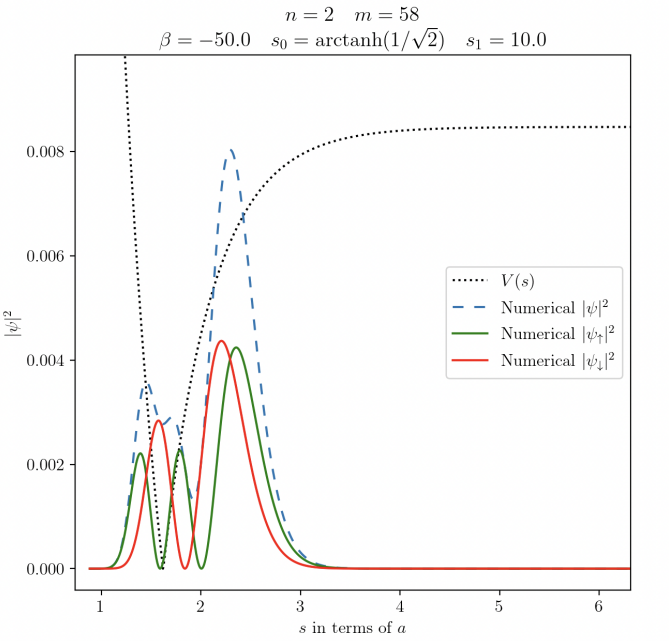

(b) $\operatorname{sgn}(B) \neq \operatorname{sgn}(\alpha_m)$

Figure 5.21: Excited states on the reciprocal hyperbolic surface

Excited states on the reciprocal hyperbolic surface with different sign configurations of B and α_m. The dotted black line represents the effective mass potential $|V(s)|$. For the numerics we used $L = 1200$ lattice points in arc length direction.

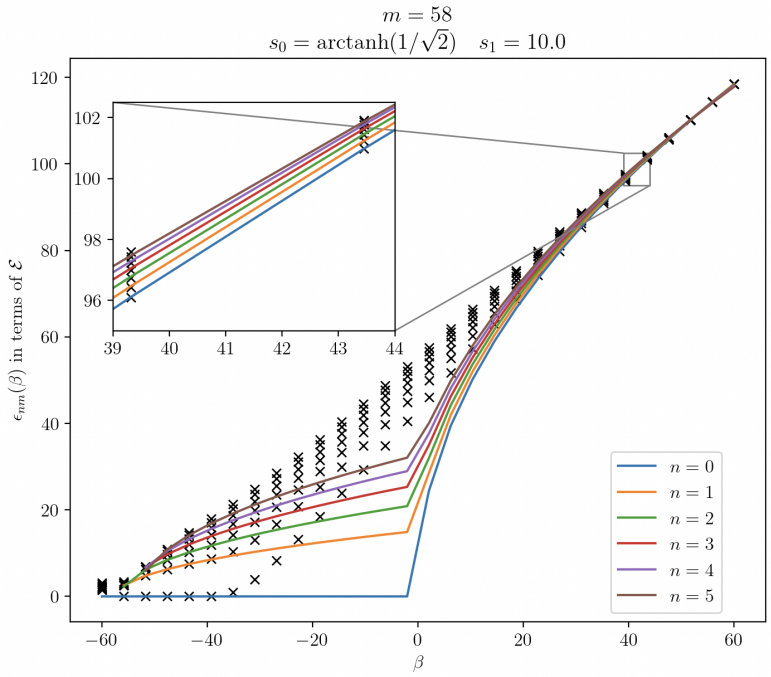

Figure 5.22: Flux dependence of the energy of the reciprocal hyperbolic surface

The continuous lines depict the analytical solutions eq. (5.127) and eq. (5.128) while the crosses represent the numerical results. For the numerics we used $L = 1200$ lattice points in arc length direction.

5.3 Conjecture for General Surfaces $\epsilon_{nm}(B) \propto B^N$ and Nodes

In this sub-chapter, we want to briefly summarize two observations that can be made in the various calculations which we have done so far.

First, we notice that the up and down component $\psi_\downarrow(s)$ and $\psi_\uparrow(s)$ of every arc length wave function $\psi(s)$, calculated numerically in the previous chapters and also analytically for different surfaces of revolution $r(s)$, exhibit a different relative amount of nodes, depending on whether we have the different or the same sign case of B and α_m. Therefore, based on these observations, we formulate the conjecture

Conjecture: For general surfaces of revolution $r(s)$ with arc length bound state solutions $\psi(s)$, the up and down spin components, $\psi_\downarrow(s)$ and $\psi_\uparrow(s)$, have

- the same number of nodes whenever $\operatorname{sgn}(B) = \operatorname{sgn}(\alpha_m)$

- a difference of one in the number of nodes between the components when $\mathrm{sgn}(B) \neq \mathrm{sgn}(\alpha_m)$.

The understanding of this behavior can most likely be drawn from the relation between the up and down component eq. (5.24), where in this equation the main difference in the two cases is that in the case $\mathrm{sgn}(B) \neq \mathrm{sgn}(\alpha_m)$ the effective mass potential $V(s)$ contained in eq. (5.24) has a zero crossing, while in the other case $\mathrm{sgn}(B) = \mathrm{sgn}(\alpha_m)$, it does not. However, the specific link between this observation and the conjecture specified above has to specifically and rigorously be proven mathematically.

We now come to a more interesting observation concerning the asymptotic magnetic field dependence of the bound state energies $\epsilon_{nm}(B)$. So far, we have seen various possibilities of the magnetic field dependence in the bound state energies for various surfaces of revolution $\mathbf{\Sigma}$. The task now is to formulate a conjecture for general surfaces of revolution, therefore, with an arbitrary radial profile $r(s)$. For this purpose, we shall first summarize in Table 1 the results obtained so far.

Surface	**Curvature** K	$r(s)$	$\frac{\mathrm{d}r}{\mathrm{d}s}$	$\epsilon_{nm}(B) \underset{B\to\infty}{\propto}$	$\epsilon_{nm}(B) \underset{B\to\infty}{\propto}$
Pseudosphere	-1	$\exp(-s)$	$-r$	$B^{\frac{1}{4}}$	$B^{\frac{1}{2}}$
Cone	0	$s\sin(\theta/2)$	$r^0 = \mathrm{const}$	$B^{\frac{1}{2}}$	$B^{\frac{1}{2}}$
Reciprocal Cone	$-2\sin^2(\theta/2)r^2 < 0$	$\frac{1}{s\sin(\theta/2)}$	$\propto r^2$	$B^0 = \mathrm{const}$	$B^{\frac{1}{2}}$
Hyperbolic surface	$2 - 2r^2 > 0$	$\tanh(s)$	$1 - r^2$	$B^{\frac{1}{2}}$	$B^{\frac{1}{2}}$
Reciprocal Hyperbolic surface	$2 - 2r^2 < 0$	$\frac{1}{\tanh(s)}$	$1 - r^2$	$B^{\frac{1}{2}}$	$B^{\frac{1}{2}}$

Table 1: A summary of all surfaces analyzed so far with their respective curvature, radius function, radius derivative and the asymptotic behavior of the bound state energies $\epsilon_{nm}(B)$ w.r.t. the magnetic field B for both branches, that is, for the branch where $\mathrm{sgn}(B) \neq \mathrm{sgn}(\alpha_m)$, which is depicted in the first energy column, and for the one where $\mathrm{sgn}(B) = \mathrm{sgn}(\alpha_m)$, which can be seen in the second energy column.

From this table, we notice something very peculiar, namely, for each surface of revolution, we obtain the same asymptotic magnetic field dependence in the energies for the branch $\mathrm{sgn}(\alpha_m) = \mathrm{sgn}(B)$, namely, a square root one. For the other branch, $\mathrm{sgn}(\alpha_m) \neq \mathrm{sgn}(B)$, we obtain various different dependencies, which we now intend to relate to the power N of the radius, which appears in the first derivative of the

radius w.r.t. the arc length $\mathrm{d}r/\mathrm{d}s \propto r^N$. Based on this rationale, we are ready to make a conjecture regarding the proportionality of the magnetic field B in the bound state energies $\epsilon_{nm}(B)$ for general surfaces of revolution, which reads

Conjecture: For general surfaces of revolution $r(s)$, with

$$\frac{\mathrm{d}r}{\mathrm{d}s} \propto r^N \,, \tag{5.129}$$

the bound state energies $\epsilon_{nm}(B)$ exhibit, in the case $\mathrm{sgn}(\alpha_m) \neq \mathrm{sgn}(B)$, at high magnetic fields B, the proportionality

$$\epsilon_{nm}(B) \underset{B\to\infty}{\propto} B^{\frac{2-N}{4}} \,, \tag{5.130}$$

while still at high magnetic fields, but in the case $\mathrm{sgn}(\alpha_m) = \mathrm{sgn}(B)$, we will always have

$$\epsilon_{nm}(B) \underset{B\to\infty}{\propto} B^{\frac{1}{2}} \,. \tag{5.131}$$

Now, this seems rather peculiar. In the first three cases of the table Table 1, this conjecture is obviously true, while in the case of the hyperbolic and reciprocal hyperbolic surface, we have a combination of radii $r' = r^0 - r^2$, and therefore, in principle, we should get the two contributions in the case of $\mathrm{sgn}(\alpha_m) \neq \mathrm{sgn}(B)$, namely, $B^{\frac{1}{2}}$ from r^0 and $B^0 = \mathrm{const}$ for r^2 and therefore, we obviously have in total the asymptotic behavior of $\epsilon_{nm}(B) \underset{B\to\infty}{\propto} B^{\frac{1}{2}}$. We further check this conjecture by numerically calculating other surfaces of revolution. Therefore, we check all remaining surfaces from $N = -2$ to $N = 4$ with N from eq. (5.129). We present the results for the case of different sign in Figure 5.24 and for case of equal sign case in Figure 5.23, where we fit a monomial $\epsilon_{nm}(\beta) = \sqrt{\lambda\beta^\eta}$ to the energies at high fields and thus read the exponent η of the magnetic field in this regime. For states that do not feel the borders of the truncated surface, our conjecture matches the numerics perfectly. Notably, in Figure 5.24 a) or b) we obtain edge states not only for low fields but also for high ones. This is due to the fact that the bound states change their position with changing magnetic flux, shifting more towards the edge of the surface. Here, they approach the smaller end of the surface as the field increases. In Figure 5.24 c) or d) we do not see this behavior because we selected different angular quantum numbers m, placing the states at different positions on the respective surfaces. If one were to increase the flux further in Figure 5.24 c) or d), edge states would also appear, as in a) or b). It is to be noted that for $N > 2$ the energy $\epsilon_{nm}(\beta)$ decreases with increasing magnetic flux β, which again is something unexpected.

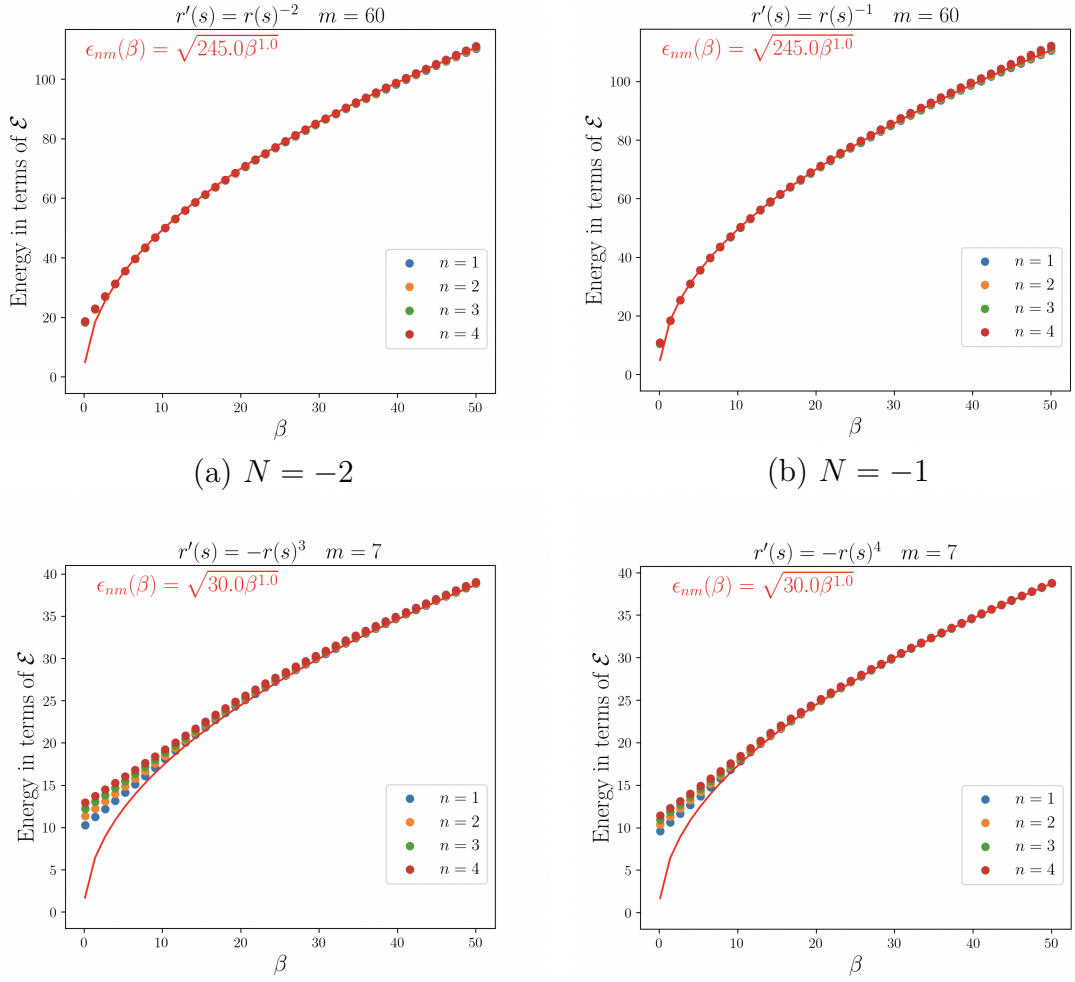

(a) $N = -2$ (b) $N = -1$

(c) $N = 3$ (d) $N = 4$

Figure 5.23: Flux dependence of the energy in the case $\mathrm{sgn}(B) = \mathrm{sgn}(\alpha_m)$

The plots depict the flux dependence of the energy of difference radial profiles fulfilling the differential equation $r' \propto r^N$. This equation is trivially solved, and its spectrum is computed numerically, which is shown by the dots. The continuous lines represent the fitting monomial, which is also shown in the same plot. A square root dependence of the magnetic field is observed for each surface.

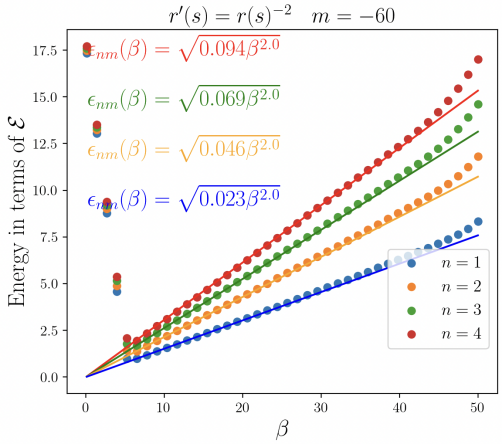

(a) $N = -2$

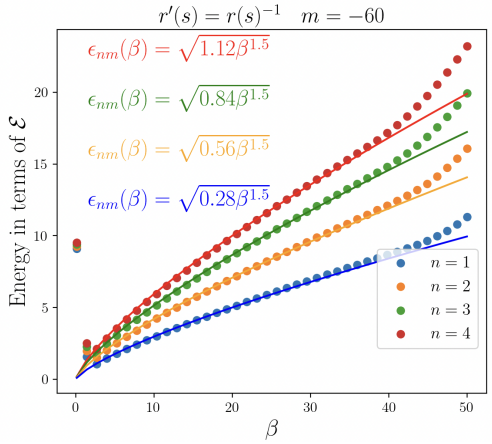

(b) $N = -1$

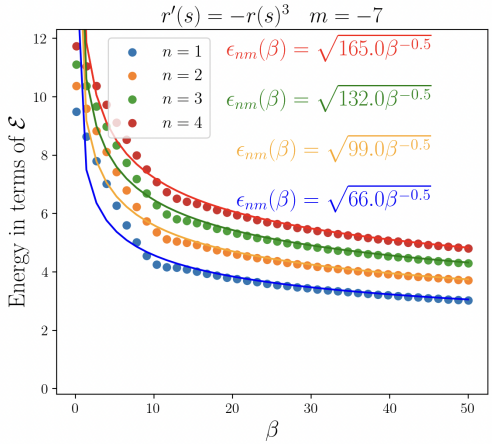

(c) $N = 3$

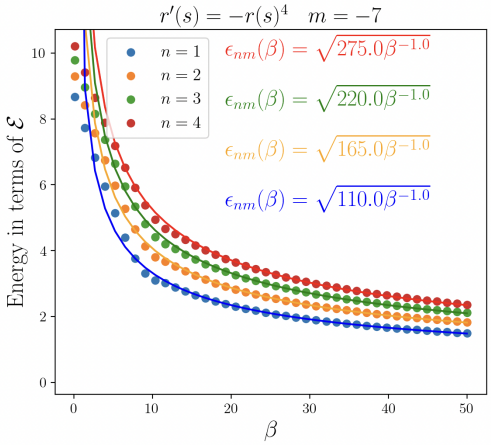

(d) $N = 4$

Figure 5.24: Flux dependence of the energy in the case $\mathrm{sgn}(B) \neq \mathrm{sgn}(\alpha_m)$

The plots depict the flux dependence of the energy of difference radial profiles fulfilling the differential equation $r' \propto r^N$. This equation is trivially solved, and its spectrum is computed numerically, which is shown by the dots. The continuous lines represent the fitting monomial, which is also shown in the same plot.

6 Transport Simulations

Now that we better understand the effects of non-trivial geometry on the Dirac Hamiltonian and the bound states on general surfaces of revolution, we shall fully shift our attention to a much more numerical side of the problem, namely, the quantum magnetotransport across surfaces of revolution and the methods and techniques involved. After a brief introduction to the Landauer-Büttiker formalism, we present the geometric layouts of the setups used for the transport simulations, namely, longitudinal transport across the entire surface from one end to the other and quantum Hall transport simulations.

6.1 Quantum Transport Setup

The Landauer-Büttiker formalism [33] is, among other things, a theoretical framework used to describe quantum transport in mesoscopic systems in the so-called linear response regime, where the applied voltage is smaller then the characteristic energy scales of the conductor. At its core, the Landauer-Büttiker formalism treats electron transport as a wave scattering problem. Electrons incident on a conductor (like a quantum wire or a point contact) are scattered by various imperfections or interfaces within the conductor. The formalism then relates the conductance of the system to these transmission probabilities of electrons through the conductor. Since it is the wave-nature of the electrons that defines the transmission, the formalism relies on the fact that the coherence length[1] of the system l_φ to be much larger than the system itself, which we assume in this work. Moreover, the formalism accounts for multiple transport channels or modes, with each channel contributing to the total conductance depending on its transmission probability. This approach is therefore particularly useful for analyzing systems with complex geometries, which is exactly what we look for. This formalism also turns out to be very useful if the coupling to the leads is big, and the system can be approximated to be non-interacting, which is the case in this work since we are dealing with a single-particle Hamiltonian. In the small temperature limit $T \to 0$, the Landauer-Büttiker formalism yields the conductance

$$G_{ab} = \frac{\partial I_a}{\partial V_b} = \frac{e^2}{h}(T_{ab} - \delta_{ab}) \tag{6.1}$$

in the linear response regime, where a and b are the terminal indices and T_{ab} the transmission probability. Determining these transmission probabilities will be one of the numerical tasks, which we will discus in the next section.

[1] This is the length over which the coherence of the particles is maintained and thus quantum interference effects play a role.

Longitudinal conductance G_{xx} Now that we are familiar with the Landauer-Büttiker formalism, let us go ahead and apply it to one of our already analytically studied systems, the pseudosphere in a coaxial magnetic field. Here, the easiest transport quantity to simulate is the longitudinal conductance, which we denote by G_{xx}. This quantity quantifies the electric current response at low applied voltages between the large and the small end of the pseudosphere. Therefore, in measurements, one requires two wires (terminals) that act as a source and a drain in the system. A way to implement this in our simulations is shown in Figure 6.1. Here, we truncate the pseudosphere (green) at the smaller end and attach semi-infinite cylindrical leads (red) on both sides. The cylindrical leads will not only preserve the rotational symmetry, but, due to their translation invariance, will also host plane waves that will scatter at the lead - pseudosphere interface (red - green). This scattering process is then quantified by the corresponding transmission probability from lead 1 to lead 2, which is T_{12}, and by the above formula, we then obtain the desired longitudinal conductance

$$G_{xx} \equiv G_{12} = \frac{e^2}{h} T_{12} \,. \tag{6.2}$$

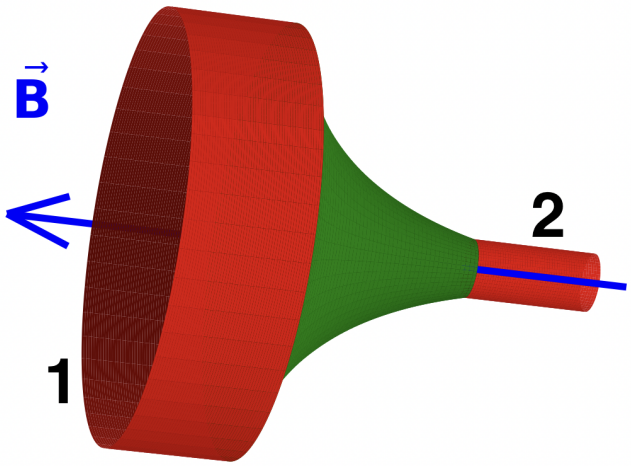

Figure 6.1: Sketch of leads attached to the pseudosphere

The sketch shows the setup used for the longitudinal quantum magneto transport simulations required to calculate the longitudinal conductance G_{xx}. It depicts semi-infinite leads (red) attached to the ends of a truncated pseudosphere (green), subjected to a coaxial magnetic field (blue).

Transversal resistance R_{xy} We not turn to a more involved quantum transport quantity, namely, a quantum Hall resistance, denoted by R_{xy}. This quantity belongs to quantum Hall transport measurements, and describes the ratio between the applied voltage and the measured transversal current. Therefore, for this measurement, one needs at least 4 wires (terminals), and to simulate R_{xy} correctly, we need to define a suitable geometry on the pseudosphere. One way to do so is shown in Figure 6.2, where, again, a cylinder is docked to the large radius side of the pseudosphere (green), but this time, it is divided into 8 equal parts, from which every second is removed, leaving us with 4 leads (red).

The next step is to relate the transversal resistance R_{xy} to the conductance from the Landauer-Büttiker formalism eq. (6.1), which can be found, for example, in Datta's book [34]. The procedure is to set the voltage at one of the terminals to zero, say V_4, which simplifies the current voltage relation to

$$\begin{pmatrix} I_1 \\ I_2 \\ I_3 \end{pmatrix} = \begin{pmatrix} G_{12}+G_{13}+G_{14} & -G_{12} & -G_{13} \\ -G_{21} & G_{21}+G_{23}+G_{24} & -G_{23} \\ -G_{31} & -G_{32} & G_{31}+G_{32}+G_{34} \end{pmatrix} \begin{pmatrix} V_1 \\ V_2 \\ V_3 \end{pmatrix} . \quad (6.3)$$

We denote this conductance matrix simply by $\mathbf{G}$. The transversal resistance R_{xy} is then defined by

$$R_{xy} = \left.\frac{V_3 - V_1}{I_2}\right|_{I_1=I_3=0} = (\mathbf{G}^{-1})_{32} - (\mathbf{G}^{-1})_{12} \, . \quad (6.4)$$

As mentioned before, to construct $\mathbf{G}$, we will have to determine the transmission probabilities T_{ab} by matching incoming and outgoing waves from the leads to the wave function in the scattering region on the pseudosphere. Since this problem is very complex, we have to rely on numerical methods to construct these waves and solve the matching problem. This leads us to the quantum transport Python package *Kwant*.

Transmission Probabilities with *Kwant* To calculate transport characteristics, such as quantum transport in the Landauer-Büttiker regime, we will use the Python package *Kwant* [35]. It is a software package that is used, among other things, to simulate quantum transport in finite systems described by a single-particle Hamiltonian. In addition to a finite scattering region, *Kwant* requires as input semi-infinite periodic leads that are attached to the scattering region to mimic wave-guides. *Kwant* then creates plane waves inside the leads, relying on their periodicity, and matches these incoming and outgoing waves to the scattering region solutions at the border of the region. In doing so, *Kwant* constructs the scattering matrix $\mathbf{S}$, which relates the outgoing flux amplitudes to the incoming ones. $\mathbf{S}$ is then used to construct the transmission coefficients that define the conductance.

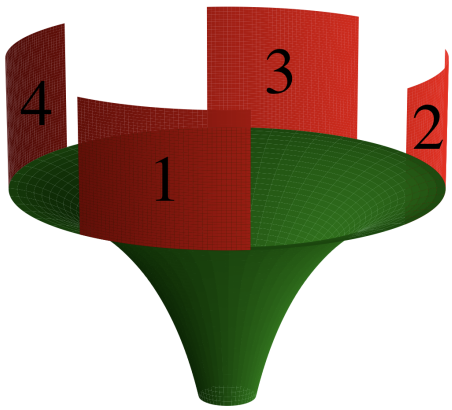

Figure 6.2: Sketch of 4-terminal system attached to the pseudosphere

The pseudosphere is shown as in Figure 5.6, but, this time, we truncate it and attach semi-infinite leads to the larger end to simulate 4-terminal quantum transport. This is realized by docking a cylinder and cutting it into 8 equal pieces, removing every second piece. The leads are numbered from 1 to 4. In the quantum Hall simulations, we use leads 3 and 1 as voltage leads and 2 and 4 as current leads.

Since *Kwant* is a numerical package, it takes as input the discretized version of the full system Hamiltonian from eq. (4.8), and not the continuum one eq. (3.31).

6.2 Disorder

The last building block needed to finally perform the simulations, consists in including disorder into the system to mimic impurities or small defects that occur in real setups. To further emphasize the importance of disorder, let us first go back for a second and recall the role of disorder in a real quantum Hall system, since we are using such a setup to determine the transversal resistance R_{xy} defined above.

In the quantum Hall effect, the quantum Hall plateaus are explained by the robust edge states that flow in only one direction. These edge states come to existence due to the sharp borders of the system, which induce a confining potential that rises sharply at the edges. The filling number ν in eq. (1.1) counts the number of edge states that are present at a given B-field and chemical potential μ. When sweeping the magnetic field B, the number of states at the chemical potential μ changes, and the number of edge states changes suddenly, and hence, the filling number changes suddenly, and so the quantum hall plateaus emerge. Most of the time, μ falls in between two Landau levels in the bulk of the sample. In a model without disorder, this would be very unlikely, since, besides the few edge-states, there are not many states to "pin" the chemical potential at the given energy. Introducing physical

disorder will create a large number of localized states in between the bulk Landau levels. And by that, the lack of localized states to pin the chemical potential at the assumed position is overcome. [36]

In our simulations, the parameter μ does not know anything about the unlikelihood of landing between two Landau levels due to the lack of localized bulk-states - it is merely a mathematical parameter, and hence, we can tune it freely. However, disorder is still important in implementing the physical broadening of the Landau-Levels, which can have physical implications like smearing of quantum Hall plateaus. Therefore, we introduce disorder by an onsite disorder term defined by a random Gaussian correlated scalar potential $V_{\text{dis}}(\mathbf{r})$, where we have

$$\langle V_{\text{dis}}(\mathbf{r}) V_{\text{dis}}(\mathbf{0}) \rangle = \mathcal{K}_0 \frac{\hbar v_F}{2\pi\xi^2} e^{-|\mathbf{r}|^2/2\xi^2} , \tag{6.5}$$

where $\mathcal{K}_0$ is the disorder strength and ξ the disorder length[1], which sets the scale on which the correlation takes place. It is created by an algorithm presented in [37], the so-called Fourier Filtering Method (FFM) method. We then add $V_{\text{dis}}(\mathbf{r})\sigma_0$ to the tight binding Hamiltonian eq. (4.8), where σ_0 is the identity matrix in two dimensions. Note that, for the disorder potential to be smooth on the lattice, we must require $\xi \gg \Delta s, \Delta\varphi$. An example for a disorder landscape on a surface of revolution is shown in Figure 6.3.

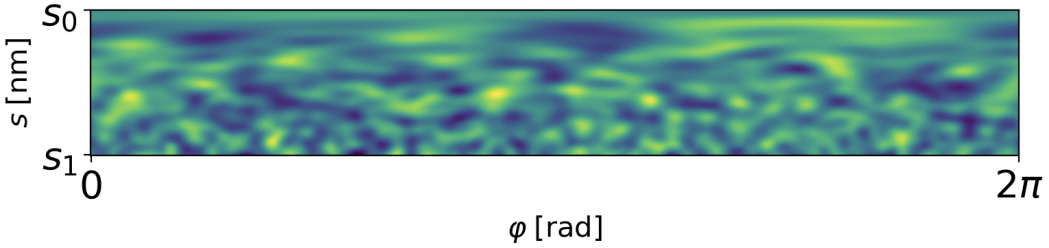

Figure 6.3: Disorder configuration on a surface of revolution

A disorder configuration on the cone (depicted in Figure 5.1) in arbitrary units, where the light color represents a high, and the dark, a low value. When the arc length decreases $s \to s_0$, we approach the apex of the cone, and hence, the length scale on the cone becomes comparable to the disorder length ξ from eq. (6.5), which explains the difference between the two regions around s_0 and s_1.

To numerically calculate a physical observable $\langle \mathcal{O} \rangle$ from the tight-binding Hamiltonian H given in eq. (4.8), which includes a disorder potential, we generate the

[1]Note that, also here, we use rescaled variable, i.e., by ξ we mean $\frac{\xi}{a}$ with the length scale from eq. (3.27).

disorder landscape N_{dis} times, and compute the corresponding quantity $\mathcal{O}_n$ for each instance. The observable $\langle \mathcal{O} \rangle$ is then determined by averaging these computed values,

$$\langle \mathcal{O} \rangle \approx \frac{1}{N_{\text{dis}}} \sum_{i=1}^{N_{\text{dis}}} \mathcal{O}_n \,. \tag{6.6}$$

6.3 Results

Two Terminal Magneto Transport G_{xx} We first simulate the longitudinal conductance and plot it in Figure 6.4. We observe five distinct conductance peaks in the energy range shown, of which the peak around the zero energy point is much more pronounced than the others. Note that the conductance peaks are bound to be smaller than or equal to the conductance quantum $G_0 = 2e^2/h$, where the factor of two stems from the spin degeneracy of the electrons.

We will examine this result by looking at the potential wedges on the pseudosphere for some selected angular quantum numbers m in Figure 6.5. The peculiarity to note here, is that although there are impenetrable potential barriers up to Fermi energies of at least $\sim 25\mathcal{E}$, we still get a non-zero conductance in this range. Moreover, we can see that the position around which the energy levels of each n are centered in Figure 6.5 roughly corresponds to the peak positions in Figure 6.4.

To understand these observations, we first turn our attention to the zeroth peak $n = 0$. It turns out that the appearance of the zero energy peak and its larger magnitude is due to the energy degeneracy of the zero level. At zero energy $n = 0$, the electron can "jump" from potential wedge to potential wedge, from one end $s_0 = 0$ to the other $s_1 = 1$, since the zero energy level exists inside each wedge (see blue dotted line), and thus this is energetically feasible. The role of the disorder, then, is to broaden the peak in the conductance plot Figure 6.4 so that we can observe it, otherwise it would have a $\delta(\epsilon_F)$ peak shape. This reasoning was also used in [23] to explain a similar conductance simulation, but on a cone, where all n levels are degenerate at low energies.

The interesting part lies in the other peaks $n > 0$, since, at higher energies, we see that the energies are non-degenerate, we would have expected the electron transmission to be strongly suppressed. However, it turns out that, even in this case the electron can "jump" from wedge to wedge. This is because the different energy levels in each wedge are broadened due to the disorder potential, and thus, compared to the $n = 0$ case, we get a somewhat smaller but still non-zero energetic overlap between these states, and thus, it is also possible here for the electron to travel from one end to the other of the pseudosphere. It is also clear that the magnitude of the zero energy peak is much higher due to the perfect energetic overlap.

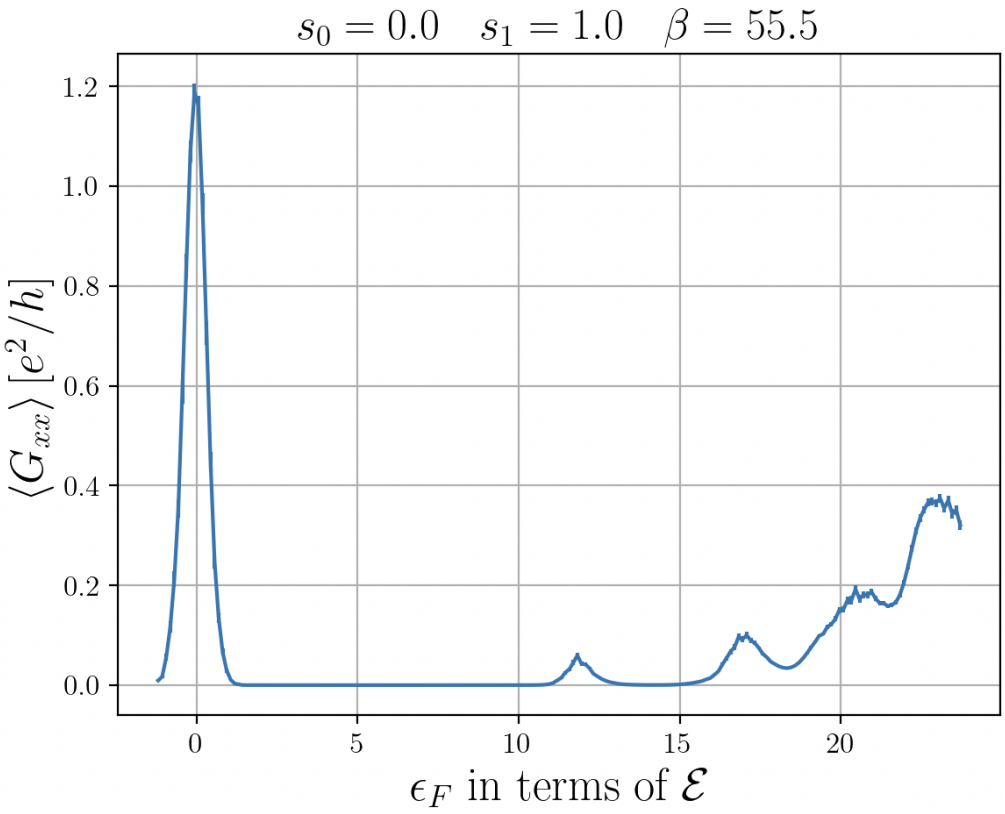

Figure 6.4: Longitudinal conductance on the pseudosphere

The longitudinal conductance $\langle G_{xx} \rangle$ is simulated across the pseudosphere by matching the incoming and outgoing plane wave from the red leads to the wave function in the green scattering region, see Figure 6.1. The corresponding error bars are too small to be visible. The parameters used for the numerical simulations with *Kwant* are $W = 800$, $L = 130$, $\mathcal{K}_0 = 0.05$, $\xi = 0.065$ and $N_{\text{dis}} = 304$.

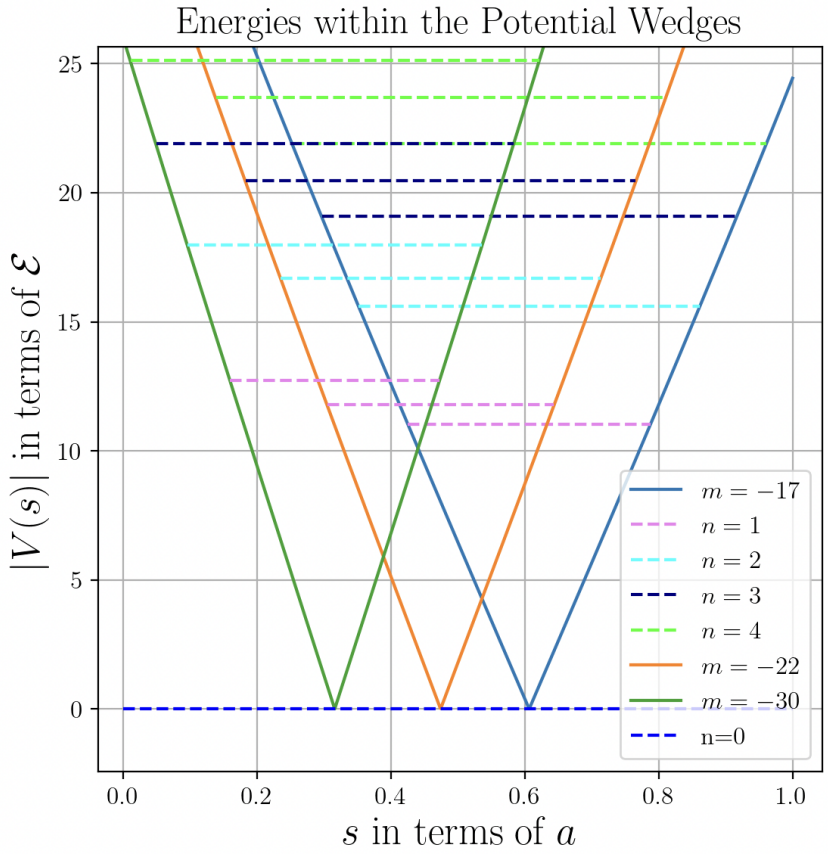

Figure 6.5: Potential wedges on the pseudosphere

Continuous lines depict potential wedges $|V(s)|$ for three different angular quantum numbers m on the pseudosphere. Inside the wedges, the first bounded energy levels on the pseudosphere are computed numerically. Each color of the dotted lines represents a single energy number n.

Four Terminal Magneto Transport R_{xy} We now turn our attention to the simulation of the transversal resistance $\langle R_{xy} \rangle$ from eq. (6.4). In Figure 6.6, this quantity is plotted in some flux interval. Here, one can clearly see the perfect quantum Hall plateaus with their corresponding filling numbers, which are also shown in the same figure.

To make sense of these results, we take a look at the spectrum of the pseudosphere at both ends of the magnetic range used in Figure 6.6. These are shown in Figure 6.7 and Figure 6.8. In these plots, we see that, for higher magnetic numbers m the energies start to deviate from their analytical formula because they start to feel the boundaries of the surface, and thus edge states are formed. Similar to the regular quantum Hall effect, these edge states facilitate the current at the large end

of the pseudosphere to flow in one distinct direction, giving rise to the plateaus in the resistance figure. Moreover, we see that the number of edge states cutting the red dotted Fermi energy line corresponds perfectly to the filling number ν.

Thus, we see that, although the degeneracy of energies is broken in curved systems, which is not the case in regular quantum Hall systems, we still get well-defined edge states, and hence, perfect resistance plateaus.

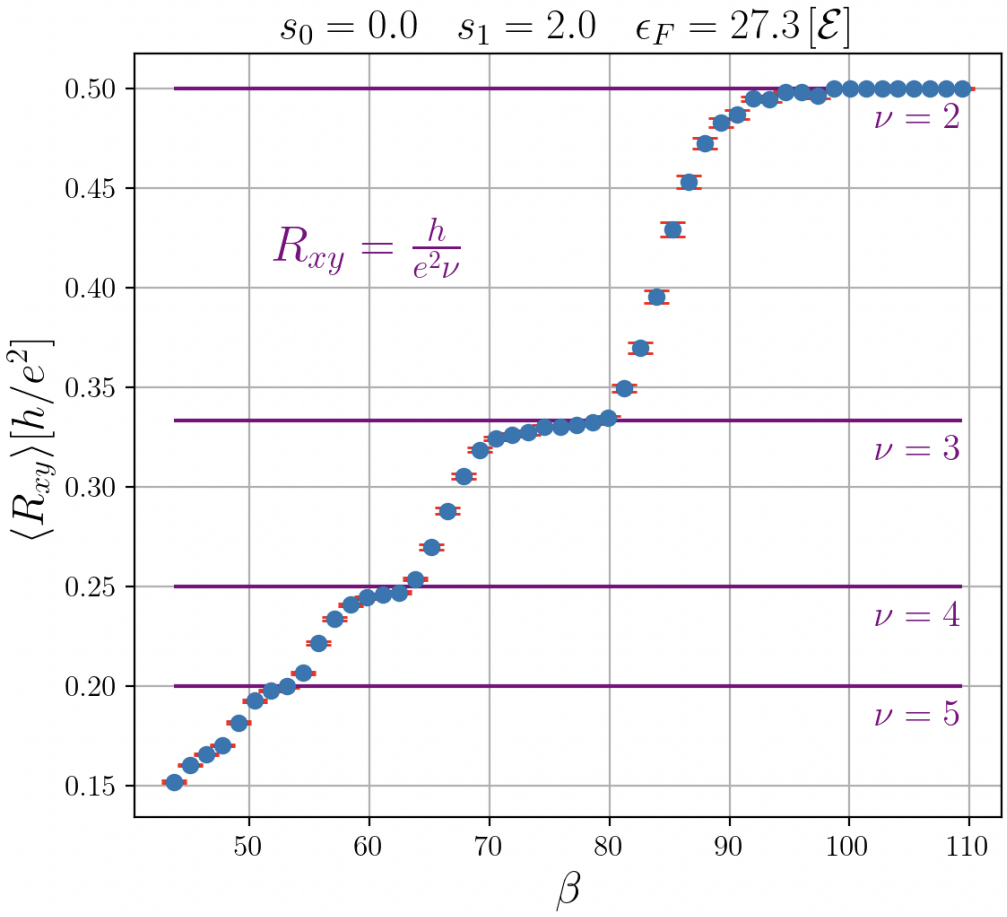

Figure 6.6: Transversal resistance on the pseudosphere

The transversal resistance $\langle R_{xy} \rangle$ (blue dots) is simulated across the pseudosphere by matching the incoming and outgoing plane waves from the red leads to the wave function in the green scattering region, see Figure 6.2. More precisely, the pairwise conductance between two different leads $\langle G_{ij} \rangle$ obtained with *Kwant* is inserted in eq. (6.4) to obtain $\langle R_{xy} \rangle$. The error bars are plotted in red and are barely visible. The purple horizontal lines correspond to the quantum Hall resistance steps. The parameters used for the numerical simulations with *Kwant* are $W = 1280$, $L = 300$, $\mathcal{K}_0 = 0.10$, $\xi = 0.067$ and $N_{\text{dis}} = 191$.

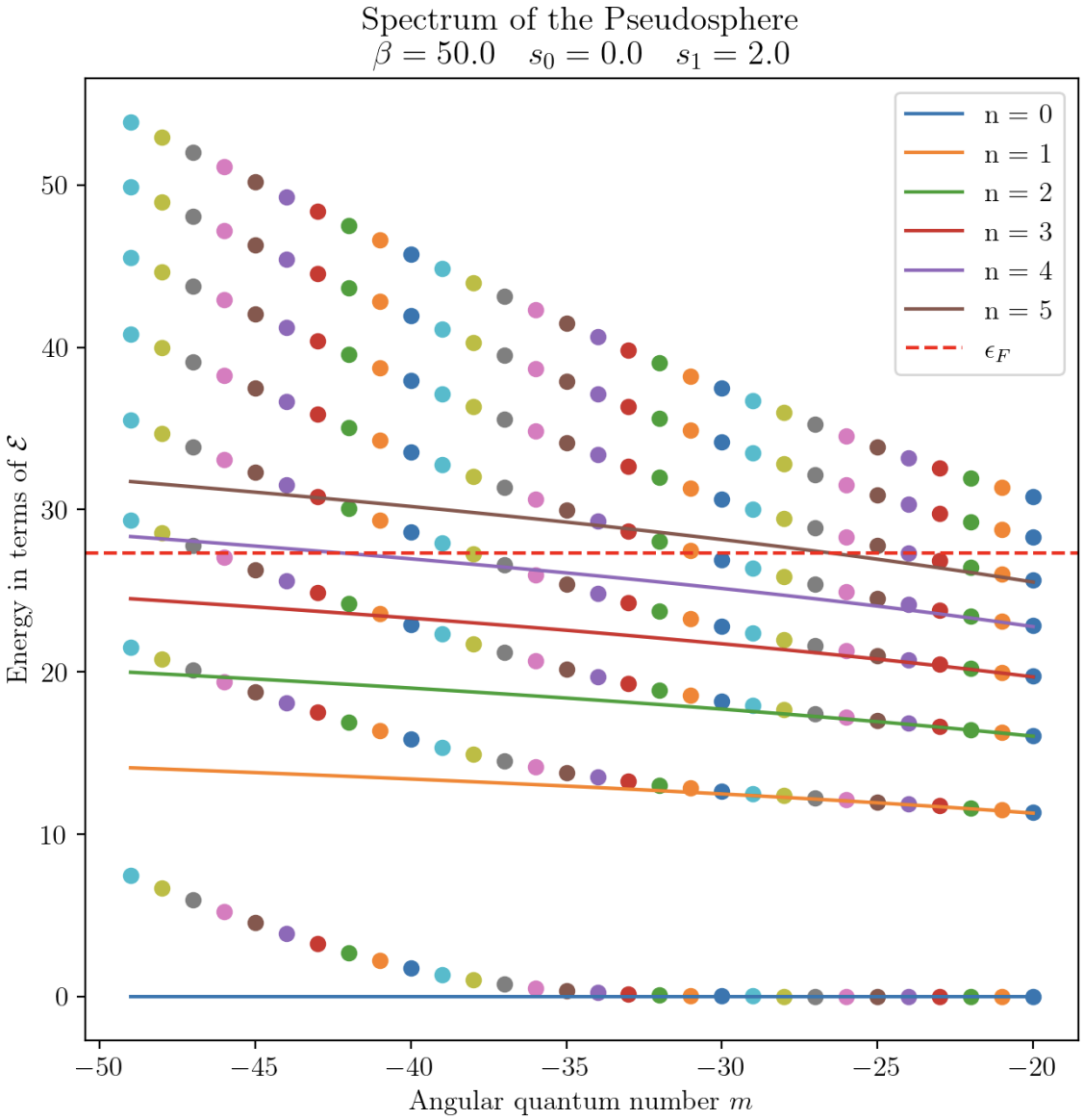

Figure 6.7: Edge states on the pseudosphere for a moderate flux

The energies on the pseudosphere are depicted numerically by the dots and analytically, see eq. (5.74), by the continuous lines. The dotted line describes the Fermi energy used in the transversal transport simulation. The numerical energies deviate from the analytical expression, because the states start to feel the boundaries of the pseudosphere, and thus edge states emerge.

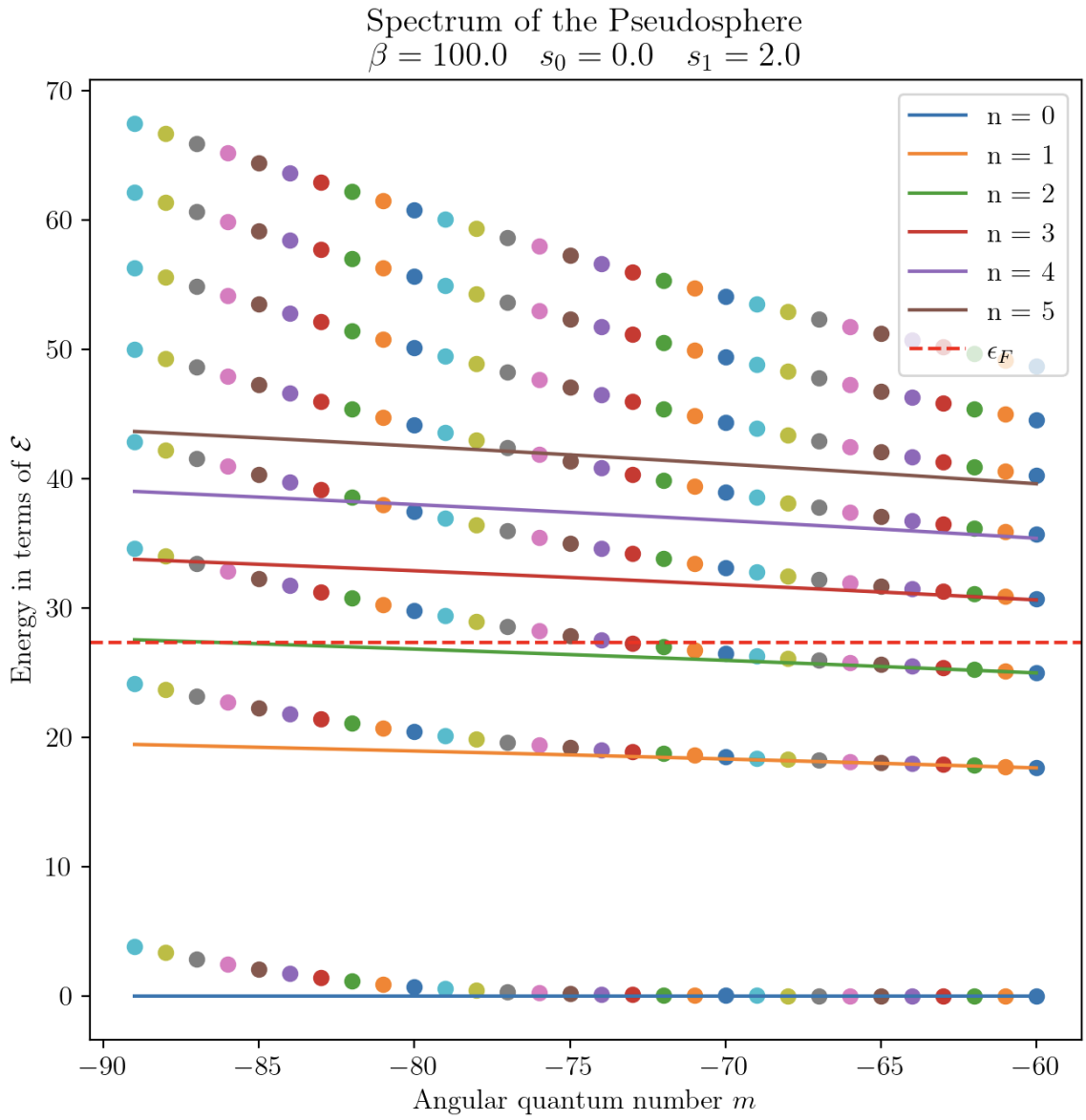

Figure 6.8: Edge states on the pseudosphere for a high flux

The energies on the pseudosphere are depicted numerically by the dots and analytically, see eq. (5.74), by the continuous lines. The dotted line describes the Fermi energy used in the transversal transport simulation. The numerical energies deviate from the analytical expression, because the states start to feel the boundaries of the pseudosphere, and thus edge states emerge.

7 Conclusion and Outlook

In this work, we have studied the transport and spectral properties of electrons on surfaces of curved 3D topological insulators, in order to understand the deeper connection between the physics of conventional topological insulators and curvature. To this end, we have introduced a general theoretical framework that models such materials as rotationally symmetric surfaces of revolution, which involves generalizing the Dirac equation to such surfaces.

For the analytical part, we have solved three different surfaces of revolution with different Gaussian curvatures, the pseudosphere, the cone, and the hyperbolic surface. To the best of our knowledge, this has never been done before for the latter two surfaces. In each case, surprising insights were obtained, especially regarding the relationship between the energetic structure and the curvature. It is worth noting that, in every example calculated, the energies fall into two categories: those that scale with the square root of the magnetic field, and those whose magnetic field scaling strongly depends on the curvature. In the case of the pseudosphere, for example, the scaling was found to be the fourth root. This particular example led to a joint publication [22].

Another insight from this work is the newly introduced concept of reciprocal surfaces, which links the spectrum and wave function of a surface to its reciprocal counterpart. This led us to the reciprocal cone surface, which turns out to possess a spectrum independent of the magnetic field. This is not only new, but also quite remarkable, as it can have massive implications for other physical quantities, such as magnetization, which, in this case, would turn out to be zero. This most likely affects the spin current densities of the electron, which might cancel each other out so that the net magnetic moment is zero.

Another valuable takeaway from this work was the general conjecture regarding the magnetic field scaling of the energies of general surfaces with $r' \propto r^N$. Here, we proved numerically that this conjecture holds. This has even larger implications, since it now appears that there are surfaces whose energies decrease as the magnetic field increases. To the best of our knowledge, there are no known topological insulating systems with such behavior.

The final insight concerned the transport properties on curved surfaces. Here, we revealed the mechanism by which electrons move on a curved topological insulating surface when a small voltage is applied between both ends. In this regime, we obtained distinct conductance peaks, which can be understood by consulting the corresponding energy spectrum. The mechanism by which the electron propagates along the curved surface consists of resonant tunneling through the non-degenerate energy levels, which have a non-zero overlap due to disorder effects in the materials, such as impurities.

A continuation of this thesis could involve rigorously proving the presented con-

jecture for general surface $r' \propto r^N$ by mathematically means. Moreover, it would be necessary to explicitly check the effects of the magnetic field-independent spectrum of the reciprocal cone, such as on the previously mentioned magnetization. For this purpose, one would have to compute the spin current densities, which is now possible analytically due to the derived expressions of the wave functions, and verify whether they indeed cancel out.

A Metric and Spin-Connection

In this section, we derive the space-time metric and the spin-connection of a surface of revolution defined by the parametrization eq. (3.8). From this, we can specify the full space-time parametrization

$$\begin{aligned} \tilde{\mathbf{\Sigma}} &: \mathbb{R}_+ \times (s_0, s_1) \times (0, 2\pi] \to \mathbb{R}^4 \\ \tilde{\mathbf{\Sigma}} &: (t, s, \varphi) \to \begin{pmatrix} t v_F \\ r(s)\cos(\varphi) \\ r(s)\sin(\varphi) \\ z(s) \end{pmatrix} . \end{aligned} \tag{A.1}$$

To find out the metric arising from this parametrization, we need to calculate the tangent vectors

$$\partial_t = \begin{pmatrix} v_F \\ 0 \\ 0 \\ 0 \end{pmatrix} \quad \partial_\varphi = \begin{pmatrix} 0 \\ -r(s)\sin(\varphi) \\ r(s)\cos(\varphi) \\ 0 \end{pmatrix} \quad \partial_s = \begin{pmatrix} 0 \\ r'(s)\cos(\varphi) \\ r'(s)\sin(\varphi) \\ z'(s) \end{pmatrix} , \tag{A.2}$$

where we identify, as usual in differential geometry, e.g., $\partial_t \equiv \partial\tilde{\mathbf{\Sigma}}/\partial t$ and the other vectors in the same way. Then, for the metric, it is straightforward to calculate

$$g_{\mu\nu} = \partial_\mu \cdot \partial^\nu = \eta^{\alpha\nu}\partial_\mu \cdot \partial_\alpha = \mathrm{diag}(-v_F^2, r(s)^2, 1) , \tag{A.3}$$

where $\eta_{\alpha\beta}$ was the flat metric with the signature $(-,+,+)$. In the calculations, we use the following identity

$$\left(\frac{\mathrm{d}r}{\mathrm{d}s}\right)^2 + \left(\frac{\mathrm{d}z}{\mathrm{d}s}\right)^2 = 1 . \tag{A.4}$$

This is easily derived by taking into consideration the definition of the arc length coordinate s, namely

$$\mathrm{d}s^2 = \mathrm{d}x^2 + \mathrm{d}y^2 + \mathrm{d}z^2 \tag{A.5}$$

and, if we switch to polar coordinates in the $x - y$ plane, we get

$$\mathrm{d}s^2 = \mathrm{d}r^2 + r^2\mathrm{d}\varphi^2 + \mathrm{d}z^2 \tag{A.6}$$

and we define the arc length to go around the surface without changing φ, so we get

$$\mathrm{d}s^2 = \mathrm{d}r^2 + \mathrm{d}z^2 \tag{A.7}$$

which yields the claim.

We now seek to calculate the Christoffel symbols $\Gamma^{\rho}_{\alpha\nu}$, which can be done in an elegant way by deriving the Euler-Lagrange equations and comparing them with the geodesic equations on the manifold $\mathbf{\Sigma}$. The Lagrangian is obtained by the relation

$$\mathcal{L} = \frac{1}{2}\dot{x}^{\mu}\dot{x}^{\nu}g_{\mu\nu}\,. \tag{A.8}$$

For instance, the first Euler-Lagrange-Equation with respect to the angle φ reads

$$\frac{\mathrm{d}}{\mathrm{d}t}\frac{\partial\mathcal{L}}{\partial\dot{\varphi}} = \frac{\mathrm{d}}{\mathrm{d}t}(r(s)^2\dot{\varphi}) = 2r(s)\dot{r}(s)\dot{\varphi} + r(s)^2\ddot{\varphi} = 2r(s)\frac{\mathrm{d}r}{\mathrm{d}s}\dot{s}\dot{\varphi} + r(s)^2\ddot{\varphi} = \frac{\partial\mathcal{L}}{\partial\varphi} = 0\,, \tag{A.9}$$

which we can compare with the corresponding geodesic equation

$$\Gamma^{\varphi}_{s\varphi}\dot{s}\dot{\varphi} + \Gamma^{\varphi}_{\varphi s}\dot{\varphi}\dot{s} + \ddot{\varphi} = 0\,, \tag{A.10}$$

from which we can deduce

$$\Gamma^{\varphi}_{s\varphi} = \Gamma^{\varphi}_{\varphi s} = \frac{1}{r(s)}\frac{\mathrm{d}r}{\mathrm{d}s}\,. \tag{A.11}$$

For the other coordinate, we obtain

$$\frac{\mathrm{d}}{\mathrm{d}t}\frac{\partial\mathcal{L}}{\partial\dot{s}} = \ddot{s}\,, \tag{A.12}$$

while for the other side we get

$$\frac{\partial\mathcal{L}}{\partial s} = r(s)\dot{r}\dot{\varphi}^2\,. \tag{A.13}$$

Putting everything together yields

$$\frac{d}{dt}\frac{\partial\mathcal{L}}{\partial\dot{s}} - \frac{\partial\mathcal{L}}{\partial s} = \ddot{s} - r(s)\dot{r}\dot{\varphi}^2 = 0\,. \tag{A.14}$$

This give us the symbol

$$\Gamma^{s}_{\varphi\varphi} = -r(s)\frac{\mathrm{d}r}{\mathrm{d}s}\,. \tag{A.15}$$

Concerning the spin-connection term, one can calculate the only non-zero spin-connection term to be

$$\hat{\omega}^{\varphi s}_{\varphi} = e^{\varphi}_{\varphi}\Gamma^{\varphi}_{s\varphi}e^{ss} = r(s)\frac{1}{r(s)}\frac{\mathrm{d}r}{\mathrm{d}s} = \frac{\mathrm{d}r}{\mathrm{d}s} = -\hat{\omega}^{s\varphi}_{\varphi}\,. \tag{A.16}$$

B Gaussian Curvature

In this chapter, we calculate the distinct Gaussian curvatures of surfaces of revolution. For a more detailed and nuanced description, see [30]. On general two dimensional surfaces embedded in $\mathbb{R}^3$, the Gaussian curvature K is given by

$$K = \frac{\det(\mathrm{II})}{\det(\mathrm{I})}\,, \tag{B.1}$$

where I and II are the first and second fundamental form, respectively. In local coordinates, using the parametrization from eq. (3.8), they read

$$\mathrm{I}_{ij} = \left\langle \frac{\partial \boldsymbol{\Sigma}}{\partial x_i}, \frac{\partial \boldsymbol{\Sigma}}{\partial x_j} \right\rangle \text{ and } \mathrm{II}_{ij} = \left\langle \frac{\partial^2 \boldsymbol{\Sigma}}{\partial x_i \partial x_j}, \hat{n} \right\rangle, \tag{B.2}$$

where $x_1 = s$ and $x_2 = \varphi$. Moreover, $\hat{n}$ denotes the normal vector of the surface, and $\langle \cdot, \cdot \rangle$ the usual scalar product in $\mathbb{R}^n$. The calculation of the first fundamental form is straight forward, since the tangential vectors are orthogonal (see Appendix A), hence

$$\mathrm{I}_{11} = 1 \text{ and } \mathrm{I}_{22} = r(s)^2\,, \tag{B.3}$$

while the off-diagonal elements vanish. Therefore, we obtain

$$\det(\mathrm{I}) = r(s)^2\,. \tag{B.4}$$

The normal vector is easily calculated

$$\hat{n} = \left(\frac{\partial \boldsymbol{\Sigma}}{\partial x_1} \times \frac{\partial \boldsymbol{\Sigma}}{\partial x_2} \right) \Bigg/ \left| \frac{\partial \boldsymbol{\Sigma}}{\partial x_1} \times \frac{\partial \boldsymbol{\Sigma}}{\partial x_2} \right|, \tag{B.5}$$

which gives us

$$\hat{n} = \begin{pmatrix} z'(s)\cos(\varphi) \\ z'(s)\sin(\varphi) \\ -r'(s) \end{pmatrix}\,. \tag{B.6}$$

With this, we obtain

$$\mathrm{II}_{11} = r''(s)z'(s) - r'(s)z''(s) \tag{B.7}$$

$$\mathrm{II}_{22} = -z'(s)r(s) \tag{B.8}$$

$$\mathrm{II}_{12} = \mathrm{II}_{21} = 0 \tag{B.9}$$

and therefore,

$$\det(\mathrm{II}) = \mathrm{II}_{11}\mathrm{II}_{22} = -r''(s)r(s)\,, \tag{B.10}$$

where we have used

$$r''(s)r'(s) + z''(s)z'(s) = 0\,, \tag{B.11}$$

which follows from

$$z'(s)^2 + r'(s)^2 = 1\,, \tag{B.12}$$

which was showed in Appendix A. Therefore, altogether we obtain

$$K = -\frac{r''(s)}{r(s)}\,. \tag{B.13}$$

C Dirac Hamiltonian

To derive the Dirac Hamiltonian, we start from eq. (3.5) and use the expressions of the covariant derivative D_μ from eq. (3.21),

$$i\gamma^a e_a^\mu D_\mu = \sigma_z \frac{1}{v_F}\partial_t + i\sigma_x \frac{1}{r(s)} D_\varphi + i\sigma_y \partial_s = 0\,. \tag{C.1}$$

Multiplying σ_z on both sides, we obtain

$$\frac{1}{v_F}\partial_t + i\sigma_z\sigma_x \frac{1}{r(s)} D_\varphi + i\sigma_z\sigma_y \partial_s = \frac{1}{v_F}\partial_t - \sigma_y \frac{1}{r(s)} D_\varphi + \sigma_x \partial_s = 0\,. \tag{C.2}$$

We assume stationary states

$$\Psi(t, s, \varphi) = \psi(s, \varphi) e^{i\epsilon t/\hbar} \tag{C.3}$$

and insert them into the Dirac equation

$$i\gamma^a e_a^\mu D_\mu \Psi(t, s, \varphi) = 0\,, \tag{C.4}$$

which yields

$$\left[\frac{1}{v_F}\left(-i\frac{\epsilon}{\hbar}\right) - \sigma_y \frac{1}{r(s)} D_\varphi + \sigma_x \partial_s\right]\psi(s, \varphi) = 0 \tag{C.5}$$

and, therefore,

$$\hbar v_F \left[i\sigma_y \frac{1}{r(s)} D_\varphi - i\sigma_x \partial_s\right]\psi(s, \varphi) = \epsilon\psi(s, \varphi)\,. \tag{C.6}$$

By expanding D_φ and evaluating $i\sigma_y i\sigma_z = -i\sigma_x$, we obtain

$$\hbar v_F \left[i\sigma_y \frac{1}{r(s)}\left(\partial_\varphi + i\frac{e}{\hbar} A_\varphi r(s)\right) - i\sigma_x\left(\partial_s + \frac{\hat{\omega}_\varphi^{\varphi s}}{2r(s)}\right)\right]\psi(s, \varphi) = \epsilon\psi(s, \varphi)\,. \tag{C.7}$$

D Analytical Solution for $K = 0$

We first want to derive the equation eq. (5.36). We therefore start from eq. (5.23). To compute it, we calculate

$$V^2(s) = \frac{\alpha_m^{\theta\,2}}{s^2} + s^2\beta_\theta^2 + 2\alpha_m^\theta\beta_\theta\,, \tag{D.1}$$

while for the derivative we get

$$\partial_s V(s) = -\frac{\alpha_m^\theta}{s^2} + \beta_\theta\,. \tag{D.2}$$

For the down part, we therefore get the equation

$$\left(-\partial_s^2 - \frac{\alpha_m^\theta}{s^2} + \beta_\theta + \frac{\alpha_m^{\theta\,2}}{s^2} + s^2\beta_\theta^2 + 2\alpha_m^\theta\beta_\theta\right)\psi_\downarrow = \epsilon^2\psi_\downarrow \tag{D.3}$$

and by grouping everything by powers, we get

$$\left(-\partial_s^2 + A_1 - \epsilon^2 + \frac{A_2}{s^2} + A_3 s^2\right)\psi_\downarrow = 0\,, \tag{D.4}$$

where the variables are

$$A_1 = \beta_\theta + 2\beta_\theta\alpha_m^\theta \tag{D.5}$$
$$A_2 = \alpha_m^{\theta\,2} - \alpha_m^\theta \tag{D.6}$$
$$A_3 = \beta_\theta^2\,. \tag{D.7}$$

To solve this, we make the Ansatz

$$\psi_\downarrow = \frac{p\left(\sqrt{A_3}s^2\right)}{\sqrt{s}}\,, \tag{D.8}$$

and denote $\tilde{s} = \sqrt{A_3}s^2$. After plugging in, the remaining equation reads

$$\left(\tilde{s}^2 + \frac{A_1 - \epsilon^2}{A_3}\,\tilde{s} + A_2 - \frac{3}{4}\right)p(\tilde{s}) - 4p''(\tilde{s})\,\tilde{s}^2 = 0\,. \tag{D.9}$$

By dividing $-4\tilde{s}^2$ out, one obtains

$$\left(-\frac{1}{4} - \frac{A_1 - \epsilon^2}{4A_3}\frac{1}{\tilde{s}} - \frac{A_2 - \frac{3}{4}}{4\tilde{s}^2}\right)p(\tilde{s}) + p''(\tilde{s}) = 0\,. \tag{D.10}$$

This is precisely Whitaker's differential equation, with solutions as specified in the main text.

In this part, we will give the analysis of the excited states. We consider all four cases independently, i.e., the two cases with the same sign and the two other cases with different signs between flux and angular quantum number. In the following analysis, we use some identities for the generalized Laguerre polynomials, which are

$$\partial_x L_n^\alpha(x) = -L_{n-1}^{\alpha+1}(x) \tag{D.11}$$
$$nL_n^\alpha(x) = (n+\alpha)L_{n-1}^\alpha(x) - xL_{n-1}^{\alpha+1}(x) \tag{D.12}$$
$$xL_n^{\alpha+1}(x) = (n+\alpha)L_{n-1}^\alpha(x) - (n-x)L_n^\alpha(x) \tag{D.13}$$
$$L_n^\alpha(x) = L_n^{\alpha+1}(x) - L_{n-1}^{\alpha+1}(x)\,. \tag{D.14}$$

Moving on, we apply the operator eq. (5.53) to get the up component. In each case, we start with the equation of the wave function, which we get from eq. (5.40) and reads

$$\psi_\downarrow(s) \propto \exp(-|\beta_\theta|s^2/2)s^{|\alpha_m^\theta - 1/2|+1/2}L_n^{|\alpha_m^\theta-1/2|}(|\beta_\theta|s^2)\,. \tag{D.15}$$

Let us start with
$B > 0$ and $\alpha_m^\theta > 1/2$:

$$\psi_\downarrow(s) \propto \exp(-\beta_\theta s^2/2)s^{\alpha_m^\theta}L_n^{\alpha_m^\theta-1/2}(\beta_\theta s^2)\,, \tag{D.16}$$

and for the up-component, by eq. (5.24), we obtain

$$\psi_\uparrow(s) \propto \frac{2i\beta_\theta}{\epsilon_{nm}}\exp(-\beta_\theta s^2/2)s^{\alpha_m^\theta+1}L_n^{\alpha_m^\theta+1/2}(\beta_\theta s^2)\,. \tag{D.17}$$

$B < 0$ and $\alpha_m^\theta < 1/2$:

$$\psi_\downarrow(s) \propto \exp(\beta_\theta s^2/2)s^{-\alpha_m^\theta+1}L_n^{-\alpha_m^\theta+1/2}(-\beta_\theta s^2)\,, \tag{D.18}$$

and by this, we obtain for the up-component

$$\psi_\uparrow(s) \propto \frac{-2i(n-\alpha_m^\theta+1/2)}{\epsilon_{nm}}\exp(\beta_\theta s^2/2)s^{-\alpha_m^\theta}L_n^{-\alpha_m^\theta-1/2}(-\beta_\theta s^2)\,. \tag{D.19}$$

By using the expression for the energy

$$\epsilon_{nm} = \pm\sqrt{4|\beta_\theta|\Big(\frac{1}{2}+n+|\alpha_m^\theta|\Big)}\,, \tag{D.20}$$

we obtain

$$\psi_\uparrow(s) \propto \frac{-i\epsilon_{nm}}{-2\beta_\theta}\exp(\beta_\theta s^2/2)s^{-\alpha_m^\theta}L_n^{-\alpha_m^\theta-1/2}(-\beta_\theta s^2)\,. \tag{D.21}$$

Thus, all together, if we sum up, we have for the case of $B, \alpha_m^\theta > 0$ the full spinor

$$\psi(s) \propto s^{|\alpha_m^\theta|} \exp(-|\beta_\theta| s^2/2) \begin{pmatrix} \frac{2i|\beta_\theta|}{\epsilon_{nm}} s L_n^{|\alpha_m^\theta|+1/2}(|\beta_\theta| s^2) \\ L_n^{|\alpha_m^\theta|-1/2}(|\beta_\theta| s^2) \end{pmatrix} , \tag{D.22}$$

while for the other case of $B, \alpha_m^\theta < 0$, it reads

$$\psi(s) \propto s^{|\alpha_m^\theta|} \exp(-|\beta_\theta| s^2/2) \begin{pmatrix} \frac{\epsilon_{nm}}{2i|\beta_\theta|} L_n^{|\alpha_m^\theta|-1/2}(|\beta_\theta| s^2)) \\ s L_n^{|\alpha_m^\theta|+1/2}(|\beta_\theta| s^2) \end{pmatrix} . \tag{D.23}$$

We could have gotten the same result by simply looking at the time reversal transformation $\mathcal{T}$, which changes $B \to -B$ and $m \to -m$. In spinor space, the time reversal transformation reads

$$\mathcal{T} = i\sigma_y \mathcal{K} , \tag{D.24}$$

where $\mathcal{K}$ is the complex conjugate operator. With this, we take the solution for $B, \alpha_m^\theta < 0$ and apply $\mathcal{T}$ on it, which yields

$$\begin{aligned} \mathcal{T}\psi(s) \propto \begin{pmatrix} -i\psi_\downarrow^* \\ i\psi_\uparrow^* \end{pmatrix} &= s^{|\alpha_m^\theta|} \exp(-|\beta_\theta| s^2/2) \begin{pmatrix} -is L_n^{|\alpha_m^\theta|+1/2}(|\beta_\theta| s^2) \\ \frac{-\epsilon_{nm}}{2|\beta_\theta|} L_n^{|\alpha_m^\theta|-1/2}(|\beta_\theta| s^2)) \end{pmatrix} \\ &\propto s^{|\alpha_m^\theta|} \exp(-|\beta_\theta| s^2/2) \begin{pmatrix} -i(\frac{-\epsilon_{nm}}{2|\beta_\theta|})^{-1} s L_n^{|\alpha_m^\theta|+1/2}(|\beta_\theta| s^2) \\ L_n^{|\alpha_m^\theta|-1/2}(|\beta_\theta| s^2)) \end{pmatrix} \\ &= \begin{pmatrix} \frac{2i|\beta_\theta|}{\epsilon_{nm}} s L_n^{|\alpha_m^\theta|+1/2}(|\beta_\theta| s^2) \\ L_n^{|\alpha_m^\theta|-1/2}(|\beta_\theta| s^2)) \end{pmatrix} . \end{aligned} \tag{D.25}$$

References

[1] K. v. Klitzing, G. Dorda, and M. Pepper. "New Method for High-Accuracy Determination of the Fine-Structure Constant Based on Quantized Hall Resistance". In: *Phys. Rev. Lett.* 45 (6 1980), pp. 494–497.

[2] Tomoki Ozawa et al. "Topological photonics". In: *Rev. Mod. Phys.* 91 (1 2019), p. 015006.

[3] B. Andrei Bernevig, Taylor L. Hughes, and Shou-Cheng Zhang. "Quantum Spin Hall Effect and Topological Phase Transition in HgTe Quantum Wells". In: *Science* 314.5806 (2006), pp. 1757–1761.

[4] Y. Zhang, YW. Tan, H. Stormer, et al. "Experimental observation of the quantum Hall effect and Berry's phase in graphene". In: *Nature* 438 (2005), pp. 201–204.

[5] M. Nakahara. *Geometry, Topology and Physics*. Graduate Student Series in Physics. Bristol, UK: Hilger, 1990.

[6] Michael Victor Berry. "Quantal phase factors accompanying adiabatic changes". In: *Proc. R. Soc. Lond. A* 392 (1984), pp. 45–57.

[7] D. J. Thouless et al. "Quantized Hall Conductance in a Two-Dimensional Periodic Potential". In: *Phys. Rev. Lett.* 49 (6 1982), pp. 405–408.

[8] Liang Fu. "Topological Crystalline Insulators". In: *Phys. Rev. Lett.* 106 (10 2011), p. 106802.

[9] K. S. Lin et al. "Spin-resolved topology and partial axion angles in three-dimensional insulators". In: *Nat Commun* 15 (2024), p. 550.

[10] Markus König et al. "Quantum Spin Hall Insulator State in HgTe Quantum Wells". In: *Science* 318.5851 (2007), pp. 766–770.

[11] Y. L. Chen et al. "Experimental Realization of a Three-Dimensional Topological Insulator, Bi2Te3". In: *Science* 325.5937 (2009), pp. 178–181.

[12] D. Hsieh et al. "A tunable topological insulator in the spin helical Dirac transport regime". In: *Nature* 460 (2009), pp. 1101–1105.

[13] M. Kessel et al. "CdTe-HgTe core-shell nanowire growth controlled by RHEED". In: *Phys. Rev. Mater.* 1 (2 2017), p. 023401.

[14] J. Ziegler et al. "Probing spin helical surface states in topological HgTe nanowires". In: *Phys. Rev. B* 97 (3 2018), p. 035157.

[15] C.L. Kane. *Chapter 1 - Topological Band Theory and the Z2 Invariant*. Ed. by Marcel Franz and Laurens Molenkamp. Vol. 6. Contemporary Concepts of Condensed Matter Science. Elsevier, 2013, pp. 3–34.

[16] F. D. M. Haldane. "Model for a Quantum Hall Effect without Landau Levels: Condensed-Matter Realization of the "Parity Anomaly"". In: *Phys. Rev. Lett.* 61 (18 1988), pp. 2015–2018.

[17] R. Jackiw and C. Rebbi. "Solitons with fermion number $\frac{1}{2}$". In: *Phys. Rev. D* 13 (12 1976), pp. 3398–3409.

[18] C. L. Kane and E. J. Mele. "Z_2 Topological Order and the Quantum Spin Hall Effect". In: *Phys. Rev. Lett.* 95 (14 2005), p. 146802.

[19] Jianpeng Liu and David Vanderbilt. "Spin-orbit spillage as a measure of band inversion in insulators". In: *Phys. Rev. B* 90 (12 2014), p. 125133.

[20] Liang Fu, C. L. Kane, and E. J. Mele. "Topological Insulators in Three Dimensions". In: *Phys. Rev. Lett.* 98 (10 2007), p. 106803.

[21] Marián Fecko. *Differential Geometry and Lie Groups for Physicists*. Cambridge University Press, 2006.

[22] Maximilian Fuerst et al. "Dirac Landau levels for surfaces with constant negative curvature". In: *Phys. Rev. B* 109 (19 2024), p. 195433.

[23] Raphael Kozlovsky. "Magnetotransport in 3D Topological Insulator Nanowires". Herausgegeben vom Präsidium des Alumnivereins der Physikalischen Fakultät: Klaus Richter, Andreas Schäfer, Dieter Weiss. Dissertation. Regensburg: Universität Regensburg, 2020. ISBN: 978-3-86845-161-0.

[24] E. Ma et al. "Unexpected edge conduction in mercury telluride quantum wells under broken time-reversal symmetry". In: *Nat Commun* 6 (2015), p. 7252.

[25] L É Gendenshteĭn and I V Krive. "Supersymmetry in quantum mechanics". In: *Soviet Physics Uspekhi* 28.8 (1985), p. 645.

[26] J. M. Luttinger. "The Effect of a Magnetic Field on Electrons in a Periodic Potential". In: *Phys. Rev.* 84 (4 1951), pp. 814–817.

[27] K. M. Masum Habib, Redwan N. Sajjad, and Avik W. Ghosh. "Modified Dirac Hamiltonian for efficient quantum mechanical simulations of micron sized devices". In: *Applied Physics Letters* 108.11 (Mar. 2016), p. 113105. ISSN: 0003-6951.

[28] Vidal Alonso, Salvatore De Vincenzo, and Luigi Mondino. "On the boundary conditions for the Dirac equation". In: *European Journal of Physics* 18.5 (1997), p. 315.

[29] A. L. Araújo et al. "Interplay between boundary conditions and Wilson's mass in Dirac-like Hamiltonians". In: *Phys. Rev. B* 100 (20 2019), p. 205111.

[30] Wolfgang Kühnel. *Differential Geometry: Curves - Surfaces - Manifolds*. Trans. by Bruce Hunt. Vol. 77. The Student Mathematical Library. University of Stuttgart, Stuttgart, Germany, 2015. ISBN: 978-1-4704-2320-9 (print); 978-1-4704-2675-0 (online).

[31] Geusa de A Marques et al. "Landau levels in the presence of topological defects". In: *Journal of Physics A: Mathematical and General* 34.30 (July 2001), 5945–5954. ISSN: 1361-6447.

[32] W Lay, K Bay, and S Yu Slavyanov. "Asymptotic and numeric study of eigenvalues of the double confluent Heun equation". In: *Journal of Physics A: Mathematical and General* 31.42 (1998), p. 8521.

[33] M. Büttiker. "Absence of backscattering in the quantum Hall effect in multiprobe conductors". In: *Phys. Rev. B* 38 (14 1988), pp. 9375–9389.

[34] Supriyo Datta. *Electronic Transport in Mesoscopic Systems*. Cambridge Studies in Semiconductor Physics and Microelectronic Engineering. Cambridge University Press, 1995.

[35] Christoph W Groth et al. "Kwant: a software package for quantum transport". In: *New Journal of Physics* 16.6 (2014), p. 063065.

[36] Gabriele Giuliani and Giovanni Vignale. *Quantum Theory of the Electron Liquid*. Cambridge University Press, 2005.

[37] Johannes Zierenberg et al. "Percolation thresholds and fractal dimensions for square and cubic lattices with long-range correlated defects". In: *Phys. Rev. E* 96 (6 2017), p. 062125.

Eigenständigkeitserklärung

Ich habe die Arbeit selbständig verfasst, keine anderen als die angegebenen Quellen und Hilfsmittel benutzt und bisher keiner anderen Prüfungsbehörde vorgelegt. Außerdem bestätige ich hiermit, dass die vorgelegten Durckexemplare und die vorgelegte elektronische Version der Arbeit identisch sind, dass ich über wissenschaftlich korrektes Arbeiten und Zitieren aufgeklärt wurde und dass ich von den in § 24 Abs. 6 vorgesehenen Rechtsfolgen Kenntnis habe.

Ort, Datum: **Unterschrift:**

_____ _____